Cavity optomagnonics

Manipulating magnetism by light

Sharma, Sanchar

DOI
10.4233/uuid:81ce7e8c-2965-42a0-bac6-b8ba6f6faee3

Publication date
2019

Document Version
Final published version

Citation (APA)
Sharma, S. (2019). *Cavity optomagnonics: Manipulating magnetism by light*. [Dissertation (TU Delft), Delft University of Technology]. https://doi.org/10.4233/uuid:81ce7e8c-2965-42a0-bac6-b8ba6f6faee3

Cavity optomagnonics

Manipulating magnetism by light

Cavity optomagnonics

Manipulating magnetism by light

Proefschrift

ter verkrijging van de graad van doctor
aan de Technische Universiteit Delft,
op gezag van de Rector Magnificus Prof. dr. ir. T.H.J.J. van der Hagen,
voorzitter van het College voor Promoties,
in het openbaar te verdedigen op dinsdag 12 september 2019 om 15:00 uur

door

Sanchar SHARMA

Master of Technology in Electrical Engineering,
Indian Institute of Technology, Mumbai, India
geboren te Jaipur, India.

Dit proefschrift is goedgekeurd door de

promotors: Prof.dr.ir. G.E.W. Bauer and Prof.dr. Y.M. Blanter

Samenstelling promotiecommissie:

Rector Magnificus,	voorzitter
Prof.dr.ir. G.E.W. Bauer	Technische Universiteit Delft
Prof.dr. Y.M. Blanter	Technische Universiteit Delft
Onafhankelijke leden:	
Prof.dr. K. Usami	University of Tokyo
Prof.dr. G.A. Steele	Technische Universiteit Delft
Prof.dr. R. Duine	Universiteit Utrecht
Dr. J. A. Haigh	Hitachi Cambridge Laboratory
Dr. A. Caviglia	Technische Universiteit Delft
Prof.dr.ir. H.S.J. van der Zant	Technische Universiteit Delft, reservelid

Casimir PhD Series, Delft-Leiden 2019-30

ISBN 978-90-8593-413-4

Contents

Summary

Magnets are indispensable for compact data storage such as hard disks, and are proposed to improve logic devices due to their robust and low power data processing capabilities. YIG (Yttrium iron garnet) stands out among all magnets for a very high magnetic quality. In a YIG sample under a magnetic field, a large majority of electrons have spins opposite to the magnetic field and it costs energy to flip any of them. A minority are parallel to the magnetic field due to thermal noise, from which energy can be extracted in principle.

Shining laser at a magnet flips the spins therein. An optical method to manipulate spins facilitates information exchange between fast carriers (photons) and a storage element (magnet). However, in typical experiments, the probability of a spin flip in YIG is so low that spins are nearly unaffected. As discussed in this thesis, we can make this probability significant by confining photons inside a YIG sphere such that they interact with each electron multiple times.

In this thesis, I develop a theory of the effect of photons on spins in a YIG sphere and vice versa. I discuss how to optically extract energy from or inject energy into the magnet in a controllable fashion, useful for making thermodynamic engines. While laser is known to heat substances, it can, counter-intuitively, cool a magnet. I discuss how to optimize this cooling effect and argue that it is feasible to experimentally observe it. We envision our theory to help develop technology for arbitrary manipulation of spins using light.

Samenvatting

Magneten zijn onmisbaar voor compacte computergeheugen, zoals harde schijven, en worden voorgesteld om logic devices te verbeteren vanwege hun robuuste en energiebesparende gegevensverwerkingsmogelijkheden. YIG (Yttrium ijzer granaat) is speciaal onder alle magneten voor een zeer hoge magnetische kwaliteit. In een YIG-monster onder een magnetisch veld heeft een grote meerderheid van elektronen spins tegengesteld aan het magnetische veld en het kost energie om ze om te draaien. Een minderheid is parallel aan het magnetisch veld vanwege thermische fluctuaties, waaruit in principe energie kan worden onttrokken.

Schitterende laser op een magneet draait de spins daarin om. Een optische methode om spins te manipuleren helpt in bij de uitwisseling van informatie tussen snelle fotonen en een geheugen (magneet). In typische experimenten is de waarschijnlijkheid van een spin flip in YIG zo laag dat spins bijna niet worden beïnvloed. Zoals in dit proefschrift geschreven, kunnen we deze kans vergroten door fotonen binnen een YIG-bol in te vangen, zodat ze meerdere keren met elk elektron interactie hebben.

In dit proefschrift ontwikkel ik een theorie van het gevolg van fotonen op spins in een YIG-bol en vice versa. Ik schrijf hoe je energie kunt uittrekken uit of energie kunt insturen in de magneet, nuttig voor het maken van thermodynamische motoren. Hoewel het bekend is dat de laser verwarmt, kan het, tegen intuïtief, een magneet koelen. Ik schrijf hoe dit afkoeling kan worden geoptimaliseerd en beargumenteer dat het haalbaar is om het experimenteel te observeren. We stellen ons onze theorie voor om technologie te ontwikkelen voor willekeurige manipulatie van spins met behulp van licht.

1

Introduction

Never underestimate the joy people derive from hearing something they already know.

Enrico Fermi

I introduce the background necessary for understanding our research on manipulating magnetization using light. This includes a theory of magnetic and optical modes in a sphere along with their interaction.

1

The 'bizarre' quantization of angular momentum observed in the classic Stern Gerlach experiment lead to the notion of spin. It is an intrinsic property of most elementary particles, analogous to rotation of a classical object. A macroscopic consequence thereof can be witnessed in a ferromagnet, which is distinguished by a strong tendency of neighbouring electrons to have parallel spins. In equilibrium, a ferromagnetic sample gets partitioned into domains, within each of which the spins of the electrons are parallel. By applying a sufficiently strong magnetic field, these domains get aligned and a large magnetic field is generated outside the sample.

Commercial applications of ferromagnets include hard disks, read and write media and sensitive gyroscopes [1]. They have benefits over conventional logic devices due to their non-volatility, reconfigurability and low-power consumption [2, 3]. Magnets which are electrically insulating are materials of choice for microwave technology such as filters and oscillators due to their high quality factors [4, 5]. A representative material for such is the ferrimagnet yttrium iron garnet (YIG) which, at low energies ($\sim 50\mu\mathrm{eV} \equiv 10\mathrm{GHz} \equiv 500\mathrm{mK}$), behaves as a ferromagnet [6]. Its high transparency at infrared and strong spin-orbit interaction makes it useful in commercial optical isolators (devices which allow transmission of light in only one direction). The elementary excitations of the magnetic order, called magnons, are long lived in YIG [6, 7]. This makes it promising for low power logic devices [8], and long-range information transfer [9].

In addition to long lifetimes, magnons in YIG are expected to have long coherence times [10], making them suitable for applications in quantum information [11]. However, studies on quantum properties of magnons are scarce and it is desirable to have an interface with high coherence such as photons. At microwave frequencies $\sim$ GHz, photons have $\sim$ cm wavelengths and can couple strongly even with magnons having sub-mm wavelengths [10, 12, 13]. However, the coupling is weaker for smaller samples and wavelengths. Optical light with frequencies ~ 100THz and sub-μm wavelengths is used to measure the dispersion of magnons in a wide range of wave-vectors [14, 15], known as Brillouin light scattering (BLS) spectroscopy. In this thesis, I argue that light can also be used to study and manipulate magnons at a quantum level.

BLS refers to inelastic scattering of photons by absorbing or creating magnons. Typical BLS measurements require strong light-matter interaction which are usually accompanied with high optical losses into the material. However, pioneering experiments on YIG spheres carried out independently in three labs [16–18] showed dynamical interaction between magnons and photons at wavelengths of transparency: $> 1.3\mu$m in free space. They found that magnon-photon coupling is enhanced by confining light inside the magnet, by using it as a whispering gallery mode (WGM) cavity. Predictions of using light to manipulate magnons followed, such as Purcell effect (optically enhanced linewidth of magnons) [19], chaos in magnetic order [20], and magnon cooling [21] (discussed in Chapter 4).

In this thesis, I theoretically discuss the interaction of infrared photons and magnons in a setup shown in Fig. 1.1. A ferromagnetic sphere is touching a proximity coupler (an optical fiber or a prism), whose transmission and reflection is affected by the magnons. In turn, with an input light of sufficiently high power, the

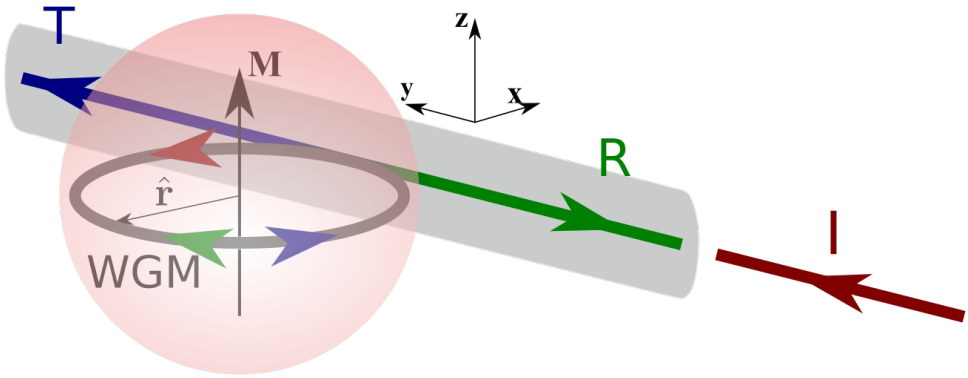

Figure 1.1: A magnetic sphere is coupled to an evanescent coupler to excite optical modes inside the sphere. Incident photons (I) in the coupler scatter inelastically by the magnetic order in the sphere, which can be observed in the reflected (R) and transmitted (T) light that leads back into the coupler. The corresponding counter-propagating WGMs are shown by green (R) and blue (T) colored arrows inside the sphere.

magnons can be pumped or cooled. I discuss interactions between spins of a ferromagnet in Sec. 1.1, and magnons in Sec. 1.2. The leading interaction Hamiltonian between magnons and photons is discussed in Sec. 1.3. The electromagnetic fields of WGMs is explained in Sec. 1.4. The theories in these sections are consolidated in Sec. 1.5, where the model used in the thesis is discussed. A brief description of each chapter in the thesis is contained in Sec. 1.6.

1.1. Magnetism

In this section, I introduce the microscopic interactions between the spins in a magnet, with a focus on Yttrium Iron Garnet (YIG), $Y_3Fe_5O_{12}$. This material has a complex unit (cubic) cell containing twenty Fe atoms with half-filled 3d shell (spin 5/2). Eight of these are bonded with oxygen atoms in an octahedral geometry and twelve in tetrahedal. The nearest neighbour Fe atoms, in two different surroundings, are anti-ferromagnetically coupled, making YIG a ferrimagnet. For energies $\ll 3\text{meV} \equiv 40\text{K} \equiv 1\text{THz}$, the spins are so strongly locked that we can treat the unit cell as a single spin $\mathbf{S}_i$ (spin $S = 10$) at sites $\mathbf{r}_i$. The neighbouring unit cells have an effective ferromagnetic interaction,

$$\mathcal{H}_{\text{ex}} = -J_{\text{ex}} \sum_{\langle ij \rangle} \mathbf{S}_i \cdot \mathbf{S}_j, \tag{1.1}$$

where $J_{\text{ex}} > 0$ is the strength of the ferromagnetic interaction and the summation is restricted to neighbouring unit cells. This exchange interaction is isotropic in YIG because the crystal is rotationally symmetric.

Non-neighbouring unit cells are coupled electromagnetically. For frequencies

$\sim 1-10$ GHz and distances smaller than $\sim$ mm, we can ignore the travel time of the photons, giving an instantaneous dipolar interaction

$$\mathcal{H}_{\text{dip}} = \sum_{ij} \frac{-\mu_0 \gamma^2 \hbar^2}{4\pi r_{ij}^5} \left[3\left(\mathbf{S}_i \cdot \mathbf{r}_{ij}\right)\left(\mathbf{S}_j \cdot \mathbf{r}_{ij}\right) - \mathbf{S}_i \cdot \mathbf{S}_j r_{ij}^2\right], \tag{1.2}$$

where μ_0 is the permeability of free space, $\mathbf{r}_{ij} = \mathbf{r}_i - \mathbf{r}_j$, and $\gamma > 0$ is the absolute value of the gyromagnetic ratio. $\gamma\hbar\mathbf{S}_i$ is the magnetic moment.

For magnons with wavelengths comparable to or larger than infrared photons, $\sim \mu$m, the neighbouring spins separated by a lattice constant, $a = 1.2$nm in YIG, are nearly parallel. Thus, we can define a continuous magnetization field $\mathbf{M}(\mathbf{r})$ such that $\mathbf{M}(\mathbf{r}_i) = -\gamma\hbar N_s \mathbf{S}_i$. The saturation magnetization $M_s = \gamma\hbar S N_s$ is the magnetic moment per unit volume when all the spins are aligned. In YIG, $M_s = 1.4 \times 10^5$ kA/m.

The Hamiltonian for the magnetization, including the dipolar and exchange interaction,

$$\mathcal{H}_{\text{m}} = -\mu_0 \int dV \left[\frac{\mathbf{M} \cdot \mathbf{H}_{\text{dip}}}{2} - \frac{1}{2k_{\text{ex}}^2} \nabla\mathbf{M} \cdot \nabla\mathbf{M} + \mathbf{M} \cdot \mathbf{H}_{\text{ext}}\right]. \tag{1.3}$$

The dipolar field generated by the magnetization can be found by solving magnetostatic equations,

$$\nabla \times \mathbf{H}_{\text{dip}} = 0, \quad \nabla \cdot \mathbf{H}_{\text{dip}} = -\nabla \cdot \mathbf{M}, \tag{1.4}$$

The exchange interaction is quantified by the inverse length scale

$$k_{\text{ex}} = \sqrt{\frac{\mu_0 a M_s^2}{2S^2 J_{\text{ex}}}}. \tag{1.5}$$

For YIG, $\lambda_{\text{ex}} = 2\pi/k_{\text{ex}} = 109$nm. If the spatial variation of the magnetization is on length scales much larger (smaller) than λ_{ex}, dipolar (exchange) interaction is dominant. $\mathbf{H}_{\text{ext}}$ is an external field typically uniform and large enough to ensure that the ground state of the magnetization is uniform.

1.2. Magnetostatic modes

We derive the spatial distribution of the elementary excitations of a ferromagnet, called magnons. For a sufficiently large external field $\mathbf{H}_{\text{ext}} = H_{\text{app}}\mathbf{z}$ the magnetization has small fluctuations around its ground state, $M_s\mathbf{z}$: $\mathbf{M} = M_s\mathbf{z} + M_x\mathbf{x} + M_y\mathbf{y}$ with $|M_x|, |M_y| \ll M_s$. To leading order, $\mathbf{M}.\mathbf{M} = M_s^2$ because of a strong exchange locking. For magnons with wavelengths $\gg \lambda_{\text{ex}}$, the exchange term in Eq. (1.3) can be ignored. We expand the magnetization in the eigenstates of the Hamiltonian

$$M_x(\mathbf{r}, t) = \sum_A \left[M_{x,A}(\mathbf{r}) m_A(t) + M_{x,A}^*(\mathbf{r}) m_A^*(t)\right], \tag{1.6}$$

where A is a mode index, and m_A is the amplitude of A-magnon mode. Similar expansion with $x \to y$ holds. The mode index $A \equiv \{l, m, \nu\}$ consists of three integers

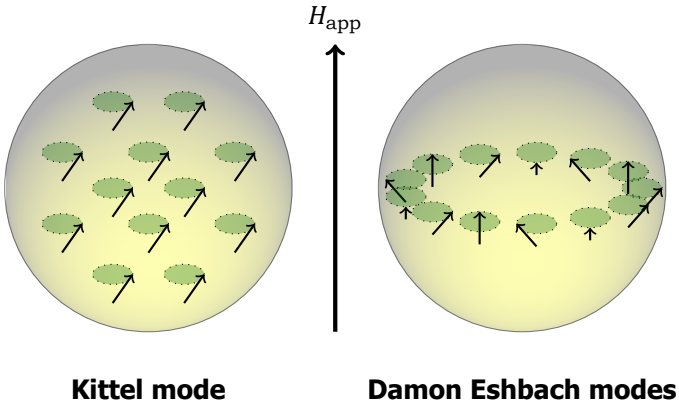

Figure 1.2: Schematic of the Kittel mode and the Damon Eshbach modes. The Kittel mode is a uniform precession of the magnetzation around the applied magnetic field. The Damon-Eshbach modes are localized near the equator with linearly increasing phase along the azimuthal.

with the following interpretation (discussed in more detail in App. 1.7). The z-component of angular momentum of one magnon in A-mode is $m\hbar$. Both M_x and M_y have $l-m>0$ elliptical nodal planes. $0\leq\nu\leq l-m$ is the number of prolate nodal planes. The total angular momentum is not defined for a mode because of rotational symmetry breaking by the applied magnetic field.

The magnetic fields are normalized as [see Eq. (1.69)],

$$\int dV\ \mathrm{Im}\left[M^*_{x,A}M_{y,A}\right]=\int dV\ \mathrm{Im}\left[M^*_{\rho,A}M_{\phi,A}\right]=\frac{\hbar\gamma M_s}{2}, \tag{1.7}$$

where $M_\rho=M_x\cos\phi+M_y\sin\phi$ and $M_\phi=M_y\sin\phi-M_x\cos\phi$ are the components in cylindrical coordinates, and $\mathrm{Im}\left[*\right]$ is the imaginary part. This normalization is chosen to ensure that the Hamiltonian becomes

$$\mathcal{H}_{\mathrm{m}}=\sum\hbar\omega_A\left|m_A\right|^2, \tag{1.8}$$

where ω_A is the resonance frequency of A-mode.

While the full expressions for $\mathbf{M}_A$ are complicated [22, 23], discussed in App. 1.7, we discuss some special cases. $K\equiv\{1,1,0\}$ corresponds to the Kittel mode, given by a uniform circular precession of the magnetization [see Fig. 1.2]

$$M_{\phi,K}=iM_{\rho,K}=\sqrt{\frac{\hbar\gamma M_s}{2V_{\mathrm{sph}}}}, \tag{1.9}$$

where V_{sph} is the volume of the sphere. Its resonant frequency is $\omega_K=\gamma\mu_0H_{\mathrm{app}}$.

$D\equiv\{l,l,0\}$ (ν is always zero for $l=m$), with $l\gg1$, corresponds to circularly

polarized surface modes, called Damon Eshbach (DE) modes [see Fig. 1.2],

$$M_{\phi,D} = iM_{\rho,D} = \left(\frac{l}{\pi}\right)^{3/4} \sqrt{\frac{\hbar\gamma M_s}{R^3}} \left(\frac{\rho}{R}\right)^{l-1}, \tag{1.10}$$

where R is the radius of the sphere. This mode is highly localized at the surface and has a small azimuthal wavelength $\approx R/l$. Its resonance frequency

$$\omega_D = \gamma\mu_0 \left[H_{\text{app}} - \frac{M_s}{3} + \frac{lM_s}{2l+1}\right]. \tag{1.11}$$

For large l, the DE modes are nearly degenerate and can hybridise even with small perturbations like surface pinning. At smaller wavelengths near λ_{ex}, exchange interaction becomes important as discussed in Ch. 5, which breaks this degeneracy.

A similar analysis for $m = -l$ gives a negative resonance frequency for all l, implying that DE modes move only in one direction [see Fig. 1.2].

1.3. Magneto-optical interaction

Optical light couples to the magnetic order, leading to static and dynamic effects discussed here. In a dielectric, photons are retarded by electrons due to (typically virtual) absorption and subsequent re-emission, which can be modelled as a renormalization of permittivity $\mathbf{D} = \epsilon\mathbf{E}$ where $\mathbf{D}$ is the displacement vector, $\mathbf{E}$ the electric field, and ϵ is a material parameter. This holds for an isotropic and linear dielectric with a weak dispersion. In the presence of spin-orbit coupling, the scattering processes are influenced by spins, giving $\mathbf{D}(\mathbf{r}) = \overline{\epsilon}\,[\mathbf{M}(\mathbf{r})]\,\mathbf{E}(\mathbf{r})$ where $\overline{\epsilon}$ is a 3×3 tensor because the magnetization breaks the rotational symmetry. This holds for slow dynamics of the spins, in our case $\sim$ GHz, compared to the optical frequencies, ~ 100THz.

Below, in Sec. 1.8, we derive

$$\mathbf{D} = \epsilon_s\mathbf{E} + if\mathbf{M}\times\mathbf{E} + g\mathbf{M}\,\mathbf{M}\cdot\mathbf{E}, \tag{1.12}$$

where $\{\epsilon_s, f, g\}$ are material parameters.

Consider a sample with a static magnetization $\mathbf{M} = M_s\boldsymbol{z}$ and light propagating along $\boldsymbol{z}$. Eq. (1.12) can be simplified to

$$D_\pm = (\epsilon_s \mp fM_s)\,E_\pm, \tag{1.13}$$

where $F_\pm = F_x \pm iF_y$ are the circular components. The refractive indices for the two circularly polarized components are different, $n_\pm = \sqrt{(\epsilon_s \mp fM_s)/\epsilon_0}$, an effect known as 'magnetic circular birefrigence'. If a linearly polarized light travels a distance l within the sample, the two circularly polarized components will acquire a phase shift of $(n_+ - n_-)k_0 l$ where k_0 is the free-space wave-vector. Thus, the polarization rotates by an angle $\Theta_F l$ where

$$\Theta_F = \frac{(n_+ - n_-)k_0}{2} \approx -\frac{\pi f M_s}{\lambda_0\epsilon_0 n_s}, \tag{1.14}$$

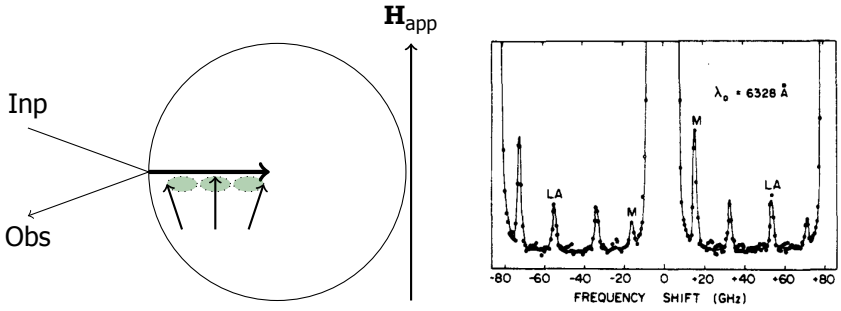

Figure 1.3: A typical BLS experiment to find the dispersion relations of magnons. The input photons are inelastically reflected by magnons, gaining or losing energy in the process. The reflected spectrum is shown on the right, where the origin is the incident frequency. It shows peaks at higher (lower) energy than the central peak corresponding to absorption (emission) of magnons. The experimental picture is taken from Ref. [14]

assuming small magneto-optical effects $fM_s \ll \epsilon_s$ and $n_s = \sqrt{\epsilon_s/\epsilon_0}$ is the average refractive index. This effect, known as Faraday rotation, occurs in the same sense regardless of the photons' direction. This time-reversal symmetry breaking is employed in commercial YIG based optical isolators. This effect can be used to measure f but is insensitive to g.

For light propagating in $\mathbf{x}$ direction and magnetization $\mathbf{M} = M_s\mathbf{z}$, the two polarizations satisfy $D_y = \epsilon_s E_y$ and $D_z = (\epsilon_s + gM_s^2)E_z$, implying a 'magnetic linear birefringence'. Consider a light polarized linearly along $\mathbf{y}+\mathbf{z}$ traveling for a distance l sufficiently small such that $(n_z - n_y)k_0 l \ll 1$ where $n_z = \sqrt{(\epsilon_s + gM_s^2)/\epsilon_0}$ and $n_y = \sqrt{\epsilon_s/\epsilon_0}$. In this small distance the polarization will become elliptic with $\Theta_{CM} l$ being the ratio of minor and major axis, where

$$\Theta_{CM} = \frac{2\pi(n_z - n_y)}{\lambda_0} \approx \frac{\pi g M_s^2}{\lambda_0 \epsilon_0 n_s}. \tag{1.15}$$

This effect is called the 'Cotton-Mouton effect', and can be used to find g. In YIG, $\Theta_{CM} \sim \Theta_F$.

Next, consider Larmor precession $\mathbf{M} = M_s\mathbf{z} + m\,[\cos(\omega_m t)\mathbf{x} + \sin(\omega_m t)\mathbf{y}]$ where m is proportional to the number of magnons in Kittel mode. For a monochromatic incident light, $\mathbf{E} \sim e^{-i\omega_p t}$, sidebands at $\omega_p \pm \omega_m$ arise in $\mathbf{D}$. They correspond to photons which have absorbed energy from or emitted to the magnons, as shown in Fig. 1.3 (the figure shows non-uniform magnons and not the Kittel mode). The reflected spectrum, shown on the right, shows that a large number of photons are reflected elastically, but a small number absorbed or created magnons (the sidebands marked by M in Fig. 1.3). We discuss this in more detail in the rest of the thesis in the context of whispering gallery cavities.

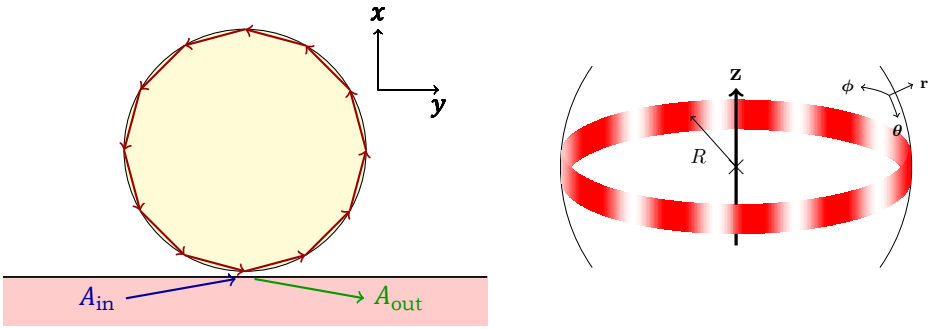

Figure 1.4: The photons traveling via the fiber can leak into the sphere and be quasi-trapped via repeated total internal reflection. The quasi-trapped photons have a small probability to leak out into the fiber and interfere with the tranmitted photons. The electromagnetic fields form a wave inside the sphere which is highly localized near the equator. The explicit expressions are discussed in the text.

1.4. Whispering gallery modes

In conventional BLS experiments, the magnon-photon coupling is strong enough to study magnons but too weak to influence their state. However, we can increase the interaction time by confining light inside the magnet. In Fig. 1.4 [cross-section of Fig. 1.1], a proximity coupler, typically a fiber or a prism, is kept in contact with a ferromagnetic sphere. The photons traveling in the coupler can leak into the sphere because of their evanescent electric fields and be confined because of repeated total internal reflection. The right hand side of Fig. 1.4 shows a schematic of the optical modes excited inside the sphere, which are confined near the equator and traveling in azimuthal direction. In this section, we describe the electric field distributions of these optical modes, known as whispering gallery modes (WGMs).

The effect of the magnetization on optical properties is weak and can be treated perturbatively [25], and thus $\epsilon_{ij} = \epsilon_s \delta_{ij}$. At optical frequencies, the susceptibility of the magnetization is negligible [5], so $\mu_0 \mathbf{H} = \mathbf{B}$. The Hamiltonian for the electromagnetic fields (equivalent to the Maxwell's equations) is

$$\mathcal{H}_{\text{em}} = \int dV \left[\frac{\epsilon(\mathbf{r}) \mathbf{E}^2(\mathbf{r})}{2} + \frac{\mu_0 \mathbf{H}^2(\mathbf{r})}{2} \right]. \tag{1.16}$$

The permittivity, $\epsilon(\mathbf{r})$ is constant is each region: ϵ_s in the sphere, ϵ_f in the coupler and ϵ_0 in free space.

The electromagnetic fields inside the sphere can be expanded in a complete set of solutions of the Maxwell's equations,

$$\mathbf{E}(\mathbf{r}, t) = \sum_P \left[\alpha_P(t) \mathbf{E}_P(\mathbf{r}) + \alpha_P^*(t) \mathbf{E}_P^*(\mathbf{r}) \right], \tag{1.17}$$

$$\mathbf{H}(\mathbf{r}, t) = \sum_P \left[\alpha_P(t) \mathbf{H}_P(\mathbf{r}) + \alpha_P^*(t) \mathbf{H}_P^*(\mathbf{r}) \right], \tag{1.18}$$

where the label $P \equiv \{l, m, \nu, \sigma\}$ (to be discussed), $\alpha_P(t)$ is the amplitude of the P-th mode and $\omega_P > 0$ is the resonance frequence of P-th mode.

With no input or dissipation, $\alpha_P(t) \sim e^{-i\omega_P t}$. For correspondence with quantum treatment, we would like $|\alpha_P|^2$ to equal the number of photons [see Sec. 1.5.1]. This is achieved by normalization,

$$\int dV \left[\frac{\epsilon(\mathbf{r})|\mathbf{E}_P|^2}{2} + \frac{\mu_0 |\mathbf{H}_P|^2}{2} \right] = \frac{\hbar\omega_P}{2}, \tag{1.19}$$

ensuring that the Hamiltonian, Eq. (1.16),

$$\mathcal{H}_{\text{em}} = \sum_P \hbar\omega_P |\alpha_P^2(t)|. \tag{1.20}$$

We now discuss the electromagnetic fields for a subset of the indices $P = \{l, m, \nu, \sigma\}$ corresponding to WGMs.

The WGMs have a wave dependence in azimuthal ϕ-direction, $\mathbf{E} \sim e^{im\phi}$, where $2\pi R/m$ can be interpreted as their wavelength. Typically, the radius of the sphere is much larger than the wavelength, thus $m \sim 1000 - 5000$. $\hbar m$ is the z-component of the angular momentum of one photon in this mode.

The electric field is confined in polar θ-direction (Gaussian dependence)

$$\mathbf{E} \sim \exp\left[-\frac{m\Theta^2}{2} \right] H_{l-m}\left(\sqrt{m}\Theta\right), \tag{1.21}$$

where $\Theta = \pi/2 - \theta$, H_{l-m} is the Hermite polynomial,

$$H_n(x) = (-1)^n e^{x^2} \frac{d^n e^{-x^2}}{dx^n}. \tag{1.22}$$

The first few Hermite polynomials are

$$H_0(x) = 1, \quad H_1(x) = 2x, \quad H_2(x) = 4x^2 - 2, \quad H_3(x) = 8x^3 - 12x. \tag{1.23}$$

The electric field has no polar nodes for $l = m$ and decays away from the equator with an angular scale $\sim 1/\sqrt{m}$. The Hermite polynomial introduces $l - m$ nodes and also expands the field in θ-direction. Thus, modes excited with the fiber typically have a small $l - m \sim 1$. $\hbar l$ is the total angular momentum of a photon in this mode.

The radial distribution is given by

$$\mathbf{E} \sim \text{Ai}\left(\tilde{r} - \beta_\nu\right), \tag{1.24}$$

where Ai is the Airy function (defined as an improper integral)

$$\text{Ai}\,(x) = \frac{1}{\pi} \int_0^\infty \cos\left(\frac{t^3}{3} + xt \right) dt, \tag{1.25}$$

the expanded 'radial' coordinate

$$\tilde{r} = 2^{1/3} m^{2/3} \left(1 - \frac{r}{R} \right), \tag{1.26}$$

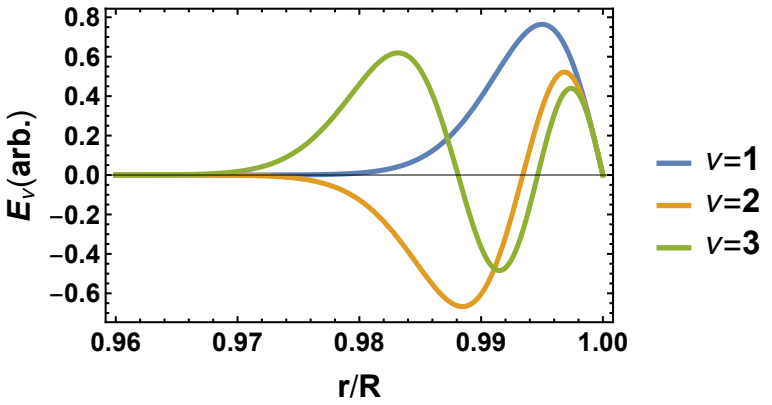

Figure 1.5: The radial distribution of the electric fields for $m = 3000$. ν gives the number of nodes and larger ν corresponds to lesser confinement.

and ν-th zero of Ai $(-x)$ is β_ν. The Airy function decays in the positive real axis and thus, the electric field strongly decays away from the surface, because $m^{2/3} \gg 1$, and typically the field is zero for $r/R < 0.95$ [see Fig. 1.5]. The electric field is nearly zero at the surface and achieves a peak close to $r/R = 1 - 1/m^{2/3}$ for $\nu = 1$.

As the WGMs travel in the azimuthal direction, they have two polarizations primarily parallel to $\mathbf{r}$ and $\boldsymbol{\theta}$. In the former (latter) case the magnetic (electric) field has no component along the azimuthal and are thus called transverse magnetic (electric), labelled by $\sigma \in \{\text{TE}, \text{TM}\}$.

The frequency of the photons can be written in terms of the wave-vector $\omega = kc/n_s$. As discussed above, $kR \approx m$ because of the azimuthal depenence $e^{im\phi}$ but there are significant corrections because the electric fields have a finite depth $\Delta \propto m^{-2/3}$, into the sphere, giving $k(R-\Delta) \approx m$. More precisely, for $l, m \gg 1, |l-m|$

$$kR \approx l + \beta_\nu \left(\frac{l}{2}\right)^{1/3} - P_\sigma, \tag{1.27}$$

where $P_{\text{TE}} = n_s/\sqrt{n_s^2 - 1}$ and $P_{\text{TM}}^{-1} = n_s\sqrt{n_s^2 - 1}$. The polar contribution is small, $l - m$, and typically difficult to observe. The radial contribution, $\propto \beta_\nu$, is comparatively larger and represents the fact that modes with larger ν are further inside the sphere. The last contribution, P_σ, is because of different boundary conditions for the electric and magnetic fields, leading to a small difference in the depths of the two polarizations.

1.5. Model

We consolidate the discussion of magnons, WGMs and magnon-photon coupling in this section, introducing the model used in the thesis. The total Hamiltonian

$$\mathcal{H} = \int dV \left[\frac{\mathbf{E}.\mathbf{D}}{2} + \frac{\mu_0 \mathbf{H}.\mathbf{H}}{2} - \frac{\mu_0 \mathbf{M} \cdot \mathbf{H}_{\text{dip}}}{2} - \mu_0 M_z H_{\text{app}} + \frac{\mu_0}{2k_{\text{ex}}^2} \nabla\mathbf{M}.\nabla\mathbf{M} \right], \tag{1.28}$$

where $\mathbf{E}$ and $\mathbf{H}$ are fields at optical frequencies (removing the dipolar contribution $\mathbf{H}_{\text{dip}}$). The last three terms are the magnetic Hamiltonian, Eq. (1.3). The first two terms are the electromagnetic Hamiltonian, Eq. (1.16), which also contain the magneto-optical interaction via $\mathbf{D} = \bar{\epsilon}\,[\mathbf{M}]\,\mathbf{E}$, Eq. (1.12).

These are equivalent to the coupled set of equations,

$$\begin{aligned} &\boldsymbol{\nabla} \times \mathbf{E} = \frac{-\partial \mathbf{B}}{\partial t},\ \boldsymbol{\nabla} \times \mathbf{H} = \frac{\partial \mathbf{D}}{\partial t}, \\ &\boldsymbol{\nabla} \cdot \mathbf{B} = 0,\ \boldsymbol{\nabla} \cdot \mathbf{D} = 0, \\ &\frac{\partial \mathbf{M}}{\partial t} = -\gamma\mu_0 \mathbf{M} \times \left(\mathbf{H} + H_{\text{app}} \boldsymbol{z} + \frac{1}{k_{\text{ex}}^2} \nabla^2 \mathbf{M} + \frac{1}{2} \sum_{ij} \nabla_{\mathbf{M}} \bar{\epsilon}_{ij}\ E_i^* E_j \right). \end{aligned} \tag{1.29}$$

The operator $\nabla_{\mathbf{M}}$ is the functional derivative with respect to the magnetization.

The boundary conditions for electromagnetic fields are the continuity of $\{\mathbf{E}_\parallel, B_\perp, D_\perp, \mathbf{H}_\parallel\}$, where $*_\parallel$ and $*_\perp$ are respectively the components of $*$ parallel and perpendicular to the surface. For the magnetization, the boundary condition is modelled as [26–28]

$$\mathbf{n}.\boldsymbol{\nabla} m_{x,y} - d m_{x,y} = 0, \tag{1.30}$$

where d is the ratio of surface anisotropy and exchange with shape-dependent corrections from long range dipolar interaction. The exact form of d is not important for our purposes.

1.5.1. Quantization

The above classical theory can be canonically quantized by expanding the fields in terms of normal modes [Eqs. (1.17), (1.18), and (1.6)] and promoting the expansion coefficients to quantum operators,

$$\hat{X}(\mathbf{r}) = \sum_P \left[\hat{a}_P X_P(\mathbf{r}) + \hat{a}_P^\dagger X_P^*(\mathbf{r}) \right], \tag{1.31}$$

$$\hat{Y}(\mathbf{r}) = \sum_R \left[\hat{m}_R Y_R(\mathbf{r}) + \hat{m}_R^\dagger Y_R^*(\mathbf{r}) \right], \tag{1.32}$$

for $X \in \{E_x, E_y, E_z, B_x, B_y, B_z\}$ and $Y \in \{M_\rho, M_\phi\}$, where $\{\hat{a}_P\}$ and $\{\hat{m}_R\}$ are the set of WGM and magnon annihilation operators satisfying $\left[\hat{a}_P, \hat{a}_Q^\dagger\right] = \delta_{PQ}$, $\left[\hat{m}_R, \hat{m}_S^\dagger\right] = \delta_{rs}$ and all other commutators being zero.

1

We promote the classical Hamiltonian to a quantum Hamiltonian

$$\hat{H} = \sum_P \hbar\omega_P \hat{a}_P^\dagger \hat{a}_P + \sum_R \hbar\omega_R \hat{m}_R^\dagger \hat{m}_R + \sum_{PQR} \hbar \hat{a}_P \hat{a}_Q^\dagger \left[G_{PQR}^+ \hat{m}_R + G_{PQR}^- \hat{m}_R^\dagger\right], \quad (1.33)$$

where ω_P and ω_R are respectively the frequencies of the P labelled WGMs and R labelled magnons. We define the coupling constants,

$$G_{PQR}^+ = \frac{n_s \epsilon_0 \lambda_0}{\pi M_s} \int dV \left[i\Theta_F \mathbf{M}_R . \left(\mathbf{E}_P \times \mathbf{E}_Q^*\right) + \Theta_{CM} \mathbf{M}_R . \left(E_{Pz} \mathbf{E}_Q^* + E_{Qz}^* \mathbf{E}_P\right)\right], \quad (1.34)$$

and $G_{PQR}^- = (G_{QPR}^+)^*$. They will be discussed in more detail in later chapters.

1.5.2. Input and dissipation

The Hamiltonian Eq. (1.33) is energy conserving and therefore, does not contain information about input light propagating in the fiber and dissipation of magnons and photons inside the ferromagnetic sphere. We add these phenomenologically in the Heisenberg equation of motion as discussed in this section.

The magnons in YIG are dissipated because of phonons and other magnons. A simple model which generates a canonical Gibbs distribution in steady state, in the absence of an input, [29]

$$\frac{d\hat{m}_R}{dt} = \frac{i}{\hbar}\left[\hat{H}, \hat{m}_R\right] - \frac{\kappa_R}{2}\hat{m}_R - \sqrt{\kappa_R}\hat{b}_R, \quad (1.35)$$

where κ_R is the linewidth and $\hat{b}_R$ is a noise source that obeys the fluctuation-dissipation theorem [30, 31]. When $\kappa_R \ll k_B T/\hbar$, which is satisfied for $\kappa_R \sim 2\pi \times 1$ MHz [16–18] and $T \gg 50\mu$K, the (narrow band filtered) noise is effectively white. Their statistics are $\left\langle \hat{b}_R(t) \right\rangle = 0$, $\left\langle \hat{b}_R^\dagger(t') \hat{b}_R(t) \right\rangle = n_R \delta(t - t')$ and $\left\langle \hat{b}_R(t') \hat{b}_R^\dagger(t) \right\rangle = (n_R + 1)\delta(t - t')$, where the Bose distribution

$$n_R = \left[\exp\left(\frac{\hbar\omega_R}{k_B T}\right) - 1\right]^{-1}. \quad (1.36)$$

This model does not distinguish between decoherence and energy dissipation, both of them happening at the same rate κ_R.

The WGMs are modelled as [see App. 1.9],

$$\frac{d\hat{a}_P}{dt} = \frac{i}{\hbar}\left[\hat{H}, \hat{a}_P\right] - \frac{\kappa_P + K_P}{2}\hat{a}_P - \sqrt{\kappa_P}\hat{b}_P - \sqrt{K_P}\hat{A}_P, \quad (1.37)$$

where $\hat{b}_P$ is a noise operator while $\hat{A}_P$ in the input from the fiber. κ_P is the intrinsic linewidth and K_P is the rate of leakage of P-WGM into the fiber. The noise source is again taken to be white for sufficiently small κ_P: $\left\langle \hat{b}_P(t) \right\rangle = 0$, $\left\langle \hat{b}_P^\dagger(t') \hat{b}_P(t) \right\rangle = 0$ and $\left\langle \hat{b}_P(t') \hat{b}_P^\dagger(t) \right\rangle = \delta(t - t')$ because the thermal occupation of photons at infrared and visible frequencies is negligibly small at room temperature $e^{-\hbar\omega_P/(k_B T)} \approx 0$.

The input from fiber can be just thermal noise for modes off-resonant with the input, in which case it has the same correlator as $\hat{b}_P$. For a coherent input at frequency ω_{in} and power P_{in},

$$\left\langle \hat{A}_P^\dagger(t)\hat{A}_P(t')\right\rangle = \frac{P_{\text{in}}}{\hbar\omega_{\text{in}}}e^{-i\omega_{\text{in}}(t'-t)}. \tag{1.38}$$

The above equations are solved and discussed in more detail in the chapters of the thesis.

1.6. Structure of the thesis

Using the basics of optical and magnonic fields introduced in this chapter, we proceed to discuss their outcomes in the rest of the thesis. We derive the transmission and reflection spectrum in the fiber, affected by the inelastic scattering of photons by magnons in Ch. 2. This gives us the selection rules for magnon-WGM coupling by simplifying the coupling constants, Eq. (1.34). We consider only magnetostatic modes here. The selection rules are expanded upon in Ch. 3 by focusing only on the long wavelength magnons. Experiments to verify these selection rules are discussed. An application, namely active cooling of magnons via optical light, is introduced in Ch. 4, where we derive the steady state distribution of magnons for a coherent light input. The analysis in Ch. 2 is generalized to include exchange interaction in Ch. 5 important for magnons with small wavelength. We derive the spatial distribution of magnons which have the maximum overlap with the electromagnetic fields and find their coupling strengths.

1.7. Appendix: Magnons in a sphere

The eigenmodes of the magnetization are found using Eq. (1.29) at microwave frequencies. If the radius of the sphere $R \ll c/\omega$, where ω is a typical frequency of magnons, the photons propagate almost instantaneously across the magnet and magnetostatic approximation holds: $\mathbf{E} = 0$. This condition is satisfied for $R < 0.5$mm for frequencies $\omega < 2\pi \times 10$GHz. The effect of light on magnons is ignored here and will be treated perturbatively in Chapter 2.

The effective model at microwave frequencies is,

$$\begin{aligned} \boldsymbol{\nabla}\times\mathbf{H}_{\text{dip}} = 0,\quad \boldsymbol{\nabla}\cdot\mathbf{H}_{\text{dip}} = -\boldsymbol{\nabla}\cdot\mathbf{M} \\ \frac{\partial\mathbf{M}}{\partial t} = -\gamma\mu_0\mathbf{M}\times\left(H_{\text{app}}\mathbf{z} + \mathbf{H}_{\text{dip}} + \frac{1}{k_{\text{ex}}^2}\nabla^2\mathbf{M}\right). \end{aligned} \tag{1.39}$$

By linearity of Maxwell's equations, the dipolar field $\mathbf{H}_{\text{dip}} = -M_s/3\mathbf{z} + \mathbf{h}$ where $\mathbf{h}$ is due to $\mathbf{m}$. The equations can be simplified by introducing a scalar magnetic potential $\mathbf{h} = -\boldsymbol{\nabla}\psi$ and Fourier transforming in time,

$$X(\omega) = \int_{-\infty}^{\infty}\frac{dt}{\sqrt{2\pi}}e^{i\omega t}X(t). \tag{1.40}$$

1

By linearization, we get

$$m_{\pm} = \frac{-\omega_s}{\pm\omega + \omega_a}\left[\partial_{\pm}\psi - \frac{\nabla^2 m_{\pm}}{k_{\text{ex}}^2}\right], \tag{1.41}$$

where $\omega_s = \gamma\mu_0 M_s$, $\omega_a = \gamma\mu_0\left(H_{\text{app}} - M_s/3\right)$, the circular coordinates $m_{\pm} = m_x \pm i m_y$, and $\partial_{\pm} = \partial_x \pm i\partial_y$

For $\lambda \gg \lambda_{\text{ex}}$, we can ignore the exchange term. We will reintroduce it in Chapter 5 when we discuss smaller wavelength magnons. Then, the equation of motion for ψ inside the sphere,

$$\left[\partial_x^2 + \partial_y^2 - \frac{\partial_z^2}{\mathcal{E}^2}\right]\psi = 0, \tag{1.42}$$

where

$$\mathcal{E}^2 = \frac{\omega_s\omega_a}{\omega^2 - \omega_a^2} - 1. \tag{1.43}$$

For bulk magnons $\omega < \sqrt{\omega_a^2 + \omega_s\omega_a}$ (found a posteriori [22]), and thus $\mathcal{E}$ is real. $\mathcal{E}$ is imaginary for surface modes but the final solution is still valid (discussed in more detail below).

Outside the sphere, $\mathbf{m} = 0$ and

$$\nabla^2\psi_o = 0. \tag{1.44}$$

1.7.1. Solution

Eq. (1.42) is similar to a Laplacian but with a negative pre-factor for ∂_z^2. If we let $z \to z\mathcal{E}$, the sphere becomes a spheroid, where a Laplacian can be solved by spheroidal coordinates. To account for the negative sign in front of ∂_z^2, we use a variation: $\{\eta, \zeta, \phi\}$ defined by

$$\rho = R\sqrt{1+\mathcal{E}^2}\sin\eta\sin\zeta, \tag{1.45}$$

$$\mathcal{E}z = R\sqrt{1+\mathcal{E}^2}\cos\eta\cos\zeta, \tag{1.46}$$

and ϕ being the azimuthal angle. Here $\rho = \sqrt{x^2+y^2}$. We allow $\eta \in [0, \Theta)$, and $\zeta \in [\Theta, \pi - \Theta]$, where

$$\Theta = \sin^{-1}\frac{1}{\sqrt{1+\mathcal{E}^2}}. \tag{1.47}$$

The above restriction ensures $\rho^2 + z^2 \leq R^2$ and uniqueness of coordinate transformation. At $\eta \to \Theta$, we get $\zeta \to \theta$ where θ is the polar coordinate. If $\mathcal{E}^2 < 0$, we can use spheroidal coordinates by $\sin\zeta \to \sinh\zeta$ and $\cos\zeta \to \cosh\zeta$, while the calculations below follow analogously.

In these coordinates, Eq. (1.42) becomes,

$$\left[\partial_\zeta^2 - \partial_\eta^2 - \tan\zeta\partial_\zeta + \tan\eta\partial_\eta + \left(\frac{1}{\cos^2\zeta} - \frac{1}{\cos^2\eta}\right)\partial_\phi^2\right]\psi = 0. \tag{1.48}$$

By Fourier transforming in ϕ-direction and separation of variables, we get

$$\psi = \sum_{lm\nu} \tilde{\alpha}_{lm\nu} P_l^m(\cos\zeta) P_l^m(\cos\eta) e^{im\phi}, \tag{1.49}$$

where $l > 0$, $\nu > 0$, and m are integers satisfying $l \geq |m|$. ν is defined below. This gives the magnetization

$$m_\pm = \sum \frac{-\tilde{\alpha}_P \omega_s \; e^{i(m\pm1)\phi}}{\pm\omega_P + \omega_a} \left(\partial_\rho \mp \frac{m}{\rho}\right) P_l^m(\cos\zeta) P_l^m(\cos\eta). \tag{1.50}$$

Explicit differentiation gives long expressions tabulated in [23].

Outside the sphere, we find

$$\psi_o = \left(\frac{R}{r}\right)^{l+1} P_l^m(\cos\Theta) P_l^m(\cos\theta) e^{im\phi}, \tag{1.51}$$

in polar coordinates. The pre-factor is chosen to ensure continuity of ψ required for finiteness of $\mathbf{h}$.

We implement the boundary condition of continuity of $\mathbf{h}_r + \mathbf{m}_r$. By simple algebra,

$$\cos\Theta (\log P_l^m)'(\cos\Theta) - \frac{m\omega\omega_s}{\omega^2 - \omega_a^2} + l + 1 = 0. \tag{1.52}$$

For each l, m, there are $[(n - |m|)/2]$ solutions for $m < 0$ and $[(n - |m|)/2] + 1$ for $m > 0$ which are labelled as ν.

For $l = m$, $P_l^l(\cos\theta) \propto \sin^l\theta$ and

$$\psi \propto \rho^l e^{il\phi}. \tag{1.53}$$

This gives the magnetization,

$$m_\phi = m_0 \rho^{l-1} e^{il\phi}, \quad m_\rho = -i m_\phi, \tag{1.54}$$

where m_0 is a normalization constant (to be discussed below). The frequency of the mode using Eq. (1.52),

$$\omega_m = \omega_a + \frac{l\omega_s}{2l+1}. \tag{1.55}$$

The mode with $l = m = 1$ is called the Kittel mode in which the magnetization is uniform with frequency $\omega_m = \gamma\mu_0 H_{\text{app}}$. The modes with $l = m \gg 1$ are Damon Eshbach (DE) surface modes where the magnetization decays rapidly away from the surface. They are degenerate at $\omega_m = \omega_a + \omega_s/2$. This degeneracy is broken by exchange [27].

With $l = -m$, using $P_l^{-l}(\cos\theta) \propto \sin^l\theta$, we get $m_{\rho,\phi} \to m^*_{\rho,\phi}$ and $\omega_m \to -\omega_m$. Therefore, it is simply a complex conjugate of the other mode. This shows that DE modes are chiral, i.e. there are magnons which have an angular momentum parallel to the equilibrium magnetization but not anti-parallel. This fact is important when it comes to magnon-photon scattering discussed in Ch. 2.

1

1.7.2. Normalization

The Hamiltonian (1.28) in the absence of electromagnetic fields and linearized in small magnetization reads [5]

$$H = -\mu_0 \int \left[\left(H_{\text{app}} - \frac{M_s}{3} \right) M_z + \frac{\mathbf{m} \cdot \mathbf{h}_{\text{eff}}}{2} \right] dV, \tag{1.56}$$

where

$$\mathbf{h}_{\text{eff}} = \frac{2A_{ex}}{\mu_0 M_s^2} \nabla^2 \mathbf{m} + \mathbf{h}_{\text{dip}}. \tag{1.57}$$

The expansion in Eq. (1.6),

$$A(\mathbf{r}) = \sum_{P, \omega_P > 0} \left[A_P(\mathbf{r}) \alpha_P + A_P^*(\mathbf{r}) \alpha_P^* \right], \tag{1.58}$$

where A_P is the amplitude of any of $\{m_x, m_y, h_x, h_y\}$ of the P-th mode. Here and below the sum is restricted to positive frequencies. We have $\omega_a = \gamma \mu_0 (H_{\text{app}} - M_s/3)$, $\omega_s = \gamma \mu_0 M_s$, and

$$M_z \approx M_s - \frac{m_x^2 + m_y^2}{2M_s}. \tag{1.59}$$

Eq. (1.41) relates $\mathbf{m}_P$ and $\mathbf{h}_P$,

$$\omega_s h_{x,P} = \omega_a m_{x,P} + i \omega_P m_{y,P} \tag{1.60}$$

$$\omega_s h_{y,P} = \omega_a m_{y,P} - i \omega_P m_{x,P}. \tag{1.61}$$

Inserting these into the Hamiltonian ,

$$H = \frac{\mu_0}{2} \sum_{PQ} \left[X_{PQ} \alpha_P \alpha_Q + X_{PQ}^* \alpha_P^* \alpha_Q^* + Y_{PQ} \alpha_P \alpha_Q^* + Y_{PQ}^* \alpha_P^* \alpha_Q \right], \tag{1.62}$$

where

$$X_{PQ} = \frac{i \omega_Q}{\omega_s} \int \left(m_{y,p} m_{x,q} - m_{x,p} m_{y,q} \right) dV \tag{1.63}$$

$$Y_{PQ} = \frac{i \omega_Q}{\omega_s} \int \left(m_{x,p} m_{y,q}^* - m_{y,p} m_{x,q}^* \right) dV. \tag{1.64}$$

Following Ref. [22], we find orthogonality relations between magnons. For $\mathbf{b}_P = \mathbf{h}_P + \mathbf{m}_P$, $\nabla \cdot \mathbf{b}_P = 0$ from Maxwell's equations and

$$\int \psi_Q^* \nabla \cdot \mathbf{b}_P dV = 0, \tag{1.65}$$

where the scalar potential ψ_Q obeys $\nabla^2 \psi_Q = \nabla \cdot \mathbf{m}_Q$. Integrating by parts and using $\mathbf{h}_Q^* = -\nabla \psi_Q^*$,

$$\int (\mathbf{h}_P + \mathbf{m}_P) \cdot \mathbf{h}_Q^* dV = 0. \tag{1.66}$$

Using the same relation with $p \leftrightarrow q$ and subtracting,

$$\int \left(\mathbf{m}_P \cdot \mathbf{h}_Q^* - \mathbf{m}_Q^* \cdot \mathbf{h}_P \right) dV = 0. \tag{1.67}$$

Substituting the mode-dependent fields $\mathbf{h}_{P(Q)}$ from Eqs. (1.60)-(1.61), we find that $(\omega_P - \omega_Q) Y_{PQ} = 0$. A similar calculation starting with $\psi_Q^* \rightarrow \psi_Q$ in Eq. (1.65) gives $(\omega_P + \omega_Q) X_{PQ} = 0$. Assuming no degeneracy, we conclude that $X_{PQ} = 0$ and $Y_{PQ} \propto \delta_{PQ}$. In case of degeneracy, a Gram-Schmidt procedure enforces these orthogonality relations. The Hamiltonian is then reduced to that of a collection of harmonic oscillators:

$$H = \mu_0 \sum_P Y_{PP} \left| \alpha_P \right|^2, \tag{1.68}$$

where we used $Y_{PP} = Y_{PP}^*$.

α_P is proportional to the amplitude of a magnon mode P. Correspondence with the quantum Hamiltonian for harmonic oscillators is achieved with a normalization that associates $|\alpha_P|^2$ to the number of magnons by demanding $\mu_0 Y_{PP} = \hbar \omega_P$ or

$$\int \left(|m_{-,P}|^2 - |m_{+,P}|^2 \right) dV = 2\hbar\gamma M_s. \tag{1.69}$$

For pure (circular) Larmor precession, i.e. $m_+ = 0$, this condition can also be derived by assuming that the magnon has a spin of $\hbar$ since

$$S_z = \int dV \frac{M_s - M_z}{\gamma} = \hbar \sum_P |\alpha_P|^2. \tag{1.70}$$

In contrast, when the precession is elliptic, the spin of a magnon is not $\hbar$ ($m_+ \neq 0$) [32].

1.8. Appendix: Magneto-optical coupling

Here, we derive Eq. 1.12 in terms of phenomenological parameters $\{\epsilon_s, f, g\}$. Linearized magnetization $\mathbf{M}(\mathbf{r}, t) = M_s \boldsymbol{z} + \mathbf{m}(\mathbf{r}, t)$ with $\left|\mathbf{m}(\mathbf{r}, t)\right| \ll M_s$ and $\mathbf{m}.\boldsymbol{z} = 0$. We expand in Taylor series $\overline{\epsilon} = \overline{\epsilon^s} + \overline{\epsilon^d}$, where

$$\overline{\epsilon^s} = \overline{\epsilon}\left[M_s \boldsymbol{z}\right], \quad \overline{\epsilon^d} = \left.\frac{\partial \overline{\epsilon}}{\partial M_x(\mathbf{r}, t)}\right|_{M_s \boldsymbol{z}} m_x(\mathbf{r}, t) + \left.\frac{\partial \overline{\epsilon}}{\partial M_y(\mathbf{r}, t)}\right|_{M_s \boldsymbol{z}} m_y(\mathbf{r}, t). \tag{1.71}$$

Below, we suppress the position and time dependence for brevity. As the Hamiltonian Eq. (1.28) is positive for arbitrary electric field distribution, $\epsilon_{ij}(\mathbf{M}) = \epsilon_{ji}^*(\mathbf{M})$. Further, the form of $\overline{\epsilon}$ is constrained by the symmetries:

- (Rot-θ) rotation by angle θ around $\boldsymbol{z}$-axis
- (Mir) reflection in a mirror perpendicular to $\boldsymbol{z}$-axis

1

For $\mathbf{M} = M_s\mathbf{z}$, (Mir) implies that the equation $\mathbf{D} = \overline{\epsilon^s}\mathbf{E}$ is invariant under $F_{x,y} \to -F_{x,y}$ and $F_z \to F_z$ with $F \in \{E, D\}$. Thus, $\epsilon^s_{xz} = \epsilon^s_{yz} = 0$. (Rot-$\pi/2$) and (Rot-$\pi/4$) implies $\epsilon^s_{xx} = \epsilon^s_{yy}$ and $\epsilon^s_{xy} = -\epsilon^s_{yx}$ respectively. Thus, we can write

$$\overline{\epsilon^s} = \begin{pmatrix} \epsilon_s & -if M_s & 0 \\ if M_s & \epsilon_s & 0 \\ 0 & 0 & \epsilon_s + gM_s^2 \end{pmatrix}, \tag{1.72}$$

where f and g are real.

Invariance of $\mathbf{D} = \overline{\epsilon}(\mathbf{M})\mathbf{E}$ under (Mir) implies $\epsilon_{ij}(M_s\mathbf{z} + M_x\mathbf{x}) = \epsilon_{ij}(M_s\mathbf{z} - M_x\mathbf{x})$ for $i, j \in \{x, y\}$ implying its derivative w.r.t M_x is zero. (Rot-$\pi/2$) implies $\epsilon_{xz}(M_s\mathbf{z} + m\mathbf{x}) = \epsilon_{yz}(M_s\mathbf{z} + m\mathbf{y})$ and $\epsilon_{yz}(M_s\mathbf{z} + m\mathbf{x}) = \epsilon_{xz}(M_s\mathbf{z} - m\mathbf{y})$. These give

$$\left.\frac{\partial\overline{\epsilon}}{\partial M_x}\right|_{M_s\mathbf{z}} = \begin{pmatrix} 0 & 0 & A \\ 0 & 0 & B \\ A^* & B^* & 0 \end{pmatrix}, \quad \left.\frac{\partial\overline{\epsilon}}{\partial M_y}\right|_{M_s\mathbf{z}} = \begin{pmatrix} 0 & 0 & -B \\ 0 & 0 & A \\ -B^* & A^* & 0 \end{pmatrix}, \tag{1.73}$$

where A and B are complex. Experiments suggest a link between the static and the dynamic components for YIG in infrared wavelength: $A = gM_s$ and $B = -if$ [24]. Although a microscopic derivation thereof is lacking, this is useful to compare theory with experiments.

Using the above forms, Eq. (1.71) can be succintly written as Eq. (1.12) up to linear order in $|\mathbf{m}| \ll M_s$.

1.9. Appendix: Interaction with fiber

The interaction of fiber and the sphere is formulated by the input/output (IO) theory [29, 33]. We use the coordinate system defined in Fig. 1.1. We assume that light is entering via a proximity-coupled single mode optical fiber with two degenerate polarizations $\mathbf{E} \parallel \mathbf{z}$ and $\mathbf{E} \parallel \mathbf{y}$ that match the TE and TM cavity modes in the sphere, respectively. The coupling via an optical prism facilitates mode matching and thus, the selection of the incoming and outgoing light modes [18], but the formalism is essentially the same. In the absence of disorder the theory is equivalent for the two polarizations, so we may omit its index here. Our discussion follows the IO theory as formulated for a Febry-Perot cavity [33].

The optical Hamiltonian (including the fiber),

$$\mathcal{H}_0 = \int d\mathbf{r}\left(\frac{\epsilon(\mathbf{r})}{2}\hat{\mathbf{E}}(\mathbf{r})\cdot\hat{\mathbf{E}}(\mathbf{r}) + \frac{1}{2\mu_0}\hat{\mathbf{B}}(\mathbf{r})\cdot\hat{\mathbf{B}}(\mathbf{r})\right) \tag{1.74}$$

In a perturbative treatment of the coupling, we can separate the total electric field as $\hat{\mathbf{E}} = \hat{\mathbf{E}}_f + \hat{\mathbf{E}}_s$ into that in the fiber ($\hat{\mathbf{E}}_f$) and sphere ($\hat{\mathbf{E}}_s$) and analogously $\hat{\mathbf{B}} = \hat{\mathbf{B}}_f + \hat{\mathbf{B}}_s$. The fields inside the sphere can be expanded using Eq. (1.31 and the fiber fields [33],

$$\hat{\mathbf{E}}_f(\mathbf{r}) = \int_{-\infty}^{\infty}\frac{dk}{\sqrt{2\pi}}\left(\mathbf{E}_k(y,z)e^{ikx}\hat{A}(k) + \mathbf{E}^*_k(y,z)e^{-ikx}\hat{A}^\dagger(k)\right), \tag{1.75}$$

where $\mathbf{E}_k(y,z)$ is the transverse spatial distribution and $\hat{A}(k)$ is the annihilation operator of a photon with wave-vector k and commutation rule $[\hat{A}(k), \hat{A}^\dagger(k')] = \delta(k-k')$ [33]. A similar relation holds for $\mathbf{E} \to \mathbf{B}$. Here the fields propagate as plane waves in the x direction, assuming that the fiber has constant (or adiabatically tapered) cross-section near the sphere.

The fields are flux-normalised such that,

$$\int dydz \left[\frac{\mathbf{E}_k \cdot \mathbf{D}_k^*}{2} + \frac{\mathbf{B}_k \cdot \mathbf{H}_k^*}{2}\right] = \frac{\hbar k v_f}{2}, \tag{1.76}$$

where v_f is the speed of light in the fiber. The displacement field $\mathbf{D}_k = \epsilon_f \mathbf{E}_k$ in the fiber and $\mathbf{D}_k = \epsilon_0 \mathbf{E}_k$ outside. The magnetizing field in a non-magnetic medium $\mathbf{H}_k = \mathbf{B}_k/\mu_0$. In the rotating wave approximation, the Hamiltonian becomes

$$\mathcal{H}_0 = \hbar v_f \int dk k\, \hat{A}^\dagger(k)\hat{A}(k) + \sum_P \hbar\omega_P \hat{a}_P^\dagger \hat{a}_P + \sum_P \int \frac{dk}{\sqrt{2\pi}} \hbar \left(g_P^*(k)\hat{a}_P^\dagger \hat{A}(k) + g_P(k)\hat{A}^\dagger(k)\hat{a}_P\right), \tag{1.77}$$

where the coupling is given by the overlap integral

$$\hbar g_P(k) = \int d\mathbf{r}\, e^{-ikx} \left[\frac{\epsilon(\mathbf{r})}{2}\mathbf{E}_k^*(y,z)\cdot\mathbf{E}_P(\mathbf{r}) + \frac{1}{2\mu_0}\mathbf{B}_k^*(y,z)\cdot\mathbf{B}_P(\mathbf{r})\right]. \tag{1.78}$$

g depends on the details of the fiber (for instance, tapering angle). In what follows, we look at the dynamics of a single mode P which is resonant with the input because other modes do not participate.

For a propagating mode with speed of light v_f Heiseberg's equation of motion

$$\frac{d\hat{A}(k,t)}{dt} = -ikv_f\hat{A}(k,t) - \frac{i}{\sqrt{2\pi}} g_P(k)\hat{a}_P(t). \tag{1.79}$$

In position space,

$$\hat{A}(x,t) = \int \frac{dk}{\sqrt{2\pi}} e^{ikx}\hat{A}(k,t). \tag{1.80}$$

Eq. (1.79) is a simple wave equation which gives

$$\hat{A}(x,t) = \hat{A}(x-v_f t) - i\int_0^t \frac{du}{\sqrt{2\pi}} g_P(x-v_f u)\hat{a}_P(t-u). \tag{1.81}$$

where $\hat{A}(x) \equiv \hat{A}(x,0)$ and

$$g_P(x) \triangleq \int e^{ikx} g_P(k) \frac{dk}{\sqrt{2\pi}}. \tag{1.82}$$

The first term in Eq. (1.81) is the unperturbed EM wave. The second term is a memory kernel in which the WGM fields at time $t-u$ instantaneously excite the fiber with spatial dependence $g(x)$. These excited fields then travel at the speed v_f such that the effect at time t is captured by $g(x-v_f u)$.

1

For a sphere of radius R, $\hat{a}_P(t)$ cannot act on the EM fields at the same time and at a distance larger than R (in reality, the contact region is much smaller than R). Therefore, $g(x)$ must be localized within $|x| < R$.

The dynamics of the slow envelope $\hat{W}_P(t) = \hat{a}_P(t)e^{i\omega_P t}$

$$\frac{d\hat{W}_P}{dt} = -ie^{i\omega_P t}\int \frac{dx}{\sqrt{2\pi}} g_P^*(x)\hat{A}(x,t), \tag{1.83}$$

where we used Parseval's identity for Fourier transforms. Using the solution for $\hat{A}$

$$\frac{d\hat{W}_P(t)}{dt} = -\sqrt{K_P}\hat{A}_{\rm in}(t) - i\int_0^t \frac{du}{\sqrt{2\pi}}\Sigma_P(u)\hat{W}_P(t-u) \tag{1.84}$$

where K_P is defined below, the input field

$$\hat{A}_{\rm in}(t) \triangleq i\int \frac{dx}{\sqrt{2\pi}}\frac{g_P^*(x)}{\sqrt{K_P}}\hat{A}(x - v_f t)e^{i\omega_P t} \tag{1.85}$$

is an averaged photon operator, and self-energy

$$\Sigma_P(u) = -i\int \frac{dx}{\sqrt{2\pi}} g_P^*(x)g_P(x - v_f u)e^{i\omega_P u}. \tag{1.86}$$

As discussed before, $g_P(x)$ is zero for $|x| > R$. Therefore, the product $g_P^*(x)g_P(x - v_f u) \approx 0$ for all x if $|u| > 2R/v_f$, implying that $\Sigma_P(u)$ is localised within $|u| < 2R/v_f \sim 10$ ps for $R < 1$ mm. This time is very short compared to the lifetime in high-quality resonators of $\tau_P = 2\pi/\kappa_P \sim 1$ ns. In the short interval $|u| < 2R/v_f$, $\hat{W}_P(t-u) \approx \hat{W}_P(t)$. In other words, we disregard the retardation, i.e. the finite time in which a photon propagates over a distance $2R$, leading to $\Sigma_i(u) \propto \delta(u)$.

The real part of $\Sigma_P(u)$ leads to frequency corrections which are usually negligible compared to optical frequencies and thus, can be ignored or incorporated in the rotating wave. The imaginary part,

$$\frac{K_P}{2} \triangleq \text{Real}\left[\int_0^t \frac{du}{\sqrt{2\pi}} i\Sigma_P\right] \approx \frac{|g_i(k_i)|^2}{v_f}, \tag{1.87}$$

where $k_P \triangleq \omega_P/v_f$ and we used $t \gg 2R/v_f$. Finally, we get

$$\frac{d\hat{W}_P(t)}{dt} = -\sqrt{K_P}\hat{A}_{\rm in}(t) - \frac{K_P}{2}\hat{W}_P(t). \tag{1.88}$$

Eq. (1.88) has been derived in Ref. [29] by assuming $g(k)$ to be approximately constant, $g(k) \approx g(k_P)$. This is equivalent to (1) a $g(x)$ localised within a small distance $|x| < R$, so $g(k)$ does not change significantly over $2\pi/R$ in k-space; and (2) a $g(k)$ centered at the wave-vector matching condition, i.e. $k = k_P$.

The input $\hat{A}_{\rm in}(t)$ depends on the EM fields between $x \approx -R - v_f t$ and $x \approx R - v_f t$. For large $-t$, it encodes the EM fields at $x \to -\infty$ which can be interpreted as the

incoming waves. For a monochromatic input resonant with the WGM, $\hat{A}(x) = \hat{A}e^{ik_P x}$ and the correlation function

$$\left\langle \hat{A}^{\dagger}_{\text{in}}(t)\hat{A}_{\text{in}}(t')\right\rangle = \int \frac{dxdx'}{2\pi}\frac{g_P(x)g_P^*(x')\ e^{ik_P(x'-x)}}{K_P^2}\left\langle \hat{A}^{\dagger}\hat{A}\right\rangle = v_f\left\langle \hat{A}^{\dagger}\hat{A}\right\rangle, \tag{1.89}$$

independent of t, t'. $\left\langle \hat{A}^{\dagger}\hat{A}\right\rangle$ is the light flux in units of number of photons per unit length related to the input power by

$$P_{in} = \hbar\omega_P v_f\left\langle \hat{A}^{\dagger}\hat{A}\right\rangle = \hbar\omega_P\left\langle \hat{A}^{\dagger}_{\text{in}}(t)\hat{A}_{\text{in}}(t')\right\rangle. \tag{1.90}$$

References

[1] https://www2.nve.com/gmrsensors/.

[2] V. V. Kruglyak, S. O. Demokritov, and D. Grundler, *Magnonics,* Journal of Physics D: Applied Physics **43**, 260301 (2010).

[3] A. A. Serga, A. V. Chumak, and B. Hillebrands, *YIG magnonics,* Journal of Physics D: Applied Physics **43**, 264002 (2010).

[4] A. G. Gurevich, *Ferrites at microwave frequencies* (Consultatnts Bureau, 1963).

[5] D. D. Stancil and A. Prabhakar, *Spin Waves: Theory and Applications* (Springer US, 2009).

[6] V. Cherepanov, I. Kolokolov, and V. L'vov, *The saga of yig: Spectra, thermodynamics, interaction and relaxation of magnons in a complex magnet,* Physics Reports **229**, 81 (1993).

[7] M. Wu and A. Hoffmann, *Recent Advances in Magnetic Insulators - From Spintronics to Microwave Applications*, Vol. 64 (Elsevier, 2013) pp. 1–408.

[8] A. V. Chumak, V. I. Vasyuchka, A. A. Serga, and B. Hillebrands, *Magnon spintronics,* Nat Phys **11**, 453 (2015).

[9] L. J. Cornelissen, J. Liu, R. A. Duine, J. B. Youssef, and B. J. van Wees, *Long-distance transport of magnon spin information in a magnetic insulator at room temperature,* Nature Physics **11**, 1022 (2015).

[10] Y. Tabuchi, S. Ishino, T. Ishikawa, R. Yamazaki, K. Usami, and Y. Nakamura, *Hybridizing ferromagnetic magnons and microwave photons in the quantum limit,* Phys. Rev. Lett. **113**, 083603 (2014).

[11] Y. Tabuchi, S. Ishino, A. Noguchi, T. Ishikawa, R. Yamazaki, K. Usami, and Y. Nakamura, *Quantum magnonics: The magnon meets the superconducting qubit,* Comptes Rendus Physique **17**, 729 (2016).

[12] O. O. Soykal and M. E. Flatte, *Strong field interactions between a nanomagnet and a photonic cavity,* Phys. Rev. Lett. **104**, 077202 (2010).

[13] X. Zhang, C.-L. Zou, L. Jiang, and H. X. Tang, *Strongly coupled magnons and cavity microwave photons,* Phys. Rev. Lett. **113**, 156401 (2014).

[14] J. Sandercock and W. Wettling, *Light scattering from thermal acoustic magnons in yttrium iron garnet,* Solid State Communications **13**, 1729 (1973).

[15] T. Sebastian, K. Schultheiss, B. Obry, B. Hillebrands, H. Schultheiss, and B. Obry, *Micro-focused brillouin light scattering: imaging spin waves at the nanoscale,* Frontiers in Physics **3** (2015), 10.3389/fphy.2015.00035.

[16] A. Osada, R. Hisatomi, A. Noguchi, Y. Tabuchi, R. Yamazaki, K. Usami, M. Sadgrove, R. Yalla, M. Nomura, and Y. Nakamura, *Cavity optomagnonics with spin-orbit coupled photons,* Phys. Rev. Lett. **116**, 223601 (2016).

[17] X. Zhang, N. Zhu, C.-L. Zou, and H. X. Tang, *Optomagnonic whispering gallery microresonators,* Phys. Rev. Lett. **117**, 123605 (2016).

[18] J. A. Haigh, A. Nunnenkamp, A. J. Ramsay, and A. J. Ferguson, *Triple-resonant brillouin light scattering in magneto-optical cavities,* Phys. Rev. Lett. **117**, 133602 (2016).

[19] T. Liu, X. Zhang, H. X. Tang, and M. E. Flatté, *Optomagnonics in magnetic solids,* Phys. Rev. B **94**, 060405 (2016).

[20] S. V. Kusminskiy, H. X. Tang, and F. Marquardt, *Coupled spin-light dynamics in cavity optomagnonics,* Phys. Rev. A **94**, 033821 (2016).

[21] S. Sharma, Y. M. Blanter, and G. E. W. Bauer, *Optical cooling of magnons,* Phys. Rev. Lett. **121**, 087205 (2018).

[22] L. R. Walker, *Magnetostatic modes in ferromagnetic resonance,* Phys. Rev. **105**, 390 (1957).

[23] P. C. Fletcher and R. O. Bell, *Ferrimagnetic resonance modes in spheres,* Journal of Applied Physics **30**, 687 (1959), https://doi.org/10.1063/1.1735216 .

[24] W. Wettling, M. G. Cottam, and J. R. Sandercock, *The relation between one-magnon light scattering and the complex magneto-optic effects in yig,* Journal of Physics C: Solid State Physics **8**, 211 (1975).

[25] J. A. Haigh, S. Langenfeld, N. J. Lambert, J. J. Baumberg, A. J. Ramsay, A. Nunnenkamp, and A. J. Ferguson, *Magneto-optical coupling in whispering-gallery-mode resonators,* Phys. Rev. A **92**, 063845 (2015).

[26] G. Rado and J. Weertman, *Spin-wave resonance in a ferromagnetic metal,* Journal of Physics and Chemistry of Solids **11**, 315 (1959).

[27] R. E. D. Wames and T. Wolfram, *Dipole□exchange spin waves in ferromagnetic films,* Journal of Applied Physics **41**, 987 (1970).

[28] K. Y. Guslienko and A. N. Slavin, *Boundary conditions for magnetization in magnetic nanoelements,* Phys. Rev. B **72**, 014463 (2005).

[29] C. W. Gardiner and M. J. Collett, *Input and output in damped quantum systems: Quantum stochastic differential equations and the master equation,* Phys. Rev. A **31**, 3761 (1985).

[30] W. F. Brown, *Thermal fluctuations of a single-domain particle,* Phys. Rev. **130**, 1677 (1963).

[31] L. Landau and E. Lifshitz, *Chapter xii - fluctuations,* in *Statistical Physics*, edited by L. Landau and E. Lifshitz (Butterworth-Heinemann, Oxford, 1980) 3rd ed., pp. 333 – 400.

[32] A. Kamra and W. Belzig, *Super-poissonian shot noise of squeezed-magnon mediated spin transport,* Phys. Rev. Lett. **116**, 146601 (2016).

[33] L. Knöll, W. Vogel, and D.-G. Welsch, *Resonators in quantum optics: A first-principles approach,* Phys. Rev. A **43**, 543 (1991).

2

Brillouin light scattering in whispering gallery mode cavity

Shut up and calculate.

N. David Mermin

This chapter has been published as S. Sharma, Y.M. Blanter, G.E.W. Bauer Phys. Rev. B **96**, 094412 (2017) [1].

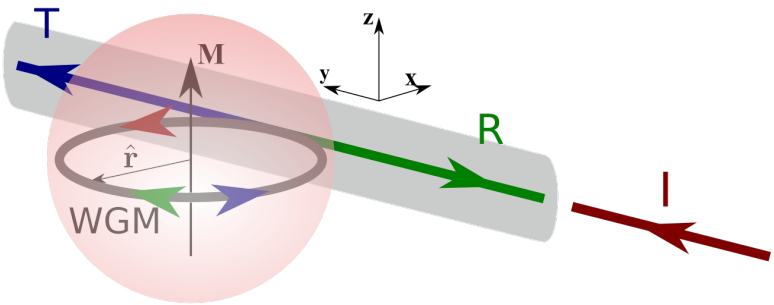

Figure 2.1: A magnetic sphere is coupled to an evanescent coupler which can excite optical modes inside the sphere. Incident photons (I) in the coupler scatter inelastically by the magnetic order in the sphere, which can be observed in the reflected (R) and transmitted (T) light that leads back into the coupler. The corresponding counter-propagating WGMs are shown by green (R) and blue (T) colored arrows inside the sphere.

In this chapter, we study light scattering by magnons in magnetic spheres in which the whispering gallery modes (WGMs) are excited by evanescent coupling to a light source, such as an illuminated waveguide, a tapered fiber or a prism. We generalize previous works by including all the magnons which contribute significantly to BLS. In particular, we differentiate between the transmission and reflection in the coupler attributed to different magnons. We consider magnetic spheres with sub-mm radii as shown in Fig. 2.1. The magnetization is assumed to be saturated by an external magnetic field.

Brillouin light scattering (BLS) in a WGM cavity made from a magnetic material displays a pronounced asymmetry in the Stokes and anti-Stokes light scattering intensities [2–4]. Such an S-aS asymmetry has been observed in other magnetic systems too, e.g. due to an interference of photons affected by different microscopic scattering mechanisms [5, 6]. Another source for S-aS imbalance is an ellipticity of the spin waves that is caused by magnetic anisotropies [7]. This asymmetry is observed in thick films too [8, 9] due to the asymmetric localization of Damon-Eshbach (DE) modes on one of the surfaces [10–13].

We consider the power spectrum of inelastically transmitted and reflected spectra for a given input light source, for both Stokes and anti-Stokes photons, emphasizing the S-aS asymmetry. We present analytic results for specific magnons and provide estimates for the other magnons. We find a pronounced S-aS asymmetry in the transmission, as observed in recent experiments for the Kittel mode [2–4]. Our theory agrees with and generalizes the analysis of [4]. The transmission due to other ("Walker") magnons have been observed as well [14, 15]. We predict that photons are inelastically reflected by DE magnons with complete suppression of either Stokes or anti-Stokes lines. The latter results can be interesting for thermodynamic applications.

This chapter is organized as follows. We start with introducing the observables and qualitative considerations in Sec. 2.1. We calculate the transmitted and the reflected power for a general cavity coupled to an evanescent coupler (a proximity

optical fiber) in Sec. 2.2. We calculate the scattering amplitude of WGMs in Sec. 2.3. We discuss the physical consequences of the theory by considering an example of a YIG sphere with a particular input in Sec. 2.4. We generalize the treatment of Sec. 2.4 to other input modes in Sec. 2.5. We summarize results and give an outlook in Sec. 2.6.

2.1. Initial considerations

We first discuss our setup shown in Fig. 2.1 and a few qualitative aspects to set the stage. An optical coupler guides the incoming and outgoing (near-infrared) light radiation along the $\pm y$-axis. We assume that the waveguide is a thin optical fiber that supports only one transverse optical mode (single mode fiber) with two polarization components corresponding to $\mathbf{E} \parallel \hat{\boldsymbol{z}}$ or $\mathbf{E} \parallel \hat{\mathbf{x}}$, which we label as transverse electric ($\varsigma = \mathrm{TE}$) and transverse magnetic ($\varsigma = \mathrm{TM}$), respectively. The power spectrum of each polarization component is denoted by $P^{\varsigma}_{\mathrm{in}}(\omega)$. The waveguide is optically coupled to the magnetic sphere due to the overlap of the transverse evanescent light amplitudes. We focus on the optical coupling to a single-mode fiber, but application to other geometries such as an attached prism or multi-mode wave guide is straightforward. The output power spectrum addressed here has three components: (1) the transmission without coupling with the magnons, $P^{\varsigma}_{\mathrm{el}}(\omega)$; (2) the light scattered by magnons in the forward direction that can be observed in transmission, $P^{\varsigma}_{\mathrm{T}}(\omega)$; (3) the light reflected by magnons, $P^{\varsigma}_{\mathrm{R}}(\omega)$.

The incident photons predominantly excite the WGMs of the sphere, which are optical modes confined to the equatorial surface and thus have the largest overlap with the optical waveguide modes. The WGMs of large spheres are to a good approximation linearly TM or TE polarized plane EM waves that propagate adiabatically along the equator. The coupling to the optical waveguide is assumed to conserve the polarization, which is a good approximation for clean contacts.

The excited WGMs may be scattered by magnons into a multitude of other optical modes mediated by the optomagnonic interaction, to be discussed in detail below. We only consider scattering among the WGMs, because only those couple to the optical waveguide and lead to observable effects. We take the magnetization to be along $+z$-axis (and later also consider the case of $-z$). In this configuration, elastic scattering effects mediated by the magnetization are symmetry-forbidden [5, 6], which simplifies the analysis. We treat the optomagnonic interaction by perturbation theory, which is valid if the magnons are not significantly affected by light. The frequency of optical photons is several orders of magnitude larger than that of magnons, so the incident and the scattered light has almost the same frequency. This implies that the scattering between the WGMs to a good approximation preserves the modulus of the (azimuthal) momentum, while a reversal of the direction (reflection or backscattering) is allowed [16]. The forward and backward scattered light are indicated by the blue and green arrows in Fig. 2.1, respectively. The scattered WGMs leak back into the optical waveguide, propagating towards $+y$ or $-y$ depending on the circulation sense of WGMs [as shown by the color-matched arrows in Fig. 2.1].

Since forward scattering nearly conserves photon momentum, the involved magnons

must have small angular momentum, denoted here as small-L (SL) magnons. The most important SL magnon is the uniformly precessing magnetization (macrospin or Kittel) mode with zero orbital angular momentum. In contrast, the reflection of photons is caused by magnons whose angular momentum is approximately twice of that of the incident WGM. High angular momentum transfer can be provided by the Damon-Eshbach (DE) surface modes localized to the equator of the sphere [10]. These magnons are chiral, viz. they always circulate in an anti-clockwise fashion with respect to the magnetization (parallel to the blue arrow in Fig. 2.1). We denote the set of DE magnons as large-L (LL) magnons.

Before going into the details of the scattering mechanism inside the sphere, we discuss the photon transport in the single-mode optical fiber evanescently coupled to the sphere. The equations can be easily carried over to discuss coupling via a prism attached to the sphere [4].

2.2. Output spectrum

Here we derive the power spectrum of transmitted and reflected photons for a given source by the input-output (IO) formalism [17, 18] . Consider an incident light beam with polarization dependent amplitude $\hat{A}^{\varsigma}_{\text{in}}(t)$, where $\varsigma \in \{\text{TE}, \text{TM}\}$. $\hat{A}^{\varsigma}_{\text{in}}$ is the annihilation operator of the incoming traveling photons that satisfy the commutation rules $\left[\hat{A}^{\varsigma}_{\text{in}}(t'), \hat{A}^{\varsigma'\dagger}_{\text{in}}(t)\right] = \delta_{\varsigma,\varsigma'}\delta(t-t')$. The overlap of the fiber and WGM modes generates photons in the sphere. The latter are expressed by the annihilation operators $\{\hat{a}_P\}$ for a mode P (discussed for WGMs in Sec 1.4). The Hamiltonian $\hat{H}$ for the sphere as derived in Section 1.5.1 leads to the equation of motion

$$\frac{d\hat{a}_P}{dt} = \frac{i}{\hbar}\left[\hat{H}, \hat{a}_P\right] - \frac{\bar{\kappa}_P}{2}\hat{a}_P - \sum_{\varsigma}\left(\frac{\kappa^{\varsigma}_P}{2}\hat{a}_P + \sqrt{\kappa^{\varsigma}_P}\hat{A}^{\varsigma}_{\text{in}}\right), \tag{2.1}$$

where $\bar{\kappa}_P$ is the intrinsic dissipation rate of mode P in the sphere. κ^{ς}_P parameterizes the coupling between the fiber and the WGMs [17, 18] via the term $\sqrt{2\kappa^{\varsigma}_P}\hat{A}^{\varsigma}_{\text{in}}$ as well as the dissipation by the escape of ς-polarized WGM photons into the fiber.

The IO formalism relates the input and output amplitudes as

$$\hat{A}^{\varsigma}_{\text{out}} = \hat{A}^{\varsigma}_{\text{in}} + \sum_{P}\sqrt{\kappa^{\varsigma}_P}\hat{a}_P, \tag{2.2}$$

where $\hat{A}^{\varsigma}_{\text{out}}$ includes both transmitted and reflected photons. As discussed above, we can separate the transmitted and reflected components based on the circulation sense of WGMs which is coded in the mode index P [see Fig. 2.1]. $\hat{A}^{\varsigma}_{\text{out}}$ governs the light observables in the fiber after interaction with the sphere. Eqs. (2.1) and (2.2) leads to $\hat{A}^{\varsigma}_{\text{out}}$ in terms of $\hat{A}^{\varsigma}_{\text{in}}$.

We now relate the amplitudes $\hat{A}^{\varsigma}_{\text{in}}$ and $\hat{A}^{\varsigma'}_{\text{out}}$ to the corresponding power spectra $P^{\varsigma}_{\text{in}}(\omega)$ and $P^{\varsigma'}_{\text{out}}(\omega)$ respectively. The power spectrum P corresponding to a field

operator $\hat{A}$ can be expressed as [18]

$$\hbar\omega \left\langle \hat{A}^{\dagger}(\omega_1)\hat{A}(\omega)\right\rangle = 2\pi P(\omega)\delta(\omega+\omega_1), \tag{2.3}$$

where the Fourier transform is defined as

$$\hat{f}(\omega) \triangleq \int dt\; e^{i\omega t}\hat{f}(t). \tag{2.4}$$

By replacing $\hat{A} \to \hat{A}^{\varsigma}_{\text{in}}, \hat{A}^{\varsigma}_{\text{out}}$ and $P \to P^{\varsigma}_{\text{in}}, P^{\varsigma}_{\text{out}}$ respectively, we can define the input and output power spectra. We find P_{out} in terms of P_{in} via the amplitude $\hat{A}^{\varsigma}_{\text{out}}$ in terms of $\hat{A}^{\varsigma}_{\text{in}}$.

2.2.1. Output amplitude

We first discuss the frequency dependence of the operators from which the power spectra can be obtained using Eq. (2.3). We treat the magnetism in terms of non-interacting spin waves or magnons, which is valid in the limit of small density and/or long wavelength of magnons. The Hamiltonian for the sphere (derived in Section 1.5.1) can be written as,

$$\hat{H} = \sum_{P} \hbar\omega_P \hat{a}_P^{\dagger}\hat{a}_P + \sum_{A} \hbar\omega_A \hat{c}_A^{\dagger}\hat{c}_A + \hat{H}_{\text{OM}}, \tag{2.5}$$

where the $\hat{c}_A$ are annihilation operators of magnon in the sphere with mode index A, $\omega_P(\omega_A)$ are the photon (magnon) frequencies, and $\hat{H}_{\text{OM}}$ represents the opto-magnonic interaction.

Since the optomagnonic interaction is weak, we can expand $\hat{H}_{\text{OM}}$ to leading order in the possible scattering processes. The photonic and magnonic modes have typical frequencies $\omega_P \sim 100-1000$ THz and $\omega_A \sim 1-10$ GHz, respectively. Optical absorption $\sim \hat{a}_P^{\dagger}\hat{c}_A$ and two-photon generation $\sim \hat{a}_P^{\dagger}\hat{a}_Q^{\dagger}\hat{c}_A$ can be safely disregarded since $\omega_A \ll \omega_P$. The leading interaction terms are of the light-scattering form

$$\hat{H}_{\text{OM}} = \hbar \sum_{PQA} \hat{a}_P\hat{a}_Q^{\dagger}\left(G^{+}_{PQA}\hat{c}_A + G^{-}_{PQA}\hat{c}_A^{\dagger}\right). \tag{2.6}$$

G^{+}_{PQA} parameterizes, e.g., the amplitude for the scattering of a WGM from mode P into Q by annihilating an A-magnon. We derive expressions for these matrix elements in the sections below for spherical samples.

Inserting Eq. (2.6) into Eq. (2.1) leads to the coupled operator equation,

$$\hat{a}_Q(\omega) = -\chi_Q(\omega)\left\{\sum_{\varsigma}\sqrt{\kappa^{\varsigma}_Q}\hat{A}^{\varsigma}_{\text{in}}(\omega) + \sum_{PA}\left[\hat{a}_P * \left(G^{+}_{PQA}\hat{c}_A + G^{-}_{PQA}\hat{c}_A^{\dagger}\right)\right](\omega)\right\}, \tag{2.7}$$

where

$$\chi_Q(\omega) = \frac{1}{-i(\omega-\omega_Q) + (\bar{\kappa}_Q + \kappa_Q^{\text{TE}} + \kappa_Q^{\text{TM}})/2}, \tag{2.8}$$

is the susceptibility of the Q-WGM, and $*$ denotes convolution in the frequency domain,

$$\left[\hat{f} * \hat{g}\right](\omega) \triangleq \int \frac{d\omega'}{2\pi} \hat{f}(\omega')\, \hat{g}(\omega - \omega'). \tag{2.9}$$

To leading order in $G^{\pm}$, we may linearise the equation $\hat{a}_P \to -\sum_\varsigma \chi_P \sqrt{\kappa_P^\varsigma}\hat{A}_{\rm in}^\varsigma$ on the right-hand-side of Eq. (2.7). Its solution for $\hat{a}_Q$ can be inserted into Eq. (2.2) leading to the output amplitude

$$\hat{A}_{\rm out}^{\varsigma'}(\omega) = \hat{A}_{\rm el}^{\varsigma'}(\omega) + \hat{A}_{\rm T}^{\varsigma'}(\omega) + \hat{A}_{\rm R}^{\varsigma'}(\omega). \tag{2.10}$$

The contribution, $\hat{A}_{\rm el}^{\varsigma'}$ describes the purely dielectric and elastic response, i.e. the transmission without optomagnonic coupling, $G^{\pm} = 0$

$$\hat{A}_{\rm el}^{\varsigma'}(\omega) = \hat{A}_{\rm in}^{\varsigma'}(\omega) - \sum_{Q,\varsigma} \chi_Q(\omega) \sqrt{\kappa_Q^{\varsigma'}\kappa_Q^{\varsigma}}\ \hat{A}_{\rm in}^{\varsigma}(\omega). \tag{2.11}$$

The photons forward or backward scattered by the magnons are given by $\hat{A}_{\rm T}$ and $\hat{A}_{\rm R}$ respectively, where

$$\hat{A}_{\rm T}^{\varsigma'}(\omega') = \sum_{\substack{PQ,\varsigma \\ A\in{\rm SL}}} \int \frac{d\omega}{\pi} \sqrt{\kappa_Q^{\varsigma'}\kappa_P^{\varsigma}}\chi_Q(\omega')\chi_P(\omega)\hat{A}_{\rm in}^{\varsigma}(\omega)$$
$$\left[G_{PQA}^{+}\hat{c}_A(\omega' - \omega) + G_{PQA}^{-}\hat{c}_A^{\dagger}(\omega' - \omega)\right], \tag{2.12}$$

and a similar equation is given by the replacements $\hat{A}_{\rm T} \to \hat{A}_{\rm R}$ and SL $\to$ LL, where SL and LL are the set of small-L and large-L magnons, as explained above.

We can interpret Eq. (2.12) in terms of the following scattering processes

$$\hat{A}_{\rm in}^{\varsigma}(\omega) \to \hat{a}_P \xrightarrow{\hat{c}_A\in{\rm SL}} \hat{a}_Q \to \hat{A}_{\rm T}^{\varsigma'}(\omega'). \tag{2.13}$$

The incoming photons with polarization ς at frequency ω couple to the P-WGMs with rate $\propto \sqrt{\kappa_P^\varsigma}\chi_P(\omega)$. Each of the P -modes is scattered by a small-L A -magnon to a Q-WGM with rate $\propto G_{PQA}^{\pm}$. The scattered Q-WGMs are transferred back into the fiber with polarization ς' and frequency ω' at rates $\propto \sqrt{\kappa_Q^{\varsigma'}}\chi_Q(\omega')$. Summing over all PQA gives the output as a function of input frequency and polarization. A similar equation involving large-L magnons gives the reflected amplitude.

2.2.2. Output power

Eq. (2.10) can be used to derive the output power spectrum $P_{\rm out}$ in terms of the expectation value in Eq. (2.3) involving squared $\hat{A}_{\rm out}$. We assume that the TE and

TM polarized components of input light are uncorrelated,

$$\left\langle \left(\hat{A}_{\text{in}}^{\varsigma'}\right)^{\dagger}(\omega_1)\hat{A}_{\text{in}}^{\varsigma}(\omega)\right\rangle = 0,\ \varsigma \neq \varsigma'. \tag{2.14}$$

This is valid if the input is TE or TM polarized. The auto-correlation function of $\hat{A}_{\text{in}}^{\varsigma}$ defines the input power according to Eq. (2.3). Since magnons are only weakly perturbed by the light, so we have $\left\langle \hat{c}_A^{\dagger}\hat{A}_{\text{in}}\right\rangle = \left\langle \hat{c}_A\hat{A}_{\text{in}}\right\rangle = 0$. Therefore the elastically scattered light $\hat{A}_{\text{el}}$ does not interfere with $\hat{A}_{\text{T}}$ and $\hat{A}_{\text{R}}$, i.e.

$$\left\langle \hat{A}_{\text{el}}\hat{A}_{\text{T}}\right\rangle = \left\langle \hat{A}_{\text{el}}\hat{A}_{\text{R}}\right\rangle = 0. \tag{2.15}$$

In contrast to the photons, the magnons are at ambient temperatures thermally occupied even without external stimulation. Thermal equilibrium of magnons can be modeled by the interactions with a memory-less (Markovian) bath at temperature T [18] that consists of a quasi-continuum of bosonic oscillators $\{\hat{B}_{\boldsymbol{\Omega}}\}$, where Ω is the frequency of an oscillator in mode $\boldsymbol{\Omega}$ and annihilation operator $\hat{B}_{\boldsymbol{\Omega}}$ with $\left[\hat{B}_{\boldsymbol{\Omega}}, \hat{B}_{\boldsymbol{\Omega}'}^{\dagger}\right] = \delta_{\boldsymbol{\Omega}\boldsymbol{\Omega}'}$. The equation of motion of an A-magnon can then be written as

$$\frac{d\hat{c}_A(t)}{dt} = -i\omega_A\hat{c}_A(t) - \frac{\bar{\kappa}_A}{2}\hat{c}_A(t) - \sqrt{\bar{\kappa}_A}\hat{b}_A(t), \tag{2.16}$$

where $\bar{\kappa}_A$ is the intrinsic linewidth that in the model below reads $\bar{\kappa}_A = \alpha_G\omega_A$ in terms of the Gilbert damping α_G. $\hat{b}_A$ represents a fluctuating noise source acting on the A-magnon and generated by the bath. It is given approximately by [18],

$$\hat{b}_A(t) \approx \frac{1}{\sqrt{2\pi\rho(\omega_A)}} \sum_{\substack{\boldsymbol{\Omega} \\ |\Omega-\omega_A|<\bar{\kappa}_p}} \hat{B}_{\boldsymbol{\Omega}}(t_0)e^{-i\Omega(t-t_0)}, \tag{2.17}$$

where $t_0 \to -\infty$ is some initial time, $\rho(\omega_A)$ is the density of states of the bath at frequency ω_A [see [19] for a proper mathematical treatment]. The bath operators with $\left\langle \hat{b}_A(t)\right\rangle = 0$ are assumed to obey the commutation rules

$$\left[\hat{b}_A(t'), \hat{b}_B^{\dagger}(t)\right] = \delta_{AB}\delta(t-t'). \tag{2.18}$$

At equilibrium

$$\left\langle \hat{b}_A^{\dagger}(t')\hat{b}_B(t)\right\rangle = \delta_{AB}n_A\delta(t-t'), \tag{2.19}$$

where $n_A = \left(\exp\frac{\hbar\omega_A}{k_BT} - 1\right)^{-1}$ is the Bose-Einstein distribution at temperature T and zero chemical potential. These equations lead to the magnon correlation function

$$\left\langle \hat{c}_A^{\dagger}(\omega_1)\hat{c}_B(\omega_2)\right\rangle = 4\pi\delta(\omega_1+\omega_2)\delta_{AB}n_A\text{Re}\left[\chi_A(\omega_2)\right], \tag{2.20}$$

where the susceptibility $\chi_A(\omega) = [-i(\omega-\omega_A)+\bar{\kappa}_A/2]^{-1}$ is defined analogous to Eq. (2.8), and Re$[*]$ denotes the real part of the argument. Similarly,

$$\left\langle \hat{c}_B(\omega_1)\hat{c}_A^\dagger(\omega_2)\right\rangle = \frac{n_A+1}{n_A}\left\langle \hat{c}_A^\dagger(\omega_2)\hat{c}_B(\omega_1)\right\rangle. \tag{2.21}$$

$\left\langle \hat{c}_A^\dagger(\omega_1)\hat{c}_B(\omega_2)+\hat{c}_B^\dagger(-\omega_2)\hat{c}_A(-\omega_1)\right\rangle$ is consistent with the fluctuation dissipation theorem [20].

Since transmission and reflection involves different magnons, $\hat{A}_\mathrm{T}$ and $\hat{A}_\mathrm{R}$ are uncorrelated. The output power [see Eqs. (2.3) and (2.10)] can therefore be written as the sum $P_\mathrm{out} = P_\mathrm{el}+P_\mathrm{T}+P_\mathrm{R}$. The purely dielectric/plasmonic contribution

$$P_\mathrm{el}^{\varsigma'}(\omega) = \sum_\varsigma \left|\delta_{\varsigma\varsigma'} - \sum_Q \chi_Q(\omega)\sqrt{\kappa_Q^{\varsigma'}\kappa_Q^\varsigma}\right|^2 P_\mathrm{in}^\varsigma(\omega), \tag{2.22}$$

persists when $G^\pm \to 0$. The magnonic contribution to the transmitted spectrum is

$$P_\mathrm{T}^{\varsigma'}(\omega') = \sum_{\varsigma,\, A\in\mathrm{SL}} \int \frac{d\omega}{2\pi} P_\mathrm{in}^\varsigma(\omega)\left[\frac{\bar{\kappa}_A S_A^+ n_A}{\Delta_+^2+\bar{\kappa}_A^2/4} + \frac{\bar{\kappa}_A S_A^-(n_A+1)}{\Delta_-^2+\bar{\kappa}_A^2/4}\right], \tag{2.23}$$

where

$$S_A^\pm = \left|\sum_{PQ} G_{PQA}^\pm \sqrt{\kappa_P^\varsigma \kappa_Q^{\varsigma'}}\,\chi_P(\omega)\chi_Q(\omega')\right|^2, \tag{2.24}$$

and $\Delta_\pm = \omega' - \omega \mp \omega_A$ is the detuning from the resonance condition. Eq. (2.23) holds also after replacing $P_\mathrm{T} \to P_\mathrm{R}$ and SL $\to$ LL. These results are general under weak coupling of any magnet to an evanescent single-mode coupler and large detuning of magnon and photon frequencies. In order to arrive at results that can be compared with experiments, we have to model $G^\pm$, which is done in the following.

While we focus here on thermally excited magnons, the formalism so far and below can be adapted to other magnon distributions. For instance, the coherent excitation by microwaves with frequency ω_MW can be handled by substituting in Eq. (2.20)

$$n_A \mathrm{Re}\left[\chi_A(\omega_2)\right] \to n_A \mathrm{Re}\left[\chi_A(\omega_2)\right] + \pi\left|\beta_A\right|^2 \delta(\omega_2-\omega_\mathrm{MW}), \tag{2.25}$$

where $\beta_A = \langle \hat{c}_A\rangle$ depends on the microwave power. The scattering power Eq. (2.23) is then augmented by

$$\begin{aligned} P_\mathrm{MW}^{\varsigma'}(\omega') = \sum_{\varsigma A}\Big[&\left|\beta_A\right|^2 \left(P_\mathrm{in}^\varsigma(\omega)S_A^+\right)_{\omega=\omega'-\omega_\mathrm{MW}} \\ &+ \left(\left|\beta_A\right|^2+1\right)\left(P_\mathrm{in}^\varsigma(\omega)S_A^-\right)_{\omega=\omega'+\omega_\mathrm{MW}}\Big]. \end{aligned} \tag{2.26}$$

2.3. BLS Amplitude

Here we calculate the coupling between the WGMs and magnons as expressed by Eq. (1.33) by perturbation theory. Using Eq. (1.34) $G^{\pm}_{\sigma=\sigma'} = 0$. In other words, $\mathrm{TE} \to \mathrm{TE}$ and $\mathrm{TM} \to \mathrm{TM}$ scattering probability vanishes, implying that the incident and the scattered photons have orthogonal polarizations. For $P \equiv \{\nu, l, m, \mathrm{TE}\}$, $Q \equiv \{\nu', l', m', \mathrm{TM}\}$, and $A \equiv \{\nu_s, l_s, m_s\}$. We have four possible incident WGMs, with $\sigma \in \{\mathrm{TE}, \mathrm{TM}\}$ and $m \approx \pm l$. In the following we explicitly illustrate the concepts for the particular case of TE polarized incident WGM with $m > 0$ (rotation sense of blue arrow in Fig. 2.1). Subsequently, we give the results for $m < 0$, while the case of TM polarized input follow from Hermiticity, $G^{\pm}_{QPA} = \left(G^{\mp}_{PQA}\right)^*$.

2.3.1. Small-L

For $m > 0$, the integral, Eq. (1.34), can be simplified for the Kittel mode (see Appendix 2.7.1),

$$G^{\pm}_{PQK} = g_{\pm}\delta_{\nu,\nu'}\delta_{m',m\pm1}\delta_{l-m,l'-m'}, \tag{2.27}$$

where

$$g_{\pm} = \frac{c\left(\Psi^{(2)}_{LB} \pm \Psi_{CB}\right)}{2n_s\sqrt{sV}}, \tag{2.28}$$

with $s = M_s/(\gamma\hbar)$ the spin (number) density and V the volume of the sphere.

The orthogonality of WGMs and constant amplitude of the Kittel mode leads to the selection rule $\nu = \nu'$. The z-component of the total angular momentum is conserved when $m' = m \pm 1$, where the upper(lower) sign corresponds to annihilation(creation) of a magnon. The third selection rule, $l' - m' = l - m$ can be interpreted as the conservation of the non-z component of angular momentum since $l - m \propto l^2 - m^2 \propto L^2 - L_z^2$. This condition is not exact when rotational symmetry is broken by the magnetization, but a good approximation here by the smallness of the MO coupling.

We can extend the discussion to small but finite-L magnons. The coupling constant for Stokes scattering is

$$\begin{aligned} G^{-}_{PQA} &\propto \delta_{\nu,\nu'} \int \left(Y^{m_s}_{l_s}\right)^* Y^{m}_{l} \left(Y^{m'}_{l'}\right)^* d\mathbf{\Omega} \\ &\propto \delta_{\nu,\nu'} \langle l', 0; l_s, 0 |\, l, 0\rangle \langle l', m'; l_s, m_s |\, l, m\rangle, \end{aligned} \tag{2.29}$$

where $d\mathbf{\Omega} = \sin\theta d\theta d\phi$. The Clebsch-Gordon (CG) coefficient $\langle l_1, m_1; l_2, m_2 |\, l_3, m_3\rangle$ is the amplitude of two angular momentum states $\{l_1, m_1\}$ and $\{l_2, m_2\}$ adding up to a third $\{l_3, m_3\}$, with explicit expressions in for instance [21] . If we interpret l_s as the angular momentum of a magnon, the first and second CG coefficients express conservation of L and L_z respectively. The coupling strengths depend on the transverse magnetization of the corresponding magnon at the equatorial surface that is of the same order as the Kittel mode, leading to the estimate,

$$G^{-}_{PQA} \sim g_{-}\delta_{\nu,\nu'} \langle l', 0; l_s, 0 |\, l, 0\rangle \langle l', m'; l_s, m_s |\, l, m\rangle. \tag{2.30}$$

Analogously, the anti-Stokes scattering is governed by

$$G^{+}_{PQA} \sim g_{+}\delta_{\nu,\nu'} \langle l,0;l_s,0|\ l',0\rangle \langle l,m;l_s,m_s|\ l',m'\rangle . \tag{2.31}$$

When $m<0$ (rotation sense of green arrow in Fig. 2.1), a similar calculation shows that the above results are valid for negative m,m' as well.

2.3.2. Large-L

While small angular momentum-magnons scatter light into the forward direction, light can be backscattered by magnons with angular momenta twice of that of the photon. We focus on the chiral DE magnons that encircle the equatorial surface with mode numbers $l_s=m_s\gg 1$. The conservation of L_z gives $m'=m\mp l_s$ where the upper(lower) sign refers to creation(annihilation) of a magnon. As discussed in Sec. 2.1, $m\approx -m'$ by energy conservation, and therefore the only allowed transition is with $m'=m-l_s$ with $l_s\approx 2m$. In other words, in the present configuration a WGM can be scattered backward only by creating a magnon, but not by annihilating one. In Appendix (2.7.2), we derive for $m>0$ and $m'<0$,

$$G^{-}_{PQD} \approx \Xi_{-} g_{-} \langle l,0;l',0|\ l_s,0\rangle \langle l,m;l',|m'||\ l_s,l_s\rangle , \tag{2.32}$$

and $G^{+}_{PQD}=0$, where g_{-} is given by Eq. (2.28). The pre-factor

$$\Xi_{-} = (-1)^{\nu-\nu'+m'}\sqrt{\frac{4}{3}\pi}P_{TE}\,(1+P_{TM}) . \tag{2.33}$$

is of order $|\Xi_{-}|\sim 1$. There is no selection rule for the radial mode indices. The CG coefficients imply that the scattering is non-zero only when $m=l_s+m'$ as argued above. The scattering amplitude is maximized when the angular momentum is conserved $l+l'\approx l_s$.

A similar calculation for a WGM with opposite circulation $m<0$ and $m'>0$, gives $G^{-}_{PQD}=0$

$$G^{+}_{PQD} \approx \Xi_{+} g_{+} \langle l,0;l',0|\ l_s,0\rangle \langle l,|m|;l',m'|l_s,l_s\rangle , \tag{2.34}$$

with

$$\Xi_{+} = (-1)^{\nu-\nu'+m'}\sqrt{\frac{4}{3}\pi}P_{TE}\,(1-P_{TM}) . \tag{2.35}$$

The above coupling constants are dependent on the overlap of DE magnons and WGMs as given in Eqs. (2.60) and (2.64). The angular overlap gives the angular momentum conservation laws selecting the DE magnon based on P and Q. For given WGMs and DE magnons, the radial overlap is small owing to two factors. First, WGMs have a node close to the surface at which the DE magnon amplitude is largest. Secondly, the spatial distributions of WGMs are wider ($\sim a/l^{2/3}$) than those of the DE modes ($\sim a/l_s$). By engineering the spatial distribution of WGMs, the overlap can possibly be enhanced, as will be discussed in a forthcoming article.

2.4. Transmission and reflection spectra

With the expressions for $G^{\pm}$ in hand, we can calculate the transmitted and the reflected spectrum given any input spectrum, P_{T} and P_{R} in terms of P_{in} [see Eq. (2.23)]. In principle, the output power spectrum can be numerically evaluated from the expressions derived above. Analytical expressions for the general case are complicated and difficult to interpret. Leaving this task for future work, we focus here on a special case to illustrate our results. The notation has been defined in Sec. 2.2.

2.4.1. Setup

Coupling: The evanescent coupling of a magnetic sphere can be achieved by proximity to an optical fiber or prism that is illuminated by photons with tunable frequency ω, wave-vector k, and polarization ς. We assume dominantly adiabatic coupling in which only WGMs with matching polarizations ($\sigma = \varsigma$) and wave vectors ($m \approx ka$) are populated. Under these conditions, the leakage from and to the fiber into a mode $W \equiv \{\nu, l, m, \sigma\}$ is $\kappa_W^{\varsigma} = \delta_{\varsigma,\sigma}\kappa_W$, where κ_W is a constant depending on the precise system parameters.

The resonance condition holds for large $l \lessapprox \omega n_s a/c$, with precise value of l discussed below. For a single mode fiber with a contact point to the sphere much smaller than the wavelength, the wave-vector matching holds only approximately and WGMs with many m-values can be excited. However, the coupling can be engineered by tapering the fiber to a width below the wavelength as discussed in [22]. This additional degree of freedom allows to match modes and selectively enhance the coupling to WGMs with small $l - |m|$ and ν. Here we consider the case where κ_W is significant only for $\nu \in \{1, 2\}$ and is maximal at $m = l$ (for a given $\{\nu, l, \sigma\}$). These assumptions can be verified in a particular experiment by monitoring the elastic transmission power P_{el} in Eq. (2.22) [23].

Sphere: Consider a YIG sphere of radius $a = 200\,\mu$m. At room temperature $M_s = 1.4 \times 10^5$ A/m and $n_s = 2.2$. The incident light has wavelength $\lambda_0 \approx 1\,\mu\mathrm{m}$ and is tunable. Near this wavelength, the MO constants are $\Psi_{CB} \sim 500$ rad/m and $\Psi_{LB}^{(1)} = \Psi_{LB}^{(2)} \sim 200$ rad/m [24], which leads to $g_+ = 2\pi \times 6$ Hz and $g_- = -2\pi \times 2.6$ Hz [see Eq. (2.28)]. The latter numbers agree with the estimate $g = 2\pi \times 5$ Hz from [3], where it is not clearly specified whether g is g_+ or g_-.

A magnetic field B_0 shifts the magnon frequencies rigidly by the Zeeman energy. In thermal equilibrium at room temperature with $\omega_A \sim 1{-}10$ GHz, we have $\hbar\omega_A n_A \approx k_B T$ and $n_A \gg 1$. When the sample is excited by resonant microwaves, the Kittel mode is selectively populated and n_K can become much larger than the thermal population. $\bar{\kappa}_A \sim \alpha_G \omega_A$, where $\alpha_G = 10^{-4}$ is typical for Gilbert damping in YIG [25].

WGM spectrum: The frequencies from Eq. (1.27) are sketched in Fig. 2.2. They depend on l, ν, and σ (but not on m). For fixed l and ν, the frequencies for two polarizations differ by $\Delta\omega_{\mathrm{BF}}$,

$$\Delta\omega_{\mathrm{BF}} = \frac{c}{n_{\mathrm{s}} a}\left(\frac{\sqrt{n_{\mathrm{s}}^2 - 1}}{n_{\mathrm{s}}} + a\Psi_{LB}^{(1)}(\lambda_0)\right). \tag{2.36}$$

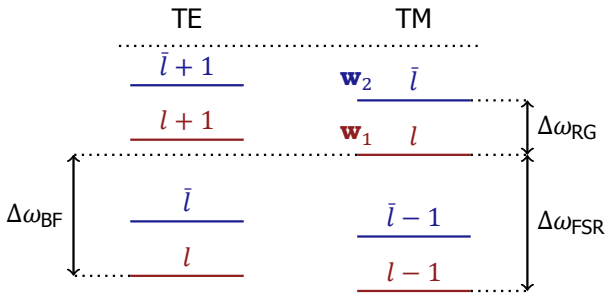

Figure 2.2: Spectrum of WGMs: The resonant frequency of a WGM depends on the angular momentum (l_R), the number of radial nodes ($\nu-1$), and the polarization. This sketch includes the levels for the first two radial modes $\nu=1$ and $\nu=2$ denoted by red and blue respectively. The labels for the splittings (FSR, BF, and RG) are defined in the text.

The gap between l and $l+1$ is called "free spectral range (FSR)". For a fixed σ and ν, $\Delta\omega_{\mathrm{FSR}} \approx c/(n_s a)$ [see Eq. (1.27)]. Two ladders of WGMs with $\nu=1$ and $\nu=2$ are shown by red and blue in Fig. 2.2, respectively (we consider only two ν values as discussed before). The splitting between levels with different ν but same l is large $\sim 4\mathrm{THz}$, but levels can be close for different angular momenta. For a given l, we define $\bar{l}$ as the WGM in the $\nu=2$ branch with frequency just above the $\{\nu=1,l\}$ WGM. So $\bar{l}$ is the lowest integer such that $\omega_{W_2} > \omega_{W_1}$ where W_i are defined in Fig. 2.2. For large $l,\bar{l}$

$$\omega_{W2} > \omega_{W1} \Rightarrow \bar{l} > l - \frac{\beta_2-\beta_1}{2^{1/3}} l^{1/3}, \tag{2.37}$$

where $(\beta_2-\beta_1)/2^{1/3} \approx 1.4$. This gives $\bar{l} = \lceil l - 1.4 l^{1/3} \rceil$ where the ceiling function $\lceil x \rceil$ is the smallest integer greater than x. We define the "radial gap" $\Delta\omega_{\mathrm{RG}} = \omega_{W2} - \omega_{W1}$ that depends on the fractional part of $l - 1.4 l^{1/3}$. The scattering between modes with different ν can be relevant in reflection, as discussed below.

We can estimate the characteristic frequency splittings in Fig. 2.2 for our model system as follows. We tune the input laser frequency ω_{in} to the mode $\{\nu=1, l_p = 1257, l_p, \mathrm{TE}\}$ (at a wavelength around $1\,\mu$m). We find $\bar{l}_p = 1242$ and $\Delta\omega_{\mathrm{RG}} = 2\pi\times 16$ GHz. This is much smaller than the free spectral range $\Delta\omega_{\mathrm{FSR}} = 2\pi \times 108$ GHz and birefringence $\Delta\omega_{\mathrm{BF}} = 2\pi \times 101$ GHz.

Source: Let us assume TE polarized input light (TM is discussed below) at frequency ω_{in} (defined above). Its power spectrum is

$$P_{\mathrm{in}}^{\varsigma}(\omega) = 2\pi\delta_{\mathrm{TE},\varsigma}\bar{P}_{\mathrm{in}}\delta(\omega-\omega_{\mathrm{in}}), \tag{2.38}$$

where $\bar{P}_{\mathrm{in}}$ is the total integrated power in the input

$$\bar{P}_{\mathrm{in}} = \int \frac{d\omega}{2\pi} P_{\mathrm{in}}^{\mathrm{TE}}(\omega). \tag{2.39}$$

In the following we focus on WGMs with index $P \equiv \{1, l_p, m, \mathrm{TE}\}$ that are resonant with ω_{in}. This is allowed when the broadening of other WGMs is much smaller

than their detuning from the input, i.e. $|\omega_W - \omega_{\rm in}| \gg \bar{\kappa}_W$ for $\omega_W \neq \omega_{\rm in}$. While all WGMs with $m \leq l_p$ can be excited, WGMs with $|m| \approx l_p$ strongly dominate when the coupling is nearly adiabatic.

Keeping the notation $Q \equiv \{\nu', l', m', \mathrm{TM}\}$, and $A \equiv \{\nu_s, l_s, m_s\}$ we now turn to the transmission power spectrum.

2.4.2. Transmission

Because of their relatively low frequencies, magnons typically have much smaller linewidths than the photons [2], i.e. $\bar{\kappa}_A \ll \kappa_Q + \bar{\kappa}_Q$. In this limit $\chi_Q(\omega') \approx \chi_Q(\omega \pm \omega_A)$ in $S_A^{\pm}$ in Eq. (2.23) such that

$$\frac{P_{\rm T}^{\rm TM}(\omega_{\rm out})}{\bar{P}_{\rm in}} = \sum_{A \in \mathrm{SL}} \left[\frac{\bar{\kappa}_A S_A^+ n_A}{\Delta_+^2 + \bar{\kappa}_A^2/4} + \frac{\bar{\kappa}_A S_A^- (n_A + 1)}{\Delta_-^2 + \bar{\kappa}_A^2/4} \right], \tag{2.40}$$

where $\omega_{\rm out}$ is the center frequency of the detector (assumed to contain a filter of a narrow bandwidth) and,

$$S_A^{\pm} = \left| \sum_{P,Q} \frac{\sqrt{\kappa_P \kappa_Q}}{\bar{\kappa}_P + \kappa_P} \frac{G_{PQA}^{\pm}}{\delta_{QA}^{\pm} - i\left(\bar{\kappa}_Q + \kappa_Q\right)/2} \right|^2 . \tag{2.41}$$

Here the sum over P refers to the sum over m in the family of WGMs with frequency $\omega_P = \omega_{\rm in}$, where the latter has been defined in Eq. (2.38), while $\delta_{QA}^{\pm} = \omega_Q - (\omega_{\rm in} \pm \omega_A)$ and $\Delta_{\pm} = \omega_{\rm out} - (\omega_{\rm in} \pm \omega_A)$ are the frequency detunings of the output WGM and the output photon in the detector from the resonance, respectively. The scattering is efficient if both are less than the typical linewidths of WGMs. $P_{\rm T}^{\rm TE} = 0$ since TE → TE scattering is forbidden.

$S_A^{\pm}$ does not depend on $\omega_{\rm out}$ anymore, so each term in the sum of Eq. (2.40) is a Lorentzian centered at $\omega_{\rm out} = \omega_{\rm in} \pm \omega_A$ with width $\bar{\kappa}_A$ [14]. Each peak is well resolved if $\bar{\kappa}_A < |\omega_A - \omega_{A' \neq A}|$ [see Fig. 2.4]. For small-L magnons with $|\omega_A - \omega_{A'}| \sim \gamma \mu_0 M_s$ [26] this is the case when $\alpha_G \ll \mu_0 M_s / B_0 \sim 0.1 - 1$, which is easily fulfilled for YIG. We note that in previous experiments [2–4] the Kittel mode is selectively populated via microwave excitations ($n_K \gg n_{A \neq K}$) which overwhelms any other magnons, and thus only one peak was observed.

The peak height at $\Delta_{\pm} = 0$ and integrated power $\bar{P}_{\rm T}$ are governed by the magnon linewidth ($\bar{\kappa}_A$), magnon occupation (n_A), and $S_A^{\pm}$ (interpreted below). We may write

$$\bar{P}_{\rm T} = \int \frac{d\omega'}{2\pi} P_{\rm T}^{\rm TM}(\omega') = \sum_{A \in \mathrm{SL}} \left[\bar{P}_A^+ + \bar{P}_A^- \right], \tag{2.42}$$

where $\bar{P}_A^- = S_A^-(n_A + 1)\bar{P}_{\rm in}$ and $\bar{P}_A^+ = S_A^+ n_A \bar{P}_{\rm in}$ is carried by photons that underwent Stokes and anti-Stokes scattering respectively by A-magnons, corresponding to the integral of $P_{\rm T}$ across individual peaks in Eq. (2.40). We can therefore interpret $S_A^{\pm}$ as the photon scattering probability from the contribution of many processes $P \to Q$ by the magnon mode A. In the following, we discuss S first for the Kittel mode and then for other small-L magnons.

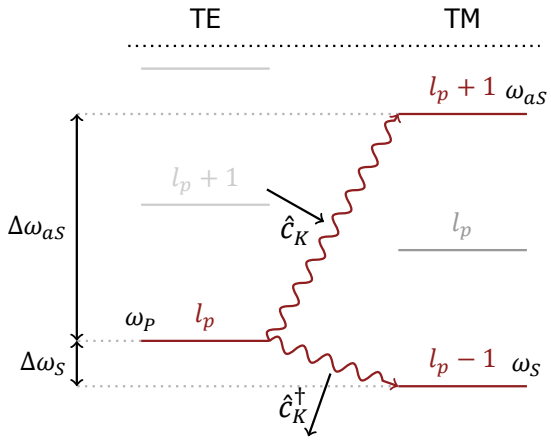

Figure 2.3: Scattering by the Kittel magnon: Angular momentum conservation fixes the final states [see Eq. (2.27)]. The wavy lines denotes the transitions associated with creation or annihilation of the Kittel mode. Referring to Fig.2.2, $\Delta\omega_{aS} = \Delta\omega_{\mathrm{FSR}} + \Delta\omega_{\mathrm{BF}}$ and $\Delta\omega_S = \Delta\omega_{\mathrm{FSR}} - \Delta\omega_{\mathrm{BF}}$. Typical numbers are $\Delta\omega_S \sim 1 - 20$ GHz and $\Delta\omega_{aS} \sim 100 - 500$ GHz for a YIG radius of $a \sim 100 - 500\,\mu$m.

Kittel mode: The Kittel mode $K = \{0, 1, 1\}$ can scatter a WGM $P = \{1, l_p, m, \mathrm{TE}\}$ into either $S = \{1, l_p - 1, m - 1, \mathrm{TM}\}$ or $aS = \{1, l_p + 1, m + 1, \mathrm{TM}\}$ [see the selection rules in Eq. (2.27)]. The optical transitions, valid for all m, are shown in Fig. 2.3. In our example, $\Delta\omega_S = \Delta\omega_{\mathrm{FSR}} - \Delta\omega_{\mathrm{BF}} = 2\pi \times 7.5$ GHz and $\Delta\omega_{aS} = \Delta\omega_{\mathrm{FSR}} + \Delta\omega_{\mathrm{BF}} = 2\pi \times 209$ GHz. For magnon frequencies $\sim 1 - 10$ GHz, the anti-Stokes scattering is highly non-resonant.

By the magnetic field we can tune to the resonance condition $\omega_K = \omega_P - \omega_S = \Delta\omega_{\mathrm{FSR}} - \Delta\omega_{\mathrm{BF}}$, where $\omega_K = \gamma(B_0 - \mu_0 M_s)$. Then, the Stokes scattering probability is maximized

$$S_K^- = |g_-|^2 \left| \sum_m \frac{\sqrt{2\kappa_P}}{\kappa_P + \bar{\kappa}_P} \frac{\sqrt{2\kappa_S}}{\kappa_S + \bar{\kappa}_S} \right|^2 . \tag{2.43}$$

The pre-factor $|g_-|^2$ is governed by the optomagnonic coupling in the sphere, while the second factor is a sum over the optical impedance matching parameters [27, 28] that determine the efficiency of the optical coupling. We find a lower bound for S_K^- by assuming that only the $m = l$ mode contributes. For $\bar{\kappa}_P = \bar{\kappa}_S = \kappa_P = \kappa_S$ with $m = l$ and an optical quality factor of $\omega_P/\bar{\kappa}_P = 10^6$ comparable to experiments [2, 4], $S_K^- = 2 \times 10^{-17}$. At $T = 300\,\mathrm{K}$, the number of magnons at $\omega_K = 2\pi \times 7$ GHz is $n_K = 835$, which leads to the scattered power of $\bar{P}_K^-/\bar{P}_{\mathrm{in}} = 1.5 \times 10^{-14}$. We note that the actual output power might be larger when more WGMs contribute to the above sum. We did not attempt to compute the power by including all such scattering events.

For the same magnetic field, the anti-Stokes scattering is detuned from a resonance by $\omega_{aS} - \omega_P - \omega_K = 2\Delta\omega_{\mathrm{BF}}$. For $2\Delta\omega_{\mathrm{BF}} \gg \bar{\kappa}_{aS}, \kappa_{aS}$, we obtain the S-aS

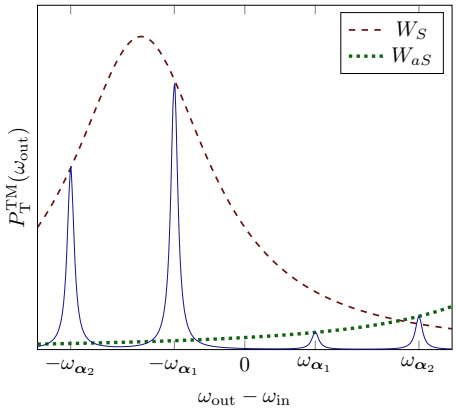

Figure 2.4: Schematic inelastic scattering lineshape with two contributing magnon A_1 and A_2 with constant coupling $G^{\pm}$. The spectra can be written as the convolution of magnetic and optical Lorentzian functions (solid line). The sharp peaks located symmetrically around the origin are centered at the magnon mode frequencies with broadening governed by the magnetization damping. The lines, W_S and W_{aS} are envelope functions defined in the text. They are separated by $2\Delta\omega_{\mathrm{FSR}}$ and broadened by optical decay rates. The widths of all Lorentzians have been exaggerated for clarity. The actual numbers are $\kappa_{S,aS} \sim 2\pi \times 1\,\mathrm{GHz}$ and $\kappa_A \sim 2\pi \times 1\,\mathrm{MHz}$ [2] implying very small magnon lines inside a wide WGM Lorentzian.

intensity ratio

$$\frac{\bar{P}_K^-}{\bar{P}_K^+} \approx \frac{n_K + 1}{n_K} \left| \frac{g_-}{g_+} \frac{2\Delta\omega_{\mathrm{BF}}}{\bar{\kappa}_S + \kappa_S} \right|^2 . \tag{2.44}$$

Three mechanisms contribute to this ratio. The fraction $(n_K + 1)/n_K$ can be an important factor when $n_K \lesssim 1$ at low temperatures, but not at room temperature. The ratio of the microscopic scattering amplitudes

$$\frac{g_-}{g_+} = \frac{\Psi_{LB}^{(2)} - \Psi_{CB}}{\Psi_{LB}^{(2)} + \Psi_{CB}}. \tag{2.45}$$

can for instance be determined by BLS spectroscopy. Values in the range $0.1 < |g_-/g_+|^2 < 10$ have been reported for YIG, depending on the magnetization direction and frequency [5, 29]. For the parameters and configuration here, we find $g_-/g_+ = -0.4$. The main reason for the observed large asymmetry [2–4] is therefore the non-resonant nature of the anti-Stokes scattering caused by the geometric and magnetic birefringence [see Eq. (2.36)]. Inserting the parameters introduced above, we find for the S-aS ratio $\bar{P}_K^-/\bar{P}_K^+ \approx S_K^-/S_K^+ = 2 \times 10^4$.

Small-L magnons: We now discuss $S_A^{\pm}$, with $A = \{\nu_s, l_s, m_s\}$, for general small-L magnons that gives the total power in each peak [see below Eq. (2.42)]. Here we refrain from accurately computing the contributions from different magnon modes to the spectrum that have recently been observed [14, 15]. Instead, we resort to making some qualitative observations. From Eq. (2.41), we see that S_A involves a sum over all (symmetry-allowed) transition amplitudes, $P \to Q$, that in principle can

cause interference effects. However, by choosing an appropriate magnetic field, the Stokes scattering is dominated strongly by the transition l_p to $l_p - 1$ while other transitions are non-resonant. This can be done if the magnon band, $= \gamma\mu_0 M_s/2$ [26, 30] ($\sim 2\pi \times 1$GHz for YIG), is not too large compared to the WGM linewidths (discussed in detail below). If this holds, we can ignore the non-resonant terms in the summation of Eq. (2.41) for S_A^-. Further, G_{PQA}^- is non-zero only if the z-component of angular momentum is conserved, i.e. $m' = m - m_s$. Thus, for a given A and $P = \{1, l_p, m, \mathrm{TE}\}$ the WGM $S = \{1, l_p - 1, m - m_s, \mathrm{TM}\}$ dominates. If $\kappa_S \neq 0$, we can observe this scattering. The anti-Stokes lines are caused by (non-resonant) scattering into different $aS = \{1, l_{aS}, m + m_s, \mathrm{TM}\}$ with $l_{aS} \geq l_p$ and $|m + m_s| \leq l_{aS}$ that can be calculated by Eq. (2.41).

$S_A^{\pm}$ depends on the angular momenta and the energy of A via the optomagnonic coupling G and the detuning δ respectively [see Eq. (2.41)]. BLS experiments are the method of choice to measure quasiparticle spectra, and this holds also for the present configuration. The WGMs transmission spectra sample the amplitude of the magnetization dynamics at the surfaces and are restricted by angular momentum conservation rules via the CG coefficients [see Eqs. (2.30) and (2.31)]. This implies that the total angular momentum should be approximately conserved, i.e. $G_{PSA}^- \approx 0$ for $l_s \gg 1$, restricting the number of optically active magnons; for $l_s \geq 10$ peak heights are estimated from the CG coefficients to be less than 2% of the Kittel mode. The lowest lying peaks are expected for $A = \{0, 2, 2\}, \{0, 2, 1\}, \{1, 1, 1\}$, with frequencies discussed briefly in Sec. 1.2. Similar restrictions hold for anti-Stokes scattering.

In S_A^- the frequency $|\delta_{QA}^-| = |\omega_{\mathrm{in}} - \omega_A - \omega_S|$ is the degree of non-resonance. When all symmetry-allowed G^- are the same, each magnon peak in the Stokes spectrum are proportional to the density of state of the S-WGM at the peak center

$$W_S(\omega_{\mathrm{out}}) \propto \frac{\kappa_S + \bar{\kappa}_S}{4(\omega_{\mathrm{in}} - \Delta\omega_S - \omega_{\mathrm{out}})^2 + (\kappa_S + \bar{\kappa}_S)^2}, \tag{2.46}$$

as shown in Fig. 2.4 (red dashed lines), where $\omega_{\mathrm{out}} = \omega_{\mathrm{in}} - \omega_A$. Here, $\Delta\omega_S$ is defined in Fig. 2.3. Only magnons with frequencies in a window of the order $\pm(\kappa_S + \bar{\kappa}_S)$ around $\Delta\omega_S$ are observable. This shows that we can optimize the scattering by shifting the magnon frequency, via an applied field.

The anti-Stokes scattering for $l_{aS} = l_p + 1$ is plotted schematically in Fig. 2.4. Here the peak heights are proportional to

$$W_{aS}(\omega_{\mathrm{out}}) \propto \frac{\kappa_{aS} + \bar{\kappa}_{aS}}{4(\omega_{\mathrm{in}} + \Delta\omega_{aS} - \omega_{\mathrm{out}})^2 + (\kappa_{aS} + \bar{\kappa}_{aS})^2}, \tag{2.47}$$

is shown in Fig. 2.4 (green dotted lines) with $\omega_{\mathrm{out}} = \omega_{\mathrm{in}} + \omega_A$. Here $\Delta\omega_{aS}$ is defined in Fig. 2.3. Similar formulas hold for other l_{aS} adding up to the total anti-Stokes peaks. The total number of observable peaks depends on G^+ that will distort the Lorentzian envelope for large detunings.

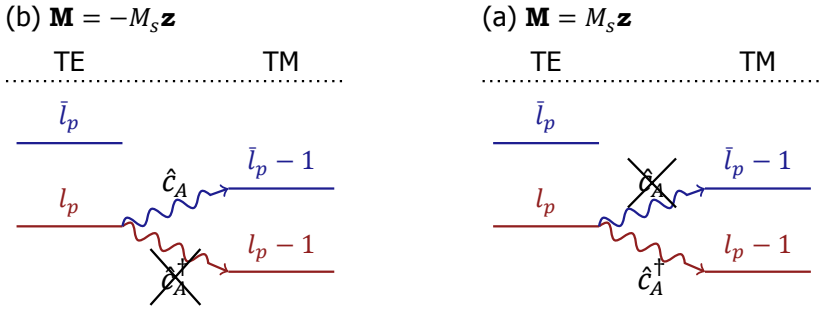

Figure 2.5: Reflection by a Damon-Eshbach mode for (a) $\mathbf{M} = M_s\hat{\mathbf{z}}$ and (b) $\mathbf{M} = -M_s\hat{\mathbf{z}}$. Due to the chirality of DE magnons, one of the Stokes or anti-Stokes transitions is forbidden, depending on the direction of the magnetization.

2.4.3. Reflection

We now turn to the inelastically reflected power. In a sphere, the DE magnons are degenerate at $\omega_{\mathrm{DE}} = \gamma\left(B_0 - 5\mu_0 M_s/6\right)$ [10, 30]. Therefore, only one Stokes peak is expected, to which the scattering amplitudes of all DE magnons contribute. Eq. (2.23) can then be simplified to

$$\frac{P_{\mathrm{R}}^{\mathrm{TM}}(\omega_{\mathrm{out}})}{\bar{P}_{\mathrm{in}}} = \frac{\bar{\kappa}_{\mathrm{DE}}(n_{\mathrm{DE}}+1)}{\left(\omega_{\mathrm{out}} - \omega_{\mathrm{in}} + \omega_{\mathrm{DE}}\right)^2 + \bar{\kappa}_{\mathrm{DE}}^2/4} \sum_{A\in\mathrm{LL}} S_A^-. \tag{2.48}$$

where $A = \{\nu_s, l_s \gg 1, l_s \geq m_s \gg 1\}$, $\omega_A = \omega_{\mathrm{DE}}$, $\kappa_A = \kappa_{\mathrm{DE}} = \alpha_G\omega_{\mathrm{DE}}$ and, at elevated temperatures, $n_A = n_{\mathrm{DE}} = k_B T/(\hbar\omega_A)$. $P_{\mathrm{R}}^{\mathrm{TE}} = 0$ since TE $\rightarrow$ TE scattering is forbidden. P_{R} is a Lorentzian centered at $\omega_P - \omega_{\mathrm{DE}}$ with a width κ_{DE}. The total integrated power over the peak

$$\bar{P}_{\mathrm{R}} \triangleq \int \frac{d\omega_{\mathrm{out}}}{2\pi} P_{\mathrm{R}}^{\mathrm{TM}}(\omega'), \tag{2.49}$$

is then

$$\frac{\bar{P}_{\mathrm{R}}}{\bar{P}_{\mathrm{in}}} = \sum_{A\in\mathrm{LL}} \left| \sum_{P,Q} \frac{2\sqrt{\kappa_P\kappa_Q}}{\bar{\kappa}_P + \kappa_P} \frac{G_{PQA}^- \sqrt{n_{\mathrm{DE}}+1}}{i\delta_{QA}^- + (\bar{\kappa}_Q + \kappa_Q)/2} \right|^2. \tag{2.50}$$

The summation over P includes all allowed $m > 0$, while the Q modes circle in the opposite direction $m' < 0$.

Using Fig. 2.2, we see that $Q = \{1, l_p - 1, m', \mathrm{TM}\}$ for $m' = m - m_s < 0$ are the only resonant final states for magnon frequencies $< 2\pi \times 20\,\mathrm{GHz}$ [illustrated in Fig. 2.5(a)]. A magnetic field ($\sim 1\,\mathrm{T}$) can tune the system into the resonant condition $\omega_{\mathrm{DE}} = \Delta\omega_{\mathrm{FSR}} - \Delta\omega_{\mathrm{BF}}$. We can estimate a lower bound of the output power by assuming that only $m = l_p$ and $m' = -\left(l_p - 1\right)$ modes couple to the fiber and the magnons with $m_s = l_s = 2l_p - 1$ dominate. There is only one state A with $m_s = l_s$

labeled as $\nu_s = 0$ [see Sec. 1.2], hence

$$\frac{\bar{P}_{\mathrm{R}}}{\bar{P}_{\mathrm{in}}} = \frac{2\kappa_P}{\left(\kappa_P + \bar{\kappa}_P\right)^2} \frac{2\kappa_Q}{\left(\kappa_Q + \bar{\kappa}_Q\right)^2} \left|g_- \Xi_-\right|^2 \left(n_{\mathrm{DE}} + 1\right), \tag{2.51}$$

where Ξ_- has been defined in Eq. (2.33). Using the parameters for YIG given above, we arrive at the estimate $\bar{P}_{\mathrm{R}}/\bar{P}_{\mathrm{in}} = 4 \times 10^{-13}$ at $T = 300\,\mathrm{K}$. The actual output power will be larger, depending on the optical coupling and multiple contributing DE magnons.

Since the WGMs are spatially extended compared to the DE modes, the radial overlap interface for $\nu_s \neq 0$ is suppressed. While for small-L magnons with approximately constant amplitude, the orthogonality of the WGMs efficiently suppresses inter-branch scattering with $\nu \neq \nu'$, the DE modes are localized to the surface, which allows scattering between WGMs $\nu' \neq \nu$. In the present configuration with $\mathbf{M} \approx M_s \hat{\mathbf{z}}$ the $\nu = 1$ intra-branch scattering dominates, because $\nu' \neq \nu$ transition are non-resonant (see Fig. 2.5). The situation is different for $\mathbf{M} \approx -M_s \hat{\mathbf{z}}$ (see next section).

The angular momentum of the WGMs for infrared light is typically of the order of $l_p \sim 10^3$. The DE magnons that reflect these photons have angular moments of the same order. In YIG spheres with $a \sim 100\,\mu\mathrm{m}$ exchange effects become significant only for $l_s > 10^4$, implying that we can neglect exchange. For exchange energy smaller than the magnetostatic energy, $\sim \gamma\mu_0 M_s$, we expect the magnons to be chiral still, but with a different magnon spatial distribution affecting the overlap.

2.5. Other configurations

The above analysis focuses on a TE polarized incident photons in Fig. 2.1 that couple to the $\nu = 1$ WGM. We now briefly discuss other configurations involving a different WGM, magnetization direction, and polarization. The conclusions are summarized in Fig. 2.6 (not to scale).

Other WGMs: Magnons close to the Kittel mode with small angular momentum and nearly constant amplitude over the sphere can scatter WGMs with the same number of nodes $\nu = \nu'$ only. The $\nu = 1$ mode is expected to dominate because of the larger evanescent coupling. DE magnons may form an exception, since on magnetization reversal inter-branch scattering should become observable (next paragraph).

Magnetization: The results for $\mathbf{M} \approx M_s \hat{\mathbf{z}}$ can be used to understand the scattering after magnetization reversal $\mathbf{M} \approx -M_s \hat{\mathbf{z}}$. This inverts the magnon angular momenta m_s in the selection rules, which might lead to a naïve expectation that we simply have to exchange Stokes and anti-Stokes scattering. This is not the case, however, as we discuss now for the Kittel mode. For simplicity, let's consider only the dominant optical mode with $m = l_p$ which has simple selection rules, viz. $l_p \to l_p \pm 1$. The Stokes scattering, in this case, occurs from l_p to $l_p + 1$ because of angular momentum conservation. This has a large detuning of $\Delta\omega_{aS} + \omega_A$ [$\Delta\omega_{aS}$ defined in Fig. 2.3]. The anti-Stokes transition $l_p \to l_p - 1$ (consistent with angular momentum conservation) is also non-resonant with a detuning of $\Delta\omega_S + \omega_A$. There-

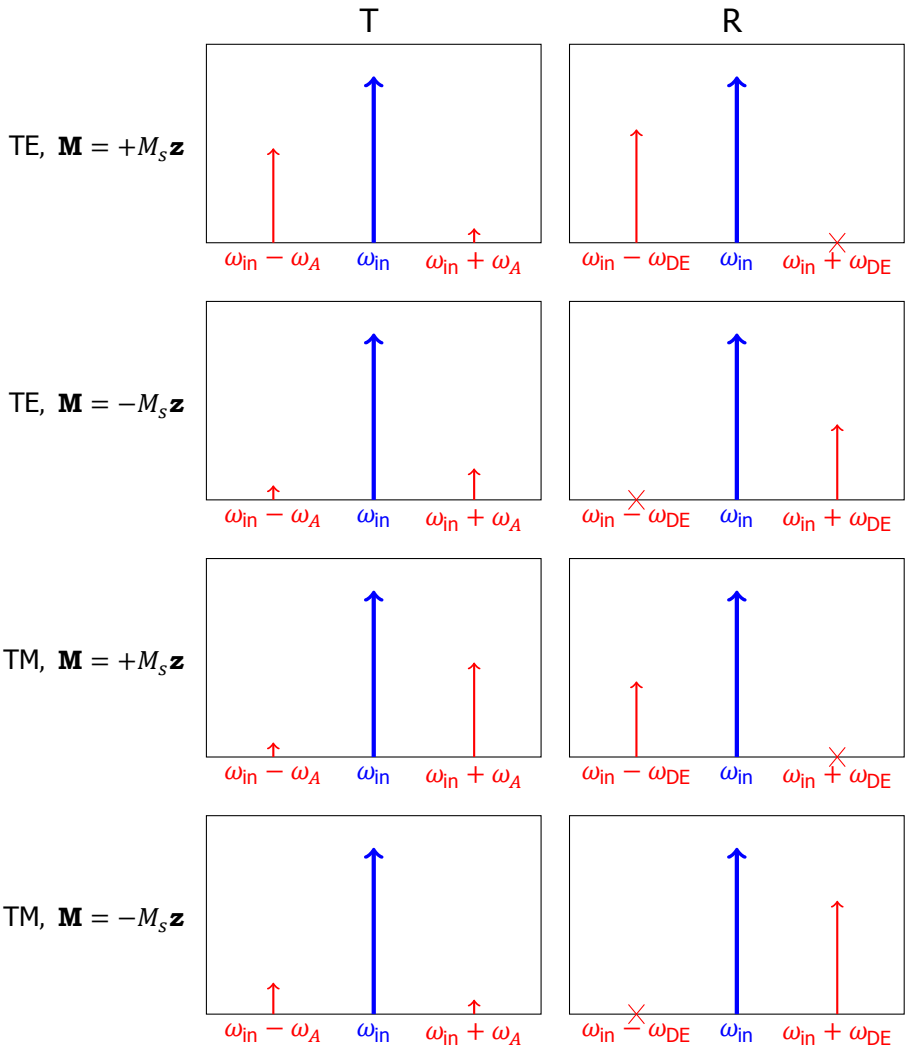

Figure 2.6: Schematic light scattering spectra by a magnetic sphere in proximity to a single mode optical fiber, emphasizing the S-aS asymmetry. The blue arrow marks the frequency ω_{in} of light input and the panel T(R) denotes the transmission(reflection) spectra with Stokes and anti-Stokes lines. ω_A and ω_{DE} are the resonance frequencies of magnons involved in the transmission and reflection, respectively. Each column corresponds to one of the four cases, $\sigma \in \{\text{TE}, \text{TM}\}$ or $\mathbf{M} \parallel \pm\hat{\mathbf{z}}$. A cross denotes complete absence of a peak by chirality selection. The peak heights are not on scale, but peaks with the same height have power in the same order-of-magnitude. We assume that the input frequency and the magnetic field have been tuned to the resonant scattering condition in each case as discussed in the main text.

fore, the reduction of angular momentum of WGM is accompanied by an increase in energy and vice versa, which is not favorable for scattering [see Fig 2.2], decreasing both the peaks. For the parameters of the YIG sphere used before, we find in this case $\bar{P}_K^+/\bar{P}_{\rm in} \sim 10^{-16}$ and a weaker (inverted) S-aS asymmetry $\bar{P}_K^+/\bar{P}_K^- \sim 100$.

The chirality of DE magnons is reversed with magnetization, and anti-Stokes scattering becomes allowed while the Stokes scattering is forbidden. Using Fig. 2.5, we see that the scattering cannot be resonant now for intra-branch scattering. However, the WGM of the $\nu = 2$ branch is close in frequency and we can choose $\omega_{\rm DE} = \Delta\omega_{\rm BF} - \Delta\omega_{\rm FSR} + \Delta\omega_{\rm RG} = 2\pi \times 8.8$ GHz in our case. Therefore, we can still have resonant reflection under certain conditions, i.e. the evanescent coupling of $\nu = 2$ branch is significant and the above detuning is not too large.

TM input: All the arguments, so far, can be repeated for the case of TM polarized light input. We can understand the schematic results in Fig. 2.6 by time-reversal symmetry arguments. The time-reversal operator, $\mathcal{T}$, inverts the magnetization and the WGM circulation direction, so the direction of a WGM w.r.t the magnetization is conserved. $\mathcal{T}$ exchanges magnon annihilation and creation as well as input WGM and scattered WGM. The last condition implies that both the polarization and the direction of motion of WGMs must be interchanged. Thus, the transmission spectrum for TM input when $\mathbf{M} = \pm M_s\hat{\boldsymbol{z}}$ is recovered by interchanging Stokes and anti-Stokes scattering in the transmission of TE input when $\mathbf{M} = \pm M_s\hat{\boldsymbol{z}}$. On the other hand, the reflection spectrum for $\{\text{TE},\ \mathbf{M} = \pm M_s\hat{\boldsymbol{z}}\}$ is mirror symmetric (across the input frequency) with $\{\text{TM},\ \mathbf{M} = \mp M_s\hat{\boldsymbol{z}}\}$.

2.6. Discussion and outlook

Our theory demonstrates that the transmission (reflection) spectra of inelastically scattered photon involves magnons with small (large) angular momentum. Both show a pronounced asymmetry in the probability of Stokes and the anti-Stokes scattering, albeit for very different reasons (discussed below). The conclusions hold for (approximately) spherical cavities with magnetizations perpendicular to the WGM orbits. Here we briefly discuss non-spherical samples and general magnetization directions. In the following $\mathbf{L}_W$ and $\mathbf{L}_m$ denote the angular momenta of WGMs and magnons, respectively.

Our finding that the pronounced S-aS asymmetry observed in forward scattering [2–4] is caused by linear birefringence agrees with that of [4]. The present results can be carried to dielectric shapes with closed extreme orbits with sufficiently weak curvature, such as bottlenecks, rings, etc. This implies that the forward scattering power is increased for oblate ellipsoid with smaller volume and equal curvature at the equator, increasing the relative overlap volume [see Eq. (2.27)].

To the best of our knowledge, back scattering of light by magnons in spherical cavities has not yet been discussed in the literature. We find a perfect selection rule for S-aS back-scattering by DE magnetostatic spin waves. The physical reason is their chirality that locks the sign of the orbital angular momenta to the magnetization direction. The interactions between DE magnons and WGMs is enhanced because (i) they are confined to the same equatorial region of the sphere and (ii) the dwell time in which the interaction can take place is long when dissipation is weak. While

the reflection power estimated here is not yet very high, engineering the spatial distribution of WGMs might lead to the coveted strong interaction between light and magnetism. We will discuss such optimizations in a future article.

The analysis for arbitrary magnetization directions is more complex because the rotational symmetry about z-axis is broken. In the case of transmission $|\mathbf{L}_m| \ll |\mathbf{L}_W|$, so the WGMs are only slightly changed after scattering. Thus we expect the spatial overlap to be the same as our work. The CG coefficients have to be generalized for non-collinear magnetization changing the selection rules but will perhaps not change the order of magnitude of the coupling constants G. The change in selection rules will significantly affect the detunings, thus the peak heights and the S-aS asymmetry, which we believe to be the major change. As we discussed before, inverting the magnetization inverts the S-aS asymmetry. For the particular case of in-plane magnetization, say $\mathbf{M} = M_s\hat{\mathbf{x}}$, we expect the S-aS asymmetry in transmission to be suppressed. This can be understood by analogy with a spin-1/2 system where the angular momentum $L_m\hat{\mathbf{x}}$ is formed as a coherent linear superposition of $L_m\hat{\mathbf{z}}$ and $-L_m\hat{\mathbf{z}}$ and adding or subtracting $L_m\hat{\mathbf{x}}$ can generate scattering from l to $l-1$ with equal probability. However, in this case too, the Stokes scattering is resonant while the anti-Stokes is detuned. In the in-plane magnetization configuration the photons also experience inhomogeneous Faraday rotation and Cotton-Mouton ellipticity [23, 31, 32]. This causes a small ellipticity in the WGMs that contributes to the light scattering only to higher order. The treatment of light reflection for a general magnetization direction is fairly complicated as $\mathbf{L}_W$ changes significantly after scattering and therefore beyond the scope of this work.

While (undoped) YIG has excellent magnetic quality, its magneto-optical effects are weak [24]. The best material for cavity optomagnonics would maximize $S^{\pm}$ [see Eq. (2.41)]. It should have a window of high transparency, i.e. small optical losses (eventually by polishing the surface [2]), and large MO effects that bolster the $g_{\pm}$ [Eq. (2.28)]. Provided that it is much smaller than the optical broadening, the magnon linewidth governed by the Gilbert damping does not play a role in the integrated scattered power. Doping YIG or substituting yttrium by magnetic rare earth atoms increases MO effects but may also lead to a deterioration of the optical and magnetic quality [33].

While we considered BLS by magnons, light can be scattered by other excitations, such as phonons. The latter generate inelastic scattering at $\omega_{\text{in}} \pm \omega_{ph}$ where ω_{ph} are optically active phonon frequencies. Unless a phonon is resonant with any of the relevant magnons, the two scattering are independent and can be easily separated from the magnetic signals by e.g. changing the magnetic field.

In summary, we studied BLS by magnons in spherical cavities, restricting to WGMs, with the magnetization perpendicular to WGM orbit. We expect our discussion of BLS by magnons in WGM cavities to hold for more general geometries, but not for a general magnetization direction. The expressions derived here can be used for improving the coupling between magnons and phonons. The dependence of the scattered power on the input mode as illustrated by Fig. 2.6, allows controllable energy transfer between magnet and light. DE magnons can be pumped or annihilated selectively by reflection of light. Similarly, the low-L magnons can

be pumped or cooled by light depending on the polarization of the input. A forthcoming article is devoted to the thermodynamics of light scattering by magnetic spheres.

We acknowledge helpful discussions with Koji Usami and Koji Satoh. This work is supported by the DFG Priority Programme 1538 "Spin-Caloric Transport", the NWO, and JSPS Grants-in-Aid for Scientific Research (Grant Nos. 25247056, 25220910, and 26103006).

2.7. Appendix: Scattering amplitudes

In this Appendix, we calculate the scattering amplitudes of a TE WGM into a TM WGM for both forward and back scattering. To this end we use the expressions for the optical and magnonic fields in Secs. 1.2 and 1.4 to calculate the integrals in Eqs. (1.34).

2.7.1. Kittel mode

Consider a WGM with index $P \equiv \{\nu, l, m, TE\}$ that scatters into $Q \equiv \{r', l', m', TM\}$ by the Kittel mode, $A \equiv \{0, 1, 1\}$. Throughout this section $l, m \gg 1, |l - m|$ and $l', m' \gg 1, |l' - m'|$. The coupling integrals, Eq. (1.34), can be written as

$$G^{\pm}_{PQA} = \frac{\mathcal{G}_{\pm} M_u}{4\hbar} I_{\pm}, \tag{2.52}$$

where

$$I_{\pm} = \int_{|r|<a} E_{P,z} E^*_{Q,\pm} d\mathbf{r}. \tag{2.53}$$

Putting the distribution of electric fields [see Sec. 1.4] we get

$$I_{\pm} \approx i\mathcal{E}_P \mathcal{E}_Q \int \left(j_l(k_P r) Y^m_l\right) \left(j_{l'}(k_Q r) \sin\theta e^{\pm i\phi} (Y^{m'}_{l'})^*\right) d\mathbf{r}. \tag{2.54}$$

For large l, we have a recursive relation, $\sin\theta e^{\pm i\phi} Y^{m'}_{l'} = Y^{m'\pm 1}_{l'\pm 1}$, giving

$$\begin{aligned} I_{\pm} &\approx i\mathcal{E}_P \mathcal{E}_Q \int j_l(k_P r) j_{l'}(k_Q r) Y^m_l \left(Y^{m'\mp 1}_{l'\mp 1}\right)^* d\mathbf{r} \\ &= i\mathcal{E}_P \mathcal{E}_Q \delta_{l,l'\mp 1} \delta_{m,m'\mp 1} \int r^2 dr j_l(k_P r) j_{l'}(k_Q r). \end{aligned} \tag{2.55}$$

where we used the orthonormality of the SHs. Since the integral is dominated by $r \approx a$, we can use the asymptotic form of the Bessel function, Eq. (1.24) and the orthogonality relation

$$\int_0^\infty dt\ \mathrm{Ai}(t - \beta_\nu)\mathrm{Ai}(t - \beta_{\nu'}) = \delta_{\nu,\nu'} \left(\mathrm{Ai}'(-\beta_\nu)\right)^2, \tag{2.56}$$

to arrive at

$$I_{\pm} \approx i \frac{\hbar\omega_P}{2\epsilon_s} \delta_{\nu,\nu'} \delta_{l,l'\mp 1} \delta_{m,m'\mp 1}, \tag{2.57}$$

for $\epsilon_s \gg \{fM_s, gM_s^2, g'M_s^2\}$. Finally,

$$G^{\pm}_{PQA} = \frac{gM_s \pm f}{2\epsilon_s}\frac{M_s}{\sqrt{sV}} i\omega_p \delta_{\nu,\nu'}\delta_{l,l'\mp 1}\delta_{m,m'\mp 1}, \tag{2.58}$$

which can be written in terms of the MO constants defined in Eqs. (1.14) - (1.15) and lead to Eq. (2.27). The orthonormality of the SHs reflects the conservation of angular momentum and the orthonormality of WGMs in the radial direction leads to the radial selection rule.

2.7.2. DE modes

We calculate scattering of a WGM with $P \equiv \{\nu, l, m, TE\}$ into one with index $Q \equiv \{\nu', l', m', TM\}$ by a particular DE magnon given by $A \equiv \{0, l_s, l_s\}$. We take the case of $m > 0$ which implies $m' < 0$ as discussed in the main text, Sec. 2.3.2. Here, we assume $l, m \gg 1, |l - m|$, and similarly $l', |m'| \gg 1, |l' + m'|$. The coupling constants

$$\hbar G^{\pm}_{PQA} = \frac{i\mathcal{G}_{\pm}\mathcal{E}_P\mathcal{E}_Q M_{l_s} a^3}{4}\mathcal{R}\Theta_{\pm}, \tag{2.59}$$

where we divided the integrals into the angular (Θ) and the radial ($\mathcal{R}$) parts. The angular integral is

$$\Theta_{\pm} = \int d\Omega Y_l^m \left[\sin\theta e^{\pm i\phi}\left(Y_{l'}^{m'}\right)^*\right]\left(\sin\theta e^{\pm i\phi}\right)^{l_s-1}, \tag{2.60}$$

where $d\Omega = \sin\theta d\theta d\phi$ is the angular differential. As $Y_l^m \sim e^{im\phi}$, we get that $\Theta_{\pm}$ is non-zero only if $m - m' \pm l_s = 0$. As discussed in the text, $m' \approx -m$, so $\Theta_+ = 0$. Θ_- can be evaluated by using $(Y_L^M)^* = (-1)^M Y_L^{-M}$,

$$Y_L^L \approx \frac{L^{1/4}}{\sqrt{2}\,\pi^{3/4}}\sin^L\theta e^{iL\phi}, \tag{2.61}$$

and the identity,

$$\int d\Omega\, Y_{L_1}^{M_1} Y_{L_2}^{M_2}\left(Y_{L_3}^{M_3}\right)^* \approx \sqrt{\frac{L_1 L_2}{2\pi L_3}}\langle L_1, M_1; L_2, M_2|L_3, M_3\rangle\langle L_1, 0; L_2, 0|L_3, 0\rangle, \tag{2.62}$$

where the approximations holds for $L_i \gg 1$ for $i \in \{1, 2, 3\}$. We get

$$\Theta_- = \frac{\pi^{3/4}}{l_s^{3/4}}\sqrt{\frac{ll'}{\pi}}\langle l, m; l', |m'|| \; l_s, m_s\rangle\langle l, 0; l', 0| \; l_s, 0\rangle. \tag{2.63}$$

The radial integral is

$$\mathcal{R} = \int_0^1 j_l(k_P a\rho)\left[j_{l'}(k_Q a\rho) - j'_{l'}(k_Q a\rho)\right]\rho^{l_s+1}d\rho, \tag{2.64}$$

where $\rho = r/a$. It quantifies the overlap between the DE modes and WGMs in the radial direction. It can be estimated by realizing that $\rho^{l_s} \approx \exp(-l_s(1-\rho))$ for $l_s \gg 1$. Therefore, the magnetization of the DE magnon decays rapidly in a reduced length scale of $1/l_s$ (or in a length scale of a/l_s). In such a small length, we can approximate WGMs by their value at the surface ($\rho = 1$) giving

$$\mathcal{R} \approx \frac{j_l(k_P a)}{l_s}\left[j_{l'}(k_Q a) - j'_{l'}(k_Q a)\right]. \tag{2.65}$$

We use the asymptotic form of the Bessel's function, Eq. (1.24), along with

$$k_P a = l + \left(\beta_\nu - \frac{2^{1/3}P_\sigma}{l^{1/3}}\right)\left(\frac{2}{l}\right)^{1/3}, \tag{2.66}$$

and the Taylor expansion of the Airy's function around its zeroes for large l,

$$\mathrm{Ai}\left(-\beta_\nu + \frac{2^{1/3}P_\sigma}{l^{1/3}}\right) \approx \mathrm{Ai}'(-\beta_\nu)\frac{2^{1/3}P_\sigma}{l^{1/3}}.$$

We can find a similar function for $j_{l'}(k_Q a)$. We simplify

$$\mathcal{R} \approx \frac{\pi}{4}\left(\frac{4}{ll'}\right)^{7/6}\mathrm{Ai}'(-\beta_\nu)\mathrm{Ai}'(-\beta_{\nu'})P_{TE}(1+P_{TM}). \tag{2.67}$$

Putting all the constants in Eq. (2.59), we arrive at the result mentioned in Eq. (2.32).

References

[1] S. Sharma, Y. M. Blanter, and G. E. W. Bauer, *Light scattering by magnons in whispering gallery mode cavities,* Phys. Rev. B **96**, 094412 (2017).

[2] X. Zhang, N. Zhu, C.-L. Zou, and H. X. Tang, *Optomagnonic whispering gallery microresonators,* Phys. Rev. Lett. **117**, 123605 (2016).

[3] A. Osada, R. Hisatomi, A. Noguchi, Y. Tabuchi, R. Yamazaki, K. Usami, M. Sadgrove, R. Yalla, M. Nomura, and Y. Nakamura, *Cavity optomagnonics with spin-orbit coupled photons,* Phys. Rev. Lett. **116**, 223601 (2016).

[4] J. A. Haigh, A. Nunnenkamp, A. J. Ramsay, and A. J. Ferguson, *Triple-resonant brillouin light scattering in magneto-optical cavities,* Phys. Rev. Lett. **117**, 133602 (2016).

[5] W. Wettling, M. G. Cottam, and J. R. Sandercock, *The relation between one-magnon light scattering and the complex magneto-optic effects in yig,* Journal of Physics C: Solid State Physics **8**, 211 (1975).

[6] A. Borovik-Romanov and S. Sinha, *Spin Waves and Magnetic Excitations*, Vol. 22 (Elsevier, 1988) pp. 88–100.

[7] R. E. Camley, P. Grünberg, and C. M. Mayr, *Stokes–anti-stokes asymmetry in brillouin scattering from magnons in thin ferromagnetic films,* Phys. Rev. B **26**, 2609 (1982).

[8] P. Grünberg and F. Metawe, *Light scattering from bulk and surface spin waves in euo,* Phys. Rev. Lett. **39**, 1561 (1977).

[9] M. Grimsditch, A. Malozemoff, and A. Brunsch, *Standing spin waves observed by brillouin scattering in amorphous metallic* $\mathrm{fe_{80}b_{20}}$ *films,* Phys. Rev. Lett. **43**, 711 (1979).

[10] J. R. Eshbach and R. W. Damon, *Surface magnetostatic modes and surface spin waves,* Phys. Rev. **118**, 1208 (1960).

[11] R. Damon and J. Eshbach, *Magnetostatic modes of a ferromagnet slab,* Journal of Physics and Chemistry of Solids **19**, 308 (1961).

[12] R. E. Camley and D. L. Mills, *Surface response of exchange- and dipolar-coupled ferromagnets: Application to light scattering from magnetic surfaces,* Phys. Rev. B **18**, 4821 (1978).

[13] R. E. Camley, T. S. Rahman, and D. L. Mills, *Magnetic excitations in layered media: Spin waves and the light-scattering spectrum,* Phys. Rev. B **27**, 261 (1983).

[14] A. Osada, A. Gloppe, R. Hisatomi, A. Noguchi, R. Yamazaki, M. Nomura, Y. Nakamura, and K. Usami, *Brillouin light scattering by magnetic quasivortices in cavity optomagnonics,* Phys. Rev. Lett. **120**, 133602 (2018).

[15] J. A. Haigh, N. J. Lambert, S. Sharma, Y. M. Blanter, G. E. W. Bauer, and A. J. Ramsay, *Selection rules for cavity-enhanced brillouin light scattering from magnetostatic modes,* Phys. Rev. B **97**, 214423 (2018).

[16] T. Sebastian, K. Schultheiss, B. Obry, B. Hillebrands, H. Schultheiss, and B. Obry, *Micro-focused brillouin light scattering: imaging spin waves at the nanoscale,* Frontiers in Physics **3** (2015), 10.3389/fphy.2015.00035.

[17] C. W. Gardiner and M. J. Collett, *Input and output in damped quantum systems: Quantum stochastic differential equations and the master equation,* Phys. Rev. A **31**, 3761 (1985).

[18] A. A. Clerk, M. H. Devoret, S. M. Girvin, F. Marquardt, and R. J. Schoelkopf, *Introduction to quantum noise, measurement, and amplification,* Rev. Mod. Phys. **82**, 1155 (2010).

[19] Á. Rivas and S. F. Huelga, *Open Quantum Systems: An Introduction* (Springer Berlin Heidelberg, 2012).

[20] L. Landau and E. Lifshitz, *Statistical Physics*, v. 5 (Elsevier Science, 1996).

[21] J. J. Sakurai, *Modern quantum mechanics* (Addison-Wesley, Reading, MA, 1994).

[22] M. J. Humphrey, E. Dale, A. Rosenberger, and D. Bandy, *Calculation of optimal fiber radius and whispering-gallery mode spectra for a fiber-coupled microsphere,* Optics Communications **271**, 124 (2007).

[23] J. A. Haigh, S. Langenfeld, N. J. Lambert, J. J. Baumberg, A. J. Ramsay, A. Nunnenkamp, and A. J. Ferguson, *Magneto-optical coupling in whispering-gallery-mode resonators,* Phys. Rev. A **92**, 063845 (2015).

[24] W. Wettling, *Magneto-optics of ferrites,* Journal of Magnetism and Magnetic Materials **3**, 147 (1976).

[25] M. Wu and A. Hoffmann, *Recent Advances in Magnetic Insulators - From Spintronics to Microwave Applications*, Vol. 64 (Elsevier, 2013) pp. 1–408.

[26] P. C. Fletcher and R. O. Bell, *Ferrimagnetic resonance modes in spheres,* Journal of Applied Physics **30**, 687 (1959), https://doi.org/10.1063/1.1735216 .

[27] P. Biagioni, J.-S. Huang, and B. Hecht, *Nanoantennas for visible and infrared radiation,* Reports on Progress in Physics **75**, 024402 (2012).

[28] M. Afzelius and C. Simon, *Impedance-matched cavity quantum memory,* Phys. Rev. A **82**, 022310 (2010).

[29] J. Sandercock and W. Wettling, *Light scattering from thermal acoustic magnons in yttrium iron garnet,* Solid State Communications **13**, 1729 (1973).

[30] L. R. Walker, *Magnetostatic modes in ferromagnetic resonance,* Phys. Rev. **105**, 390 (1957).

[31] A. D. Fisher, J. N. Lee, E. S. Gaynor, and A. B. Tveten, *Optical guided-wave interactions with magnetostatic waves at microwave frequencies,* Applied Physics Letters **41**, 779 (1982).

[32] S. Lan and M. Hossein-Zadeh, *Faraday effect in high-q whispering-gallery mode optical cavities,* IEEE Photonics Journal **3**, 872 (2011).

[33] T. B. Mitchell and P. E. Wigen, *The faraday rotation of bismuth- and thulium-substituted yttrium iron garnet,* Journal of Applied Physics **61**, 3259 (1987).

3

Selection rules for cavity-enhanced Brillouin light scattering from magnetostatic modes

This chapter has been published as J. A. Haigh, N. J. Lambert, S. Sharma, Y. M. Blanter, G. E. W. Bauer, and A. J. Ramsay Phys. Rev. B **97**, 214423 (2018) [1].

Initial experiments on cavity optomagnonics focused on the Kittel mode, in which the magnetization precesses uniformly across the entire sphere. However, theoretical analysis [2] shows that the enhanced BLS should be large for some spatially varying magnetic modes as well. Due to better spatial overlap with WGMs, these could be expected to have stronger optomagnonic coupling. Here, we discuss the selection rules governing BLS active magnetostatic modes in YIG sphere and discuss experiments to observe it.

Fig. 3.1(b) shows the node-less Kittel mode. The other modes have additional nodal planes in the form of ellipsoids whose number and ellipticity is governed by l_m and q_m, respectively and are shown in Fig. 3.1(c-i). In microwave experiments, strong coupling of several higher order modes to microwave resonators has been achieved [3–5], despite the fact that only the Kittel mode has any net dynamic magnetization. This is possible due to inhomogeneity in either the microwave or the applied static magnetic field. In our experiments, we exploit both to allow us to drive various non-uniform magneto-static modes.

3.1. Experimental setup

A schematic of the experimental setup is shown in Fig. 3.2. A rutile prism coupler is used to optically excite the whispering gallery modes, while the magnetostatic modes are driven by a small loop antenna. The 1 mm diameter YIG sphere is mounted on a ceramic rod.

The WGMs are probed with a tunable external-cavity diode laser with linewidth $\approx$1 MHz. Due to the birefringence of the coupling prism, the reflected linearly polarized input beam and the polarization-rotated scattered beam are spatially separated and can be measured independently. The reflected beam is measured on a photodiode and is used to identify the WGMs. The polarization scattered light is passed through a scanning Fabry-Pérot etalon to spectrally resolve the BLS. Whilst in previous experiments [6, 7] both input polarizations were studied, here we focus solely on measurements for h-input (TM) polarization, where better out-coupling of the BLS light from the birefringent coupling prism is achieved.

For microwave characterization of the magnetostatic modes, we measure absorption dips in the reflection coefficient $|S_{11}|$ of the loop antenna with a vector network analyzer. The static magnetic field is applied using a permanent NdFeB magnet. The magnitude of the magnetic field can be controlled by shifting the position of the magnet relative to the YIG sphere.

3.2. Expected modes active for BLS

We briefly review the modes expected to be active for BLS in our experimental setup using recent theoretical calculations of the optomagnonic coupling constants [2].

A photon in a $\sigma_i = h$ polarized input WGM $\{l_i, m_i, q_i\}$ can undergo anti-Stokes scattering by a magnon $\{l_m, m_m, q_m\}$ into a $\sigma_o = v$ polarized output WGM $\{l_o, m_o, q_o\}$, while Stokes scattering is strongly suppressed [2, 7]. The constraints on the cou-

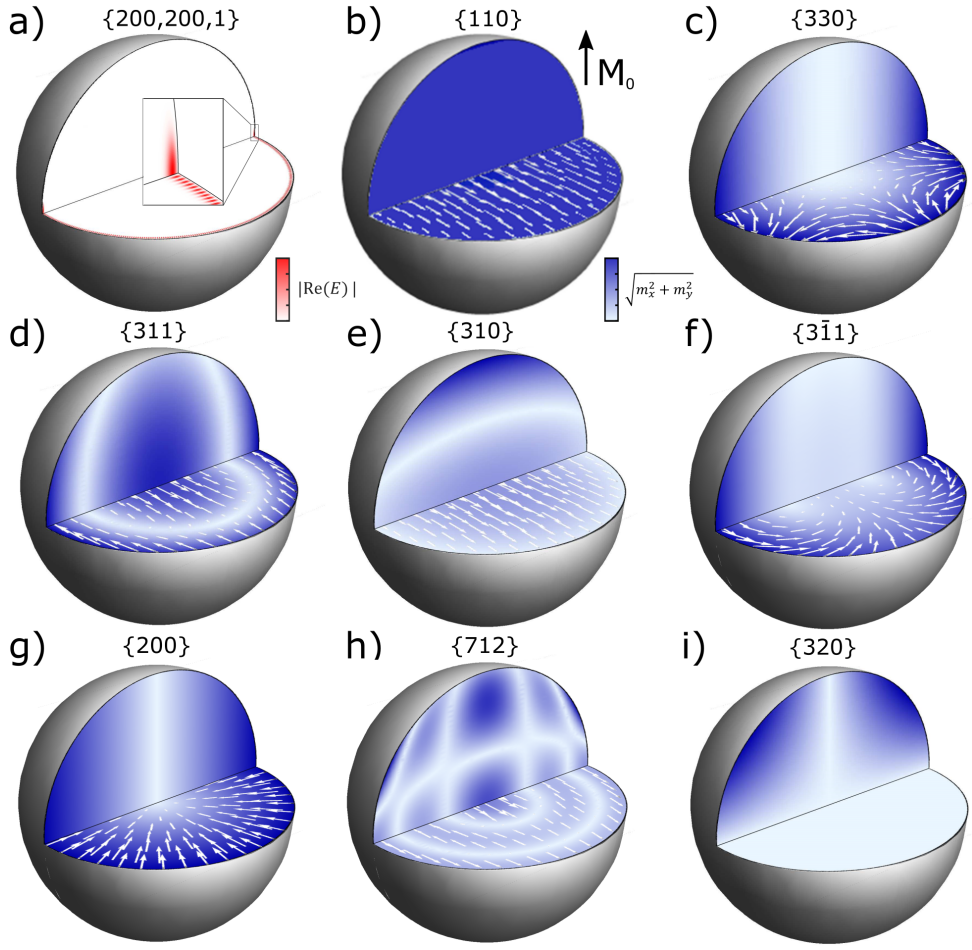

Figure 3.1: Spatial variation of (a) an optical WGM and (b-i) dynamic magnetization modes of a yig sphere. The labels above the spheres are the angular momentum and radial mode numbers $\{l, m, q\}$ (with subscript m for magnetic modes, see text). (a) The in-phase intensity of the electric field for an optical WGM with $l = m = 200$ (in the actual experiment, $l, m \sim 1000$). (b-i) The color indicates the intensity of the dynamic magnetization, while arrows indicate the in-phase direction. Negative mode indices are indicated by an over-bar. The static magnetization M_0 is indicated in (b).

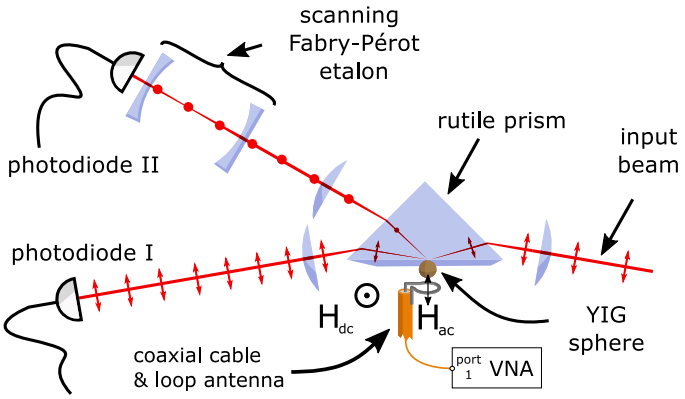

Figure 3.2: Experimental setup. Linearly polarized input light is evanescently coupled into the YIG sphere via a rutile prism. Photodiode I measures the transmitted input beam, in order to identify the WGM resonances. Photodiode II measures the polarization rotated output from the YIG sphere, with a scanning Fabry-Pérot etalon in the beam path providing spectral resolution. A permanent NdFeB magnet saturates the magnetization perpendicular to the WGM orbit. The microwave measurements are made with the loop antenna using a vector network analyzer (VNA).

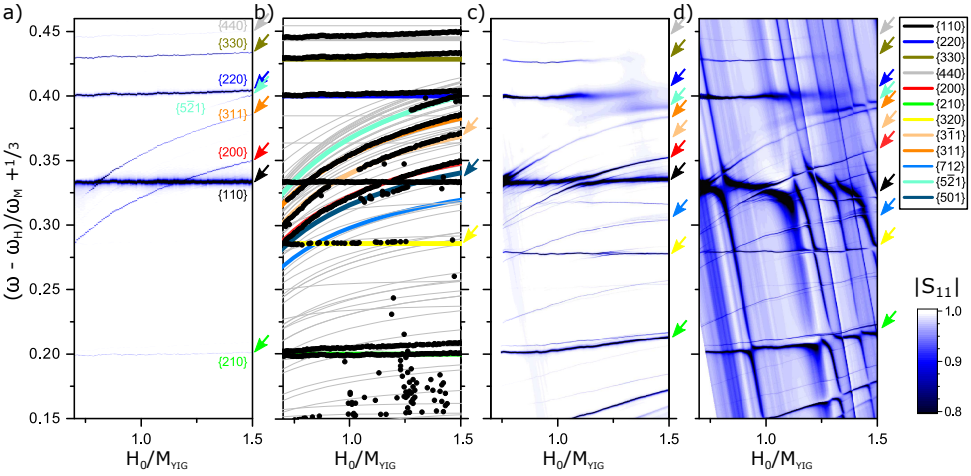

Figure 3.3: Identification of magnetostatic modes from magnetic field dispersion. (a) Microwave reflection coefficient $|S_{11}|$ as a function of magnetic field and reduced frequency $(\omega-\omega_H)/\omega_M+1/3$ measured in uniform applied magnetic field generated by an electromagnet. (b) Calculated eigenfrequencies of magnetostatic modes with indices $\{l_m, m_m, q_m\}$, overlaid with dips from (a). This is used to identify the magnons excited by the microwave antenna. (c) Same as (a) but in non-uniform magnetic field of a permanent magnet showing normal mode splittings and additional magnons. (d) Same as (c), but with rutile coupling prism in place indicating the microwave modes of the prism alongside that of the YIG sphere.

pling constant G can be summarized as [2],

$$G \propto \delta_{q_i,q_o} \langle l_i, m_i; l_m, m_m | l_o, m_o \rangle . \tag{3.1}$$

This expression effectively captures the mode matching between the three modes. The first factor gives a radial selection rule, $q_i = q_o$. The second factor is the Clebsch-Gordan coefficient governing the angular momentum conservation.

For WGMs, $m_i \approx l_i$ and $m_o \approx l_o$, while for the magnons excited by microwaves, $l_m, m_m \sim 1 \ll l_i, l_o \sim 10^3$. Under such conditions, the optical interaction with the magnon occurs only in the thin band occupied by the WGMs near the equator. The long-wavelength nature of magnons therefore preserves the transverse field distribution of WGMs. This gives the radial selection rule above, and considering polar direction, that $l_o - m_o = l_i - m_i$. The wave-matching conditions in the azimuthal direction dictates $m_o = m_m + m_i$. This implies that G is approximately zero unless $l_o - l_i = m_m$, which is confirmed by explicit calculation of the Clebsch-Gordan coefficient. BLS scatters photons into the mode given by $\{l_i + m_m, m_i + m_m, q_i\}$ which is fixed by the incident WGM and the magnon.

For significant coupling we require a non-zero magnon density at the equator, where WGMs reside. From explicit solutions [8], the magnetostatic mode amplitudes vanish at equator for odd $l_m - m_m$ (see Fig. 3.1(b-i)).

Finally, we consider the energy conservation. The $l_o = l_i + 1$, $l_o = l_i$ and $l_o = l_i - 1$ transitions have frequencies of 7 GHz, 40 GHz, and 50 GHz, respectively, fixed by the optical cavity free spectral range and geometrical birefringence. The linewidth of the WGM of ≈ 1 GHz is much smaller than the frequency spacing between these transitions, ensuring the selectivity of the resonance condition. In our setup the maximum field is ≈ 300 mT, corresponding to a ferromagnetic resonance frequency ≈ 8.5 GHz. Hence, only the $l_o = l_i + 1$ transitions are observed [7]. Comparing this resonance condition to $l_o - l_i = m_m$ derived previously, we therefore have $m_m = 1$. The fact that $l_m - m_m$ must be even then restricts l_m to be an odd integer. While it is more difficult to couple microwaves to high l_m modes, increasing l_m typically increases the equatorial magnon density and hence, is likely to have higher optomagnonic coupling. We note that the equatorial magnon density also depends on q_m, but its discussion is beyond the scope of this work.

In summary, the magnons expected to be active for BLS should have $l_m = 1, 3, 5, \ldots$ and $m_m = 1$. Note that the sign of m_m in the allowed transitions is for the magnetic field direction shown in Fig. 3.2, such that the angular momentum of the WGMs is parallel to the static magnetization. Similar arguments show that for the opposite magnetic field (or WGM circulation direction), the expected magnons should have $l_m = 1, 3, 5, \ldots$ and $m_m = -1$. For opposite input polarization, energy conservation leads to preferential Stokes scattering, but the same selection rules apply.

3.3. Identification of magnetostatic modes

The microwave reflection coefficient $|S_{11}|$ of the loop antenna [9] is measured in the experimental setup shown in Fig. 3.2. Two complications hinder the labeling

of the magnetostatic mode spectra: (1) the inhomegeniety of the static magnetic field of the permanent magnet. (2) The rutile coupling prism is a good microwave dielectric resonator that interferes with the magnetic resonance. Therefore, we first carry out a simpler experiment by transferring the loop antenna with YIG sphere (without the prism) into a separate electromagnet with uniform static magnetic field. The results are summarized in Fig. 3.3(a). We follow Ref. [8] and plot the reduced frequency $(\omega - \omega_H)/\omega_M + 1/3$, where the Larmor frequency $\omega_H = \gamma\mu_0 H_0$ is subtracted so that the dispersion can be seen more clearly. Here, the gyromagnetic ratio $\gamma = 28\,\mathrm{GHz/T}$ and $\omega_M = \gamma\mu_0 M_{\mathrm{yig}}$, with $\mu_0 M_{\mathrm{yig}} = 180\,\mathrm{mT}$. We use the $\{110\}$ (Kittel) and $\{220\}$ modes as magnetic field sensors, aligning them to their expected position in reduced frequency. These can be identified by their frequency separation $\omega_M/15$, which is independent of magnetic field and depends only on the saturation magnetization. The rescaled map of the observed microwave reflection coefficient $|S_{11}|$ is shown in Fig. 3.3(a).

The positions of the resonances in Fig. 3.3(a) are plotted in Fig. 3.3(b), along with expected mode frequencies [8]. There is clear agreement with several sets of points indicating that several non-Kittel modes are driven by the loop antenna (highlighted by colored lines). If the drive field distribution of this antenna were uniform, only the Kittel mode would couple to the microwave line. However, non-uniformity in the drive field allows other magnetostatic modes to be driven as well.

To help identify the observed magnetostatic modes, we numerically calculated the magnon mode overlap with the drive field distribution of the loop antenna treated as a current loop. All the modes labeled in Fig. 3.3(a) have microwave coupling strength greater than 0.1% of the Kittel mode, apart from the $\{521\}$ and $\{210\}$ modes which are much weaker in the model. For example, the relative microwave coupling strength for the $\{200\}$ mode is estimated to be ≈4%.

Next, we transfer the YIG sphere and microwave antenna to the optical setup (with rutile prism removed) in which the static magnetic field is generated by a small permanent magnet since there is no room for an electromagnet. The differences between the measured $|S_{11}|$ in Fig. 3.3(c) and (a) are caused by the inhomogeneous dc magnetic field. We again use the $\{110\}$ and $\{220\}$ modes as sensors for the magnetic field distribution, which can be estimated by analytical expressions for a cuboid magnet [10].

The non-uniformity of the static magnetic field leads to microwave absorption of additional modes and normal mode splitting at degeneracies, in particular between $\{110\}$ and $\{200\}$. Nevertheless, the modes identified in Fig. 3.3(b) are easily recognized and labeled by the colored arrows. At higher magnetic fields, corresponding to the YIG sphere being closer to the permanent magnet, the increasing non-uniformity of the magnetic field further distorts the spectra.

Finally, we put the rutile coupling prism in place next to the YIG sphere. The prism is a good microwave dielectric resonator, so that the spectra in Fig. 3.3(c) are affected by a large number of additional spurious resonances. These do not depend on the magnetic field and have a negative slope since the Larmor frequency has been subtracted. Despite this, the magnetostatic modes can still be clearly identified.

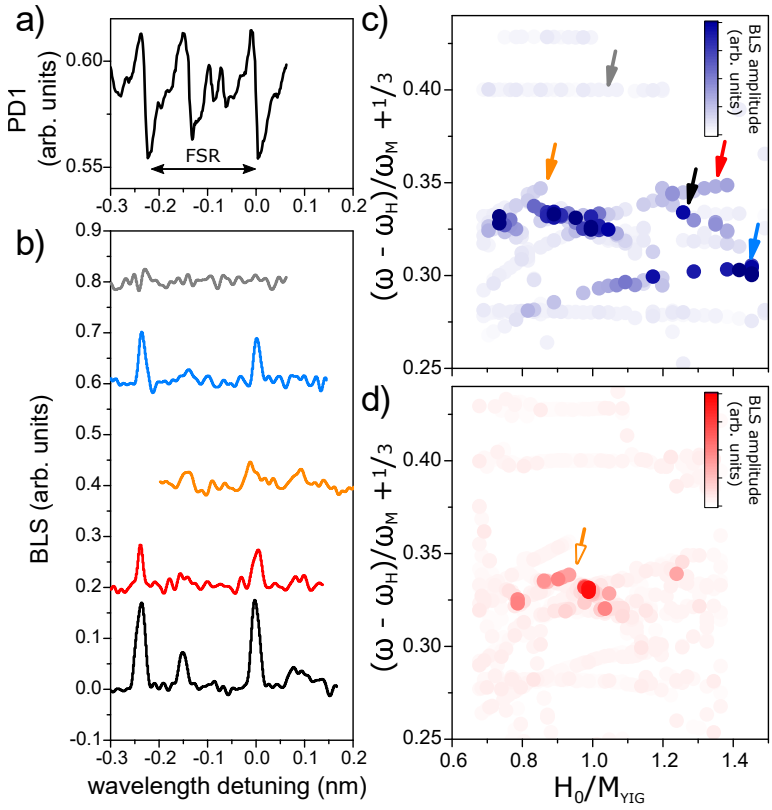

Figure 3.4: Optical measurements of BLS efficiency. (a) The reflected input optical power at photodiode I as a function of input laser wavelength detects the WGM resonances. The laser detuning (x-axis) is measured relative to one of the WGMs. Resonances corresponding to mode families $q = 1, 2$ are observed. The free spectral range for modes with $q = 1$ is indicated. (b) BLS signal as a function of input laser wavelength for several magnons marked by arrows in (c) with matching color. (c) BLS intensity maxima of the $q = 1$ WGM resonance (coded by color intensity) for each measured point of microwave frequency (y-axis, reduced frequency) and magnetic field (x-axis). (d) Same as (c), but with static magnetic field inverted.

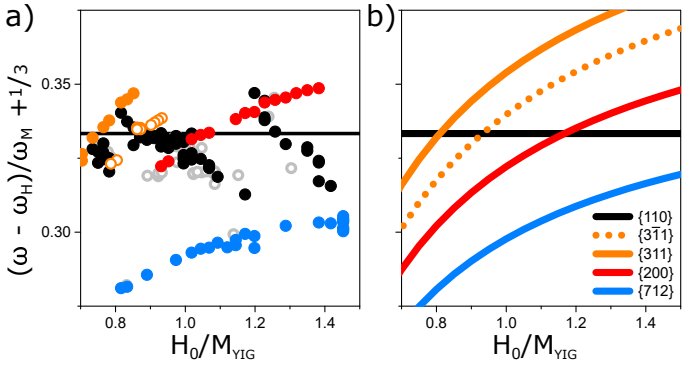

Figure 3.5: Indentification of BLS active magnetostatic modes. (a) Data points corresponding to those in Fig. 3.4(c) which are above a threshold set by the noise floor. The dot colors correspond to the assigned magnetostatic mode. Positive and negative magnetic fields are indicated by filled and open points, respectively. Points where mode identification is unclear are marked in gray. (b) Theoretical dispersion of the modes observed in (a).

3.4. Brillouin light scattering

Having identified the magnons that couple to the microwave antenna, we now discuss the optical measurements. We identify WGM resonances by varying the wavelength of the input light and measuring the reflected output in photodiode I, as shown in Fig. 3.4(a). Dips are seen for the $q = 1$ mode family as well as a smaller peak for the $q = 2$ mode family [7], where q is the radial index of WGM defined above.

We apply a microwave drive at several of the magnetostatic mode frequencies identified in Fig. 3.3(c) and look for BLS. The polarization scattered light is spectrally resolved using a Fabry-Pérot etalon to identify the anti-Stokes BLS and measured on photodiode II. For each microwave resonance we sweep the input laser wavelength, some of the spectra are plotted in Fig. 3.4(b). The peaks indicate enhanced BLS when the drive laser is resonant with a WGM.

A fit to the BLS peaks corresponding to the $q = 1$ mode is used to extract the maximum BLS for each FMR frequency. The results are plotted as a function of reduced frequency and positive and negative magnetic field in Fig. 3.4(c) and Fig. 3.4(d), respectively. In addition to the Kittel mode, several magnetostatic modes also generate BLS above the noise level.

We take the data from Fig. 3.4(c,d) and set a suitable noise-level threshold determined from a histogram of the measurement points. The measurement points with BLS above this threshold are plotted in Fig. 3.5(a). Closed (open) circles indicate measurements at positive (negative) magnetic field. Using their dispersion from Fig. 3.3, we identify the magnetostatic mode associated with each of the points. The relevant calculated magnetostatic mode frequency dispersion are plotted for comparison in Fig. 3.5(b). For some points with negative field, mode identification has not been possible (gray points) due to the proximity of the overwhelming signal of the Kittel mode.

3.5. Comparison with theory

We are now in a position to compare the observed mode frequencies with the model calculations. In Sec. 3.2, we concluded that BLS should be observed for magnetostatic modes with odd l_m and $m_m = +1(-1)$ for positive (negative) magnetic field, respectively. In addition to the Kittel mode $\{110\}$, we observe the $\{311\}$ mode and, in the opposite field direction, the $\{3\bar{1}1\}$ mode, as expected. Additionally, we observe a signal for the $\{712\}$ mode. We do not observe BLS for the $\{220\}$, $\{330\}$, $\{320\}$ and several other magnetostatic modes identified in the microwave measurements, all conforming to the selection rules derived above.

On the other hand, the BLS by the $\{200\}$ mode contradicts the model predictions. This is likely caused by the non-uniformity of the applied magnetic field discussed in Sec. 3.3. The $m = 0$ modes are particularly sensitive to inhomogeneities that break axial symmetry, as they are identical with spin-waves in the bulk material [11]. In theory, all that is required to allow BLS would be a small lateral shift in the $\{200\}$ mode function with respect to the center of the sphere. This is plausible given the magnetic field inhomogeneity. The axial symmetry breaking also allows resonant coupling to the 110 mode [11], which is evidenced in our microwave experiments as a normal mode splitting between the $\{200\}$ and $\{110\}$ modes (cf. Fig. 3.3(c) and Fig. 3.3(a)). Note that the BLS scattering from the 200 mode is still observed far from the anticrossing, indicating that this effect is not simply due to resonant admixing of the two mode functions (see Fig. 4(c)). While the non-uniformity of the magnetic field complicates the interpretation, it does indicate that BLS by magnetostatic modes can be tailored by the application of controlled non-uniform magnetic fields.

For the $\{712\}$ mode, we measure similar BLS strength to the $\{110\}$ (see Fig. 3.4(b)). However, the microwave coupling to the $\{712\}$ is much weaker than that to the $\{110\}$. This can be seen from the fact that the ratio of the observed depth of the microwave resonances $\approx 1/8$ (see Fig. 3.3(c)), while the internal Q-factors are approximately equal [1]. Thus, the optomagnonic coupling must be stronger, in order that the BLS is comparable. This is consistent with calculations that show that the optomagnonic coupling for the $\{712\}$ mode is 3–4 times larger than for the $\{110\}$ mode.

3.6. Conclusions

In conclusion, we have measured cavity enhanced BLS from magnetostatic modes other than the uniform Kittel mode. We find reasonable agreement with the recently determined selection rules based on the axial rotational symmetry of the system [2]. If microwave coupling to higher order modes can be optimized, the stronger optomagnonic coupling strength could be exploited. This offers a possible route to achieving larger microwave-to-optical conversion efficiency.

[1] Note that the loaded Q-factor of the $\{110\}$ mode is significantly lower due to strong radiative damping via the antenna.

References

[1] J. A. Haigh, N. J. Lambert, S. Sharma, Y. M. Blanter, G. E. W. Bauer, and A. J. Ramsay, *Selection rules for cavity-enhanced brillouin light scattering from magnetostatic modes,* Phys. Rev. B **97**, 214423 (2018).

[2] S. Sharma, Y. M. Blanter, and G. E. W. Bauer, *Light scattering by magnons in whispering gallery mode cavities,* Phys. Rev. B **96**, 094412 (2017).

[3] M. Goryachev, W. G. Farr, D. L. Creedon, Y. Fan, M. Kostylev, and M. E. Tobar, *High-Cooperativity Cavity QED with Magnons at Microwave Frequencies,* Phys. Rev. Applied **2**, 054002 (2014).

[4] N. J. Lambert, J. A. Haigh, and A. J. Ferguson, *Identification of spin wave modes in yttrium iron garnet strongly coupled to a co-axial cavity,* J. Appl. Phys. **117**, 053910 (2015).

[5] A. D. Karenowska, A. F. v. Loo, R. G. E. Morris, and S. Kosen, *Strong coupling of magnons in a YIG sphere to photons in a planar superconducting resonator in the quantum limit,* Sci. Rep. **7**, 11511 (2017).

[6] J. A. Haigh, S. Langenfeld, N. J. Lambert, J. J. Baumberg, A. J. Ramsay, A. Nunnenkamp, and A. J. Ferguson, *Magneto-optical coupling in whispering-gallery-mode resonators,* Phys. Rev. A **92**, 063845 (2015).

[7] J. A. Haigh, A. Nunnenkamp, A. J. Ramsay, and A. J. Ferguson, *Triple-resonant brillouin light scattering in magneto-optical cavities,* Phys. Rev. Lett. **117**, 133602 (2016).

[8] P. C. Fletcher and R. O. Bell, *Ferrimagnetic resonance modes in spheres,* Journal of Applied Physics **30**, 687 (1959), https://doi.org/10.1063/1.1735216 .

[9] S. Klingler, H. Maier-Flaig, C. Dubs, O. Surzhenko, R. Gross, H. Huebl, S. T. B. Goennenwein, and M. Weiler, *Gilbert damping of magnetostatic modes in a yttrium iron garnet sphere,* Appl. Phys. Lett. **110**, 092409 (2017).

[10] R. Engel-Herbert and T. Hesjedal, *Calculation of the magnetic stray field of a uniaxial magnetic domain,* J. Appl. Phys. **97**, 074504 (2005).

[11] P. Röschmann and H. Dötsch, *Properties of Magnetostatic Modes in Ferrimagnetic Spheroids,* Phys. Stat. Sol. (b) **82**, 11 (1977).

4

Optical cooling of magnons

This chapter has been published as S. Sharma, Y.M. Blanter, G.E.W. Bauer Phys. Rev. Lett. **121**, 087205 (2018) [1].

A great achievement of modern physics is the Doppler cooling of trapped atoms by optical lasers [2, 3] down to temperatures of micro-Kelvin [4]. Subsequently, even macroscopic mechanical objects, such as membranes and cantilevers, have been cooled to their quantum mechanical ground state [5–9] by blue shifting the stimulated emission using an optical cavity [5, 6]. 'Cavity optomechanics' is a vibrant field that achieved successful Heisenberg uncertainty-limited mechanical measurements, the generation of entangled light-mechanical states, and ultra-sensitive gravitational wave detection [9]. An optical cryocooler based on solid state samples [10] can be superior due to its compactness and lack of moving components [11]. Optical cooling has been demonstrated for glass [10, 12] and envisioned for semiconductors [11, 13, 14].

Motivated by the potential of a ferromagnet as a versatile quantum interface at low temperatures, we discuss here the potential of optical cooling of magnons. As discussed in Chs. 2 and 3, the red and blue sidebands in BLS via magnons are not of the same height. When more photons are scattered into the blue sideband, light effectively extracts energy from the magnons and in principle cools them. Here, we predict that modern technology and materials can significantly reduce the temperature of the magnetic order, showing the potential to manipulate magnons using light.

We derive below rate equations for photons and magnons to estimate the steady-state magnon number that can be reached as a function of material and device parameters. We consider a spherical magnetic insulator with high index of refraction that is transparent at the input light frequency (Fig. 4.1) and magnetization perpendicular to the WGM orbits that are excited by proximity coupling to an external laser. We single out two groups of magnon modes that couple preferentially to the WGMs [15]. The small angular momentum (including the Kittel) magnons, M_S in Fig. 4.1, and large angular momentum magnons, the chiral Damon-Eshbach (DE) modes M_L. The theory presented below is valid for both types of magnons.

4.1. Steady state number of magnons

We can understand the basic physics by the minimal model sketched in Fig. 4.2. We focus on a single incident WGM W_p with index p (stands for pump) and frequency ω_p. It is occupied by [9]

$$n_p = \frac{4K_p}{(\kappa_p + K_p)^2} \frac{P_{\text{in}}}{\hbar\omega_p} \tag{4.1}$$

photons, with κ_p being the intrinsic linewidth, K_p the leakage rate into the proximity coupler, and P_{in} the input light power. An optically active magnon M [with either small or large angular momentum] is annihilated $W_p + M \rightarrow W_c$ or created $W_p \rightarrow W_h + M$ by BLS, where W_c (cold) and W_h (hot) are blue and red-shifted sideband WGMs, respectively.

We first derive a simple semi-classical rate equation for the non-equilibrium steady-state magnon number, $n_m^{(sc)}$ [the superscript distinguishes the estimate from n_m as more rigorously derived below]. The thermal bath absorbs and injects magnons at rates $\kappa_m n_m^{(sc)} (n_{\text{th}} + 1)$ and $\kappa_m n_{\text{th}} \left(n_m^{(sc)} + 1\right)$ respectively, where κ_m

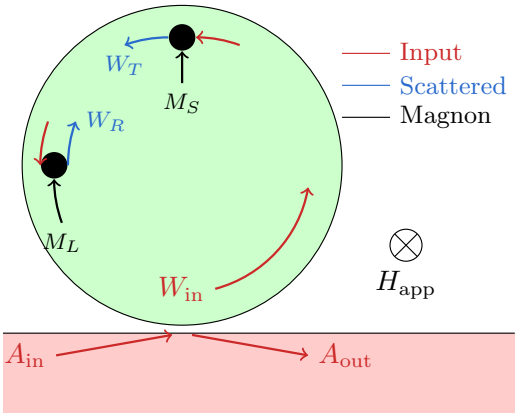

Figure 4.1: Optomagnonic cooling setup: A ferromagnetic sphere in contact with an optical waveguide. A magnetic field H_{app} (into the paper) is applied to saturate the magnetization. Input light with amplitude A_{in} is evanescently coupled to a WGM W_{in}. We focus on anti-Stokes scattering by two types of magnons that are characterized by their angular momentum [15]. A small angular momentum magnon M_S maintains the direction of WGMs, converting W_{in} to W_T. W_{in} can be reflected into W_R by absorbing a large angular momentum magnon M_L. Theoretically, both the cases can be treated in the same formalism. The input WGM is labelled by (pump) p and T or R by (cool) c.

is the inverse magnon lifetime and n_{th} is the occupation of the bath at magnon frequency ω_m. At an ambient temperature T,

$$n_{\text{th}} = \left[\exp\left(\frac{\hbar\omega_m}{k_B T}\right) - 1\right]^{-1}. \tag{4.2}$$

The optical cooling rate is $R_c^0 n_p n_m^{(sc)}$, where R_c^0 is the anti-Stokes scattering rate of one W_p-photon by one M-magnon and we assumed that there are no photons in W_c. The latter is justified because of small optomagnonic couplings compared to WGM dissipation rates, $\sim 2\pi \times 0.1 - 1$ GHz [16–18] while $R_c^0 n_p n_m^{(sc)}$ is at most $\sim \kappa_m \sim 2\pi \times 1$ MHz. In the absence of dissipation, Fermi's golden rule gives $R_c^0 = 2\pi |g_c|^2 \delta(\omega_p + \omega_m - \omega_c)$, where $\hbar g_c$ is the optomagnonic coupling and $\{\omega_p, \omega_c, \omega_m\}$ are the frequencies of $\{W_p, W_c, M\}$, respectively. When W_c has a finite lifetime, the δ-function is broadened into a Lorentzian, giving

$$R_c^0 = \frac{|g_c|^2 (\kappa_c + K_c)}{\left(\omega_p + \omega_m - \omega_c\right)^2 + (\kappa_c + K_c)^2/4}, \tag{4.3}$$

where κ_c is its intrinsic linewidth, and K_c is its leakage rate into the proximity coupler. Similarly, the optical heating rate is $R_h^0 n_p \left(n_m^{(sc)} + 1\right)$, where R_h^0 is given by Eq. (4.3) with $g_c, \omega_c, \kappa_c \to g_h, \omega_h, \kappa_h$ and $\omega_m \to -\omega_m$. In deriving $R_{c,h}^0$, we ignore the magnon linewidth since $\kappa_m \ll \kappa_c, \kappa_h$ [15, 16]. In the steady state the cooling and heating

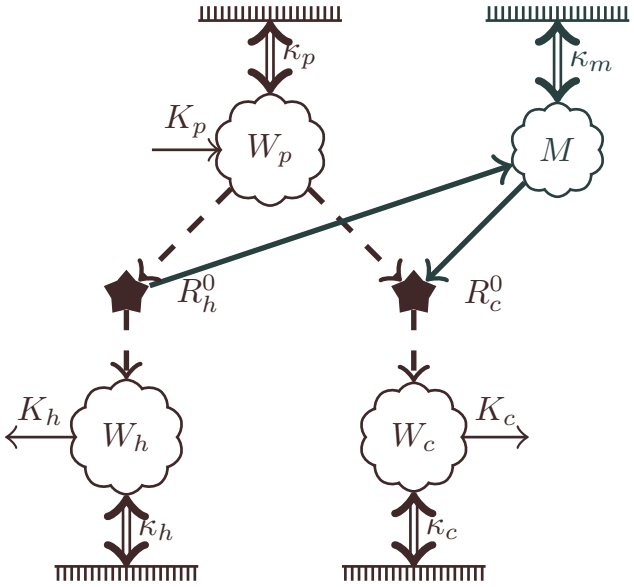

Figure 4.2: Light-induced cooling of a magnon, M. A proximity fiber or prism is coupled to the WGMs W_x with a coupling constant κ_x, exciting W_p while collecting the scattered W_c and W_h. The photons are inelastically scattered by the magnon $W_p + M \to W_c$ and $W_p \to W_h + M$ at single particle rates R_c^0 and R_h^0 respectively, derived in the text. All modes are coupled to their respective thermal baths by leakage rates κ_x. When κ_c is much larger than the corresponding scattering rate, the bath associated with W_c can become an efficient channel for dissipation of the magnons in M.

rates are equal, leading to the estimate

$$n_m^{(sc)} = \frac{\kappa_m n_{\mathrm{th}} + R_h^0 n_p}{\kappa_m + \left(R_c^0 - R_h^0\right) n_p}. \tag{4.4}$$

This agrees with the result from the more precise theory discussed below, thus capturing the essential processes correctly (a posteriori). However, the rate equation cannot access noise properties beyond the magnon number that are important for thermodynamic applications. Further, it does not differentiate between a coherent precession of the magnetization and the thermal magnon cloud with the same number of magnons.

4.2. Equation of motion

In order to model the cooling process more rigorously, we proceed from a model Hamiltonian for a system with three photon and one magnon modes. In the Hamiltonian $\hat{H}_S = \hat{H}_0 + \hat{H}_{\mathrm{om}}$ [15]

$$\hat{H}_0 = \hbar\omega_p \hat{a}_p^\dagger \hat{a}_p + \hbar\omega_c \hat{a}_c^\dagger \hat{a}_c + \hbar\omega_h \hat{a}_h^\dagger \hat{a}_h + \hbar\omega_m \hat{m}^\dagger \hat{m}, \tag{4.5}$$

and $\hat{a}_x$ and $\hat{m}$ are the annihilation operators for photon W_x with $x \in \{p, c, h\}$ and magnon M. The optomagnonic coupling in the rotating wave approximation reads

[15]

$$\hat{H}_{\mathrm{om}} = \hbar g_c \hat{a}_p \hat{a}_c^\dagger \hat{m} + \hbar g_h \hat{a}_p \hat{a}_h^\dagger \hat{m}^\dagger + \mathrm{h.c.}, \tag{4.6}$$

where g_c and g_h are the scattering amplitudes and h.c. is the Hermitian conjugate.

In the rotating frame of the "envelope" operators $\hat{W}_x(t) \triangleq \hat{a}_x(t)e^{i\omega_x t}$ and $\hat{M}(t) \triangleq \hat{m}(t)e^{i\omega_m t}$ the (Heisenberg) equation of motion for $\hat{M}$ becomes [5, 19]

$$\frac{d\hat{M}}{dt} = -ig_h \hat{W}_p \hat{W}_h^\dagger e^{i\delta_h t} - ig_c^* \hat{W}_p^\dagger \hat{W}_c e^{-i\delta_c t} - \frac{\kappa_m}{2}\hat{M} - \sqrt{\kappa_m}\hat{b}_m, \tag{4.7}$$

where $\delta_h = \omega_h + \omega_m - \omega_p$ and $\delta_c = \omega_c - \omega_m - \omega_p$ are the detunings from the scattering resonances. $\hat{b}_m(t)$ is the stochastic magnetic field generated by the interaction of M with phonons [20] and/or other magnons [21], whose precise form depends on the microscopic details of the interaction [22].

We assume that the correlators of $\hat{b}_m$ obey the fluctuation-dissipation theorem for thermal equilibrium [23, 24]. When $\kappa_m \ll k_B T/\hbar$, which is satisfied for $\kappa_m \sim 2\pi \times 1$ MHz [16–18] and $T \gg 50\mu$K, the (narrow band filtered) noise is effectively white and generates a canonical Gibbs distribution of the magnons in steady state [19]. Their statistics are $\langle \hat{b}_m(t) \rangle = 0$, $\left\langle \hat{b}_m^\dagger(t')\hat{b}_m(t) \right\rangle = n_{\mathrm{th}}\delta(t-t')$ and $\left\langle \hat{b}_m(t')\hat{b}_m^\dagger(t) \right\rangle = (n_{\mathrm{th}}+1)\delta(t-t')$, where n_{th} is defined in Eq. (4.2).

For weak scattering relative to the input power, we can ignore any back-action on W_p such that its dynamics is governed only by the proximity coupling. When W_p is in a coherent state, $\langle \hat{W}_p(t) \rangle = \sqrt{n_p}$ and $\left\langle \hat{W}_p^\dagger(t')\hat{W}_p(t) \right\rangle = n_p$, where n_p is given by Eq. (4.1).

The photons in W_c are generated by $\hat{H}_{\mathrm{om}}$ and dissipated into their thermal bath, with Heisenberg equation of motion [5, 19]

$$\frac{d\hat{W}_c}{dt} = -ig_c \hat{W}_p \hat{M} e^{i\delta_c t} - \frac{\kappa_c + K_c}{2}\hat{W}_c - \sqrt{\kappa_c}\hat{b}_c - \sqrt{K_c}\hat{A}_c, \tag{4.8}$$

where $\hat{b}_c$ and $\hat{A}_c$ are noise operators. The physical origins of $\hat{b}_c$ and finite lifetime κ_c^{-1} are scattering by impurities, surface roughness, and lattice vibrations. K_c is the leakage rate of W_c into the proximity coupler and $\hat{A}_c$ is the vacuum noise from the latter into W_c. The noise sources are white for sufficiently small κ_c. $\langle \hat{X}_c(t) \rangle = 0$, $\left\langle \hat{X}_c^\dagger(t')\hat{X}_c(t) \right\rangle = 0$ and $\left\langle \hat{X}_c(t')\hat{X}_c^\dagger(t) \right\rangle = \delta(t-t')$ where $X \in \{\hat{b}_c, \hat{A}_c\}$, because the thermal occupation of photons at infrared and visible frequencies is negligibly small at room temperature $e^{-\hbar\omega_c/(k_B T)} \approx 0$.

The solution to Eq. (4.8) is $\hat{W}_c(t) = \hat{W}_{c,\mathrm{th}}(t) + \hat{W}_{c,\mathrm{om}}(t)$. The thermal contribution is,

$$\hat{W}_{c,\mathrm{th}} = \int_0^t e^{-(\kappa_c+K_c)(t-\tau)/2}\left[-\sqrt{\kappa_c}\hat{b}_c(\tau) - \sqrt{K_c}\hat{A}_c(\tau)\right]d\tau \tag{4.9}$$

where the origin of time is arbitrary. For $t, t' \to \infty$, we get the equilibrium statistics

$\left\langle \hat{W}^{\dagger}_{c,\mathrm{th}}(t')\hat{W}_{c,\mathrm{th}}(t)\right\rangle = 0$ and

$$\left\langle \hat{W}_{c,\mathrm{th}}(t')\hat{W}^{\dagger}_{c,\mathrm{th}}(t)\right\rangle = \exp\left[-\frac{(\kappa_c + K_c)|t-t'|}{2}\right], \tag{4.10}$$

independent of the optomagnonic coupling. $\hat{W}_{c,\mathrm{om}}$ can be simplified by the adiabaticity of the magnetization dynamics that follows from $\kappa_m \ll \kappa_c$. When $\hat{M}$ is treated as a slowly varying constant

$$\hat{W}_{c,\mathrm{om}}(t) \approx -ig_c\hat{M}(t)\int_0^t e^{-(\kappa_c+K_c)(t-\tau)/2}\hat{W}_p(\tau)e^{i\delta_c\tau}d\tau. \tag{4.11}$$

$\hat{W}_h(t)$ is obtained by the substitution $c \to h$ and $\hat{M} \to \hat{M}^{\dagger}$ in Eqs. (4.9-4.11).

We can now rewrite Eq. (4.7) as

$$\frac{d\hat{M}}{dt} = -\left(\frac{\kappa_m}{2}\hat{M} + \sqrt{\kappa_m}\hat{b}_m\right) + \hat{O}_c + \hat{O}_h. \tag{4.12}$$

with cooling and heating operators that reflect the light scattering processes in Fig. 4.2:

$$\hat{O}_c = \hat{\mathcal{N}}_c + i\hat{\Sigma}_c\hat{M}, \tag{4.13}$$

$$\hat{O}_h = -\hat{\mathcal{N}}^{\dagger}_h + i\hat{\Sigma}^{\dagger}_h\hat{M}. \tag{4.14}$$

Focusing on the cooling process, we distinguish the self-energy,

$$\hat{\Sigma}_c = i|g_c|^2\int_0^t e^{(i\delta_c+(\kappa_c+K_c)/2)(\tau-t)}\hat{W}^{\dagger}_p(t)\hat{W}_p(\tau)d\tau, \tag{4.15}$$

from the noise operator,

$$\hat{\mathcal{N}}_c(t) = -ig^*_c\hat{W}^{\dagger}_p(t)\hat{W}_{c,\mathrm{th}}(t)e^{-i\delta_c t}. \tag{4.16}$$

In the weak-coupling regime we may adopt a mean-field approximation by replacing $\hat{\Sigma}_c$ by its average,

$$\left\langle\hat{\Sigma}_c\right\rangle = -\bar{\omega}_c + i\frac{\bar{\kappa}_c}{2} \triangleq \frac{|g_c|^2 n_p}{\delta_c - i(\kappa_c + K_c)/2}, \tag{4.17}$$

where $\bar{\omega}_c$ is the (reactive) shift of the magnon resonance and $\bar{\kappa}_c$ the optical contribution to the magnon linewidth.

The noise $\hat{\mathcal{N}}_c$ can be interpreted as the vacuum fluctuations of W_c entering the magnon subsystem via the optomagnonic interaction. $\hat{\mathcal{N}}_c$ has a very short correlation time $\sim (\kappa_c + K_c)^{-1}$ [see Eq. (4.10)] compared to magnon dynamics $\sim \kappa_m^{-1}$, and thus can be treated as a white noise source with $\left\langle\hat{\mathcal{N}}_c(t)\right\rangle = 0$, $\left\langle\hat{\mathcal{N}}^{\dagger}_c(t)\hat{\mathcal{N}}_c(t')\right\rangle = 0$,

and $\left\langle \hat{\mathcal{N}}_c(t')\hat{\mathcal{N}}_c^\dagger(t)\right\rangle \approx V_c\delta(t-t')$. By integrating over time and using the correlation functions of $\hat{W}_p$ and $\hat{W}_{c,\mathrm{th}}$

$$V_c = \frac{4|g_c|^2 n_p(\kappa_c + K_c)}{4\delta_c^2 + (\kappa_c + K_c)^2} = \bar{\kappa}_c, \tag{4.18}$$

defined in Eq. (4.17). $\bar{\kappa}_c/\kappa_m$ at resonance $\delta_c = 0$ is the cooperativity between the magnons and W_c-photons due to the coupling mediated by W_p-photons.

Analogous results hold for $\hat{O}_h$, with substitutions $c \to h$ in Eqs. (4.15)-(4.18). We arrive at

$$\frac{d\hat{M}}{dt} \approx -i(\bar{\omega}_c + \bar{\omega}_h)\hat{M} - \frac{\kappa_{\mathrm{tot}}}{2}\hat{M} - \sqrt{\kappa_{\mathrm{tot}}}\hat{b}_{\mathrm{tot}}, \tag{4.19}$$

where $\kappa_{\mathrm{tot}} = \kappa_m + \bar{\kappa}_c - \bar{\kappa}_h$ and $\sqrt{\kappa_{\mathrm{tot}}}\hat{b}_{\mathrm{tot}} = \sqrt{\kappa_m}\hat{b}_m - \hat{\mathcal{N}}_c + \hat{\mathcal{N}}_h^\dagger$. The fluctuations of the total noise follow from Eq. (4.18)

$$\left\langle \hat{b}_{\mathrm{tot}}^\dagger(t')\,\hat{b}_{\mathrm{tot}}(t)\right\rangle \approx n_m\,\delta(t-t'), \tag{4.20}$$

$$\left\langle \hat{b}_{\mathrm{tot}}(t')\,\hat{b}_{\mathrm{tot}}^\dagger(t)\right\rangle \approx (n_m+1)\,\delta(t-t'), \tag{4.21}$$

where

$$n_m = \frac{\kappa_m n_{\mathrm{th}} + \bar{\kappa}_h}{\kappa_m + \bar{\kappa}_c - \bar{\kappa}_h}. \tag{4.22}$$

4.3. Results

Eq. (4.19) is equivalent to the equation of motion for magnons in equilibrium after the substitutions $\omega_m \to \omega_m + \bar{\omega}_c + \bar{\omega}_h$, $\kappa_m \to \kappa_{\mathrm{tot}}$, and $n_{\mathrm{th}} \to n_m$. It implies that the magnons in the non-equilibrium steady state are still canonically distributed with density matrix

$$\hat{\rho}_{ne} = \exp\left(\frac{-\hbar\omega_m\hat{n}_m}{k_B T_{ne}}\right)\left(\mathrm{Tr}\left[\exp\left(\frac{-\hbar\omega_m\hat{n}_m}{k_B T_{ne}}\right)\right]\right)^{-1} \tag{4.23}$$

where the number operator $\hat{n}_m = \hat{m}^\dagger\hat{m}$ and the non-equilibrium magnon temperature T_{ne} is implicitly defined by Eq. (4.22) and

$$n_m = \left[\exp\left(\frac{\hbar\omega_m}{k_B T_{ne}}\right) - 1\right]^{-1}. \tag{4.24}$$

We get $\langle\hat{M}_x\rangle = \langle\hat{M}_y\rangle = 0$, which implies that light scattering does not induce a coherent magnon precession, in contrast to a resonant ac magnetic field. n_m is the average number of magnons that can be larger or smaller than the equilibrium value n_{th}. The result is consistent with $n_m^{(sc)}$ [see Eq. (4.4)] because $\bar{\kappa}_{c,h} = R^0_{c,h}n_p$ as expected from Fermi's golden rule. The canonical distribution implies that the steady-state magnon entropy is maximized for the given number of magnons, n_m.

When $\bar{\kappa}_h - \bar{\kappa}_c > \kappa_m$, i.e. when heating by the laser overcomes the intrinsic magnon damping, the system becomes unstable, leading to runaway magnon generation and self-oscillations [25–27]. The instability is regularized by magnon-magnon scattering, not included in our theory.

Here we focus on the cooling scenario in which $\bar{\kappa}_h \ll \bar{\kappa}_c$ [15]. Magnon cooling can be monitored by the intensity of the blue-shifted sideband. Using the input-output formalism [19, 28] the scattered light amplitude in the rotating frame is

$$\hat{A}_{\text{out}}(t) = -\sqrt{K_c}\hat{W}_c(t). \tag{4.25}$$

It can be converted into the output power by $P_{\text{out}} = \hbar\omega_c \left\langle \hat{A}^\dagger_{\text{out}}(t)\hat{A}_{\text{out}}(t) \right\rangle$, which is independent of time in steady state. With impedance matching, $\kappa_{p,c} = K_{p,c}$, and at the triple resonance, $\delta_c = 0$,

$$\frac{P_{\text{out}}}{P_{\text{in}}} = \frac{|g_c|^2}{\kappa_c\kappa_p}\frac{\kappa_m n_{\text{th}}}{\kappa_m + 2|g_c|^2 n_p/\kappa_c} \propto \frac{1}{1 + P_{\text{in}}/P_s}, \tag{4.26}$$

defining the saturation power

$$P_s \triangleq \frac{\hbar\omega_p\kappa_p\kappa_c\kappa_m}{2|g_c|^2}. \tag{4.27}$$

To leading order $P_{\text{out}} \propto P_{\text{in}}$ [15, 18], but saturates when the magnon number becomes small, which is an experimental evidence for magnon cooling. P_s is the input power that halves the number of magnons.

Eq. (4.23) is the reduced density matrix of a single magnon mode, M. At long wavelengths and small magnon numbers, the magnon-magnon interactions may be disregarded, so each magnon mode can be treated independently. The total $\hat{\rho}$ is a direct product of the reduced density matrices of the form (4.23), where ω_m and T_{ne} depend on the mode index.

For a YIG sphere with parameters $\omega_c \approx \omega_p = 2\pi \times 300\,\text{THz}$ (free space wavelength $1\mu\text{m}$), an optical Q-factor $\omega_p/(2\kappa_p) = \omega_c/(2\kappa_c) = 10^6$, [18], magnon linewidth $\kappa_m = 2\pi \times 1\,\text{MHz}$, and optomagnonic coupling $g_c = 2\pi \times 10\,\text{Hz}$ [15], we get $P_s = 140\,\text{W}$. Trying to match this with P_{in} is not useful since laser-induced lattice heating [11] will overwhelm the cooling effect. However, P_s can be significantly reduced by large magnon-photon coupling. Doping YIG with bismuth can increase g_c tenfold [29], bringing P_s down to $\sim 1\,\text{W}$. The spatial overlap between the magnons and photons [15] can be engineered in ellipsoidal or nanostructured magnets [30] which can increase g_c further by an order of magnitude, giving $P_s \sim 10\text{mW}$. For an ambient temperature $T = 1\,\text{K}$ and magnon frequency $\omega_m = 2\pi \times 10\,\text{GHz}$, the thermal magnon number $n_{\text{th}} = 1.62$. For $P_{\text{in}} = \{P_s/20,\, P_s,\, 5P_s\}$ the steady-state magnon numbers are $n_m = \{1.55,\, 0.81,\, 0.27\}$ and temperatures $T_{ne} = \{0.96,\, 0.60,\, 0.31\}\,\text{K}$ respectively. At an optimistic $P_s = 10\text{mW}$, the above input power corresponds to $n_p = \{3 \times 10^6,\, 5 \times 10^7,\, 3 \times 10^8\}$ intra-cavity photons respectively. Cooling is experimentally observable for relatively small powers $P_{\text{in}} < P_s/20$, which should be achievable by optimizing the magnon-photon coupling.

4.4. Summary

In summary, we estimate the cooling power due to BLS of light by magnons in an optomagnonic cavity. Due to the large mismatch of optical and magnonic time scales, the photon degree of freedom can be eliminated by renormalizing the magnon frequency and damping, cf. Eq. (4.19), and a light-controlled effective temperature Eq. (4.22). Current technology and materials are close to achieving significant cooling of magnons, envisioning the possibility of light-controlled magnon manipulation.

References

[1] S. Sharma, Y. M. Blanter, and G. E. W. Bauer, *Optical cooling of magnons,* Phys. Rev. Lett. **121**, 087205 (2018).

[2] T. Hänsch and A. Schawlow, *Cooling of gases by laser radiation,* Optics Communications **13**, 68 (1975).

[3] W. D. Phillips, *Nobel lecture: Laser cooling and trapping of neutral atoms,* Rev. Mod. Phys. **70**, 721 (1998).

[4] P. D. Lett, R. N. Watts, C. I. Westbrook, W. D. Phillips, P. L. Gould, and H. J. Metcalf, *Observation of atoms laser cooled below the doppler limit,* Phys. Rev. Lett. **61**, 169 (1988).

[5] F. Marquardt, J. P. Chen, A. A. Clerk, and S. M. Girvin, *Quantum theory of cavity-assisted sideband cooling of mechanical motion,* Phys. Rev. Lett. **99**, 093902 (2007).

[6] I. Wilson-Rae, N. Nooshi, W. Zwerger, and T. J. Kippenberg, *Theory of ground state cooling of a mechanical oscillator using dynamical backaction,* Phys. Rev. Lett. **99**, 093901 (2007).

[7] A. D. O'Connell, M. Hofheinz, M. Ansmann, R. C. Bialczak, M. Lenander, E. Lucero, M. Neeley, D. Sank, H. Wang, M. Weides, J. Wenner, J. M. Martinis, and A. N. Cleland, *Quantum ground state and single-phonon control of a mechanical resonator,* Nature **464**, 697 (2010).

[8] J. Chan, T. P. M. Alegre, A. H. Safavi-Naeini, J. T. Hill, A. Krause, S. Groblacher, M. Aspelmeyer, and O. Painter, *Laser cooling of a nanomechanical oscillator into its quantum ground state,* Nature **478**, 89 (2011).

[9] M. Aspelmeyer, T. J. Kippenberg, and F. Marquardt, *Cavity optomechanics,* Rev. Mod. Phys. **86**, 1391 (2014).

[10] B. C. Edwards, J. E. Anderson, R. I. Epstein, G. L. Mills, and A. J. Mord, *Demonstration of a solid-state optical cooler: An approach to cryogenic refrigeration,* Journal of Applied Physics **86**, 6489 (1999).

[11] M. Sheik-Bahae and R. Epstein, *Laser cooling of solids,* Laser & Photonics Reviews **3**, 67 (2009).

[12] R. I. Epstein, M. I. Buchwald, B. C. Edwards, T. R. Gosnell, and C. E. Mungan, *Observation of laser-induced fluorescent cooling of a solid,* Nature **377**, 500 (1995).

[13] M. Sheik-Bahae and R. I. Epstein, *Can laser light cool semiconductors?* Phys. Rev. Lett. **92**, 247403 (2004).

[14] K. Usami, A. Naesby, T. Bagci, B. Melholt Nielsen, J. Liu, S. Stobbe, P. Lodahl, and E. S. Polzik, *Optical cavity cooling of mechanical modes of a semiconductor nanomembrane,* Nature Physics **8**, 168 (2012).

[15] S. Sharma, Y. M. Blanter, and G. E. W. Bauer, *Light scattering by magnons in whispering gallery mode cavities,* Phys. Rev. B **96**, 094412 (2017).

[16] J. A. Haigh, A. Nunnenkamp, A. J. Ramsay, and A. J. Ferguson, *Triple-resonant brillouin light scattering in magneto-optical cavities,* Phys. Rev. Lett. **117**, 133602 (2016).

[17] A. Osada, R. Hisatomi, A. Noguchi, Y. Tabuchi, R. Yamazaki, K. Usami, M. Sadgrove, R. Yalla, M. Nomura, and Y. Nakamura, *Cavity optomagnonics with spin-orbit coupled photons,* Phys. Rev. Lett. **116**, 223601 (2016).

[18] X. Zhang, N. Zhu, C.-L. Zou, and H. X. Tang, *Optomagnonic whispering gallery microresonators,* Phys. Rev. Lett. **117**, 123605 (2016).

[19] C. W. Gardiner and M. J. Collett, *Input and output in damped quantum systems: Quantum stochastic differential equations and the master equation,* Phys. Rev. A **31**, 3761 (1985).

[20] C. Vittoria, S. D. Yoon, and A. Widom, *Relaxation mechanism for ordered magnetic materials,* Phys. Rev. B **81**, 014412 (2010).

[21] E. Schlömann, *Spin-wave analysis of ferromagnetic resonance in polycrystalline ferrites,* Journal of Physics and Chemistry of Solids **6**, 242 (1958).

[22] Á. Rivas and S. F. Huelga, *Open Quantum Systems: An Introduction* (Springer Berlin Heidelberg, 2012).

[23] W. F. Brown, *Thermal fluctuations of a single-domain particle,* Phys. Rev. **130**, 1677 (1963).

[24] L. Landau and E. Lifshitz, *Chapter xii - fluctuations,* in *Statistical Physics*, edited by L. Landau and E. Lifshitz (Butterworth-Heinemann, Oxford, 1980) 3rd ed., pp. 333 – 400.

[25] H. Suhl, *The theory of ferromagnetic resonance at high signal powers,* Journal of Physics and Chemistry of Solids **1**, 209 (1957).

[26] S. M. Rezende and F. M. de Aguiar, *Spin-wave instabilities, auto-oscillations, and chaos in yttrium-iron-garnet,* Proceedings of the IEEE **78**, 893 (1990).

[27] S. V. Kusminskiy, H. X. Tang, and F. Marquardt, *Coupled spin-light dynamics in cavity optomagnonics,* Phys. Rev. A **94**, 033821 (2016).

[28] A. A. Clerk, M. H. Devoret, S. M. Girvin, F. Marquardt, and R. J. Schoelkopf, *Introduction to quantum noise, measurement, and amplification,* Rev. Mod. Phys. **82**, 1155 (2010).

[29] D. Lacklison, G. Scott, H. Ralph, and J. Page, *Garnets with high magnetooptic figures of merit in the visible region,* IEEE Transactions on Magnetics **9**, 457 (1973).

[30] S. Sharma, B. Zare Rameshti, Y. M. Blanter, and G. E. W. Bauer, *Optimal mode matching in cavity optomagnonics,* arXiv e-prints , arXiv:1903.01718 (2019), arXiv:1903.01718 [cond-mat.mes-hall] .

5

Optimal mode matching

(Einstein's) head was in the clouds, but his feet were on the ground. Those of us who are not so tall have to choose.

Richard P. Feynman

This chapter has been uploaded as S. Sharma, B.Z. Rameshti, Y.M. Blanter, and G.E.W. Bauer arXiv:1903.01718 [1]

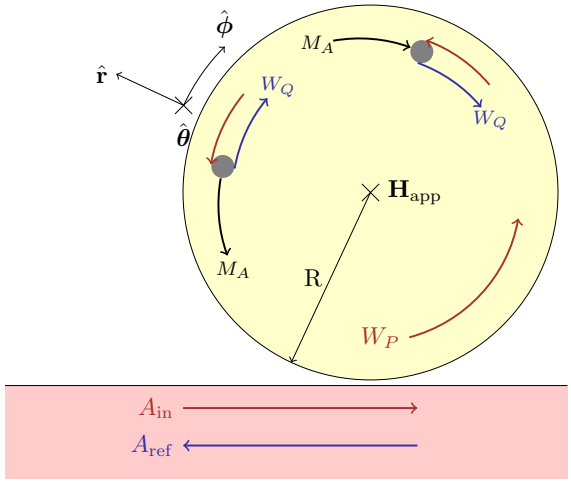

Figure 5.1: A sphere made of a ferromagnetic dielectric in proximity to an optical fiber or prism. A magnetic field saturates the magnetization. The input photons in the fiber, $A_{\rm in}$, leak into the whispering gallery modes (WGMs) $\{W_P\}$. The latter can be reflected by magnons $\{M_A\}$ of twice the angular momentum into the blue, via $W_P + M_A \to W_Q$, or red, $W_P \to W_Q + M_A$, sideband. The photons $\{W_Q\}$ can leak back into the fiber and be observed in the reflection spectrum.

The models, discussed in Chs. 2 and 3, addressed only the magnetostatic magnon modes, i.e. ignored retardation and the exchange interaction. The observed and predicted coupling rates were too low to be able to optically manipulate magnons [2, 3] mainly because of poor overlap between optical and magnonic fields. Higher optomagnonic coupling can be achieved by reducing the size of the magnets down to optical wavelengths [4], but this requires nanostructuring of the magnet [5–7]. In this chapter, we suggest and analyze a method to increase coupling by about 2 orders of magnitude in conventional set-ups with a sub-mm YIG sphere. It can be achieved by coupling to exchange-dipolar modes with wavelengths comparable to those of the WGMs.

Our system, the same as in the previous chapters, is sketched in Fig. 5.1. A ferromagnetic sphere acts as a WGM resonator in which photons interact with the magnetic order via standard proximity coupling to an optical prism or fiber. The frequency of photons is 4 to 5 orders of magnitude larger than magnons at similar wavelengths, thus the incident and scattered photons have nearly the same frequency and wavelength. *Forward scattering* of photons occurs via magnons of large wavelength $\sim 100\,\mu$m, which is a process that is well described by a purely dipolar theory [Sec. 2]. Here we discuss *back scattering* of photons by magnons with sub-μm wavelengths that are affected significantly by exchange. We show that the exchange generates magnetic modes that have a near ideal overlap with the optical WGMs, with an optomagnonic coupling limited only by the bulk magneto-optical constants.

We first briefly review the basics of cavity optomagnonics and derive an upper

bound for the optomagnonic coupling constant in resonators in Sec. 5.1. We model the magnetization dynamics by the Landau-Lifshitz equation introduced in Sec. 5.2. The spatial amplitude of surface exchange-dipolar magnons is discussed in Sec. 5.3, with details of the derivation in App. 5.6. The optomagnonic coupling constants found in Sec. 5.4 are compared with the upper bound found in Sec. 5.1. We conclude with discussion and outlook in Sec. 5.5.

5.1. Ideal magnetization profile

We, first, summarize the basic theory of magnon-photon coupling in spherical optical resonators [8] (discussed also in Sec. 1.4). The electric and magnetic fields of the optical modes in a spherical resonator are labeled by orbital indices $\{l, m, \nu\}$ and a polarization $\sigma \in \{\mathrm{TM}, \mathrm{TE}\}$. They become optical whispering gallery modes (WGMs) at extremal cross sections when $l, m \gg \{1, |l-m|\}$. WGMs are traveling waves in the $\pm\phi$-direction with dimensionless wavelength $2\pi/m$. $\nu - 1$ and $l - m$ are the number of nodes in the optical fields in the r and θ direction. The electric field of these modes is $\mathbf{E}_{\mathrm{TM}} = E(\mathbf{r})\hat{\theta}$ and $\mathbf{E}_{\mathrm{TE}} = E(\mathbf{r})\hat{\mathbf{r}}$ where [9],

$$E(\mathbf{r}) = \mathcal{E} Y_l^m(\theta, \phi) J_l(kr). \tag{5.1}$$

Here J_l is the Bessel function of order l [Eq. (5.64)] and Y_l^m is a scalar spherical harmonic [Eq. (5.57)]. The wave number k, for $l \gg 1$ [9]

$$kR \approx l + \beta_\nu \left(\frac{l}{2}\right)^{1/3} - P_\sigma, \tag{5.2}$$

where R is the radius of the sphere, $\beta_\nu \in \{2.3, 4.1, 5.5, \ldots\}$ are the negative of the zeros of Airy's function $\mathrm{Ai}(x)$, $P_{\mathrm{TM}} = n_s/\sqrt{n_s^2 - 1}$, and $P_{\mathrm{TE}}^{-1} = n_s\sqrt{n_s^2 - 1}$. $\mathcal{E}$ is a normalization constant chosen such that the integral over the system volume

$$\int \left[\frac{\epsilon_s}{2}|\mathbf{E}|^2 + \frac{1}{2\mu_0}|\mathbf{B}|^2\right] dV = \frac{\hbar\omega}{2}, \tag{5.3}$$

where $i\omega\mathbf{B} = \nabla \times \mathbf{E}$, $\epsilon_s = \epsilon_0 n_s^2$, and $\omega = kc/n_s$ with n_s being the refractive index of the sphere. Then

$$\mathcal{E} = \sqrt{\frac{\hbar\omega}{2\epsilon_s R^3 \mathcal{N}_l(kR)}}, \tag{5.4}$$

where

$$\mathcal{N}_l(x) \triangleq \int_0^1 \tilde{r}^2 d\tilde{r} J_l^2(x\tilde{r}) \approx \frac{J_l^2(x) - J_{l+1}(x)J_{l-1}(x)}{2}, \tag{5.5}$$

and the approximation holds again for $l \gg 1$. The angular dependence for $l = m$ with $l \gg 1$, [9]

$$Y_l^l(\theta, \phi) \approx \left(\frac{l}{\pi}\right)^{1/4} \exp\left[-\frac{l}{2}\left(\frac{\pi}{2} - \theta\right)^2\right] \frac{e^{il\phi}}{\sqrt{2\pi}}, \tag{5.6}$$

is a narrow Gaussian around $\theta = \pi/2$ with a width $\sqrt{2/l}$ and a traveling wave along the circle with wave number l/R. The radial dependence for $l \gg 1$ [10]

$$J_l(kr) \approx \left(\frac{2}{l}\right)^{1/3} \mathrm{Ai}\left(x - \beta_\nu\right), \tag{5.7}$$

where the radial coordinate is scaled to

$$x = \frac{l}{(l/2)^{1/3}}\left(1 - \frac{r}{R}\right). \tag{5.8}$$

The leading interaction between magnons and WGMs is 2-photon 1-magnon scattering. Consider a TM polarized WGM $P \equiv \{p, -p', \mu\}$ that scatters into a TE-polarized WGM $Q \equiv \{q, q', \nu\}$ by absorbing a magnon A (to be generalized below). We take in the following $p' > 0$ and thus, back(forward) scattering corresponds to $q' > 0 (q' < 0)$. The coupling constant depends on the modes as [8, 11, 12],

$$G_{PQA} = \frac{n_s \epsilon_0 \lambda_0}{\pi M_s} \int E_P E_Q^* \left(\Theta_C M_{A,\rho} - i\Theta_F M_{A,\phi}\right) dV, \tag{5.9}$$

where the integral is over the sphere's volume, λ_0 is the vacuum wavelength of the incident light, M_s is the saturation magnetization, Θ_F is the Faraday rotation per unit length, Θ_C is the Cotton-Mouton ellipticity per unit length, and $M_{A,\phi}(M_{A,\rho})$ is the $\phi(\rho)$-component of A-magnons.

For the uniform precession of the magnetization, i.e. the Kittel mode K, [13]

$$M_{K,\phi} = iM_{K,\rho} = \sqrt{\frac{\hbar\gamma M_s}{2V_{\mathrm{sph}}}}, \tag{5.10}$$

where V_{sph} is the volume of the sphere, and γ is the modulus of the gyromagnetic ratio. We normalized the magnetization as

$$\int \mathrm{Re}\left[iM_\phi^* M_\rho\right] dV = \frac{\hbar\gamma M_s}{2}, \tag{5.11}$$

equivalent to Eq. (1.69). The coupling constant is finite only when $q' + p' = 1$, $p - |p'| = q - |q'|$, and $\mu = \nu$ [8, 14]. The coupling constant, independent of optical modes,

$$\left|G_{PQK}\right| = G_K = \frac{c\left(\Theta_F + \Theta_C\right)}{n_s\sqrt{2sV_{\mathrm{sph}}}}, \tag{5.12}$$

where $s = M_s/\gamma\hbar$ is the spin density. For the parameters in Table 5.1, $G_K = 2\pi \times 3.6\,\mathrm{Hz}$.

An upper bound on G_{PQA} for a given set of WGMs can be found by maximizing it over all normalized functions $\{M_{A,\rho}(\mathbf{r}), M_{A,\phi}(\mathbf{r})\}$. The solution $\mathbf{M}^{\mathrm{opt}}$ gives the magnetization profile with highest optomagnonic coupling. Later, we show that there exists eigenstates that are close to $\mathbf{M}^{\mathrm{opt}}$. We consider circularly polarized

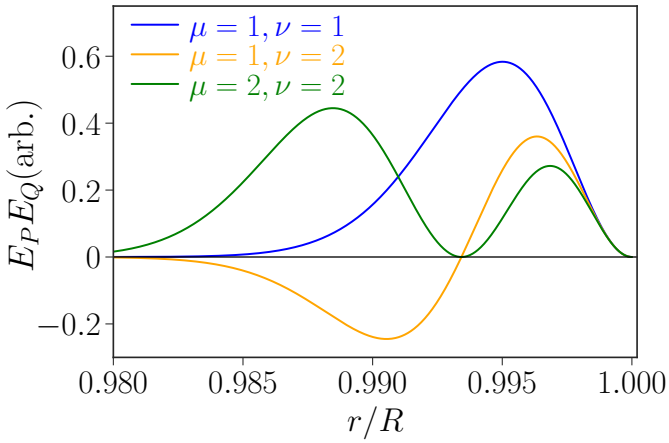

Figure 5.2: The r-dependence of the product of the electric field of WGMs, in arbitrary units, for $p = p' = q = q' = 3000$ and radial mode numbers $\mu, \nu \in \{1, 2\}$. For the parameters of our system in Table 5.1, this corresponds to photons with free space wavelength $\approx 1.3\,\mu$m. The magnons that match these profiles have the largest optomagnonic coupling, cf. Eq. (5.14).

magnons $M_{A,\phi} = iM_{A,\rho}$ and discuss the effect of finite ellipticity below. By the method of Lagrange multipliers,

$$\mathcal{L} = \int E_P E_Q^* M_\phi dV - \lambda \left(\int M_\phi^* M_\phi dV - \frac{\hbar \gamma M_s}{2} \right) \tag{5.13}$$

is stationary at $M_\phi = M_\phi^{\text{opt}}$. We find

$$M_\phi^{\text{opt}} = \frac{E_P^* E_Q}{\lambda} \propto J_p(k_P r) J_q(k_Q r) Y_p^{p'} Y_q^{q'}, \tag{5.14}$$

with

$$\lambda = \sqrt{\frac{2}{\gamma \hbar M_s} \int \left| E_P E_Q \right|^2 dV}. \tag{5.15}$$

Therefore

$$\mathcal{G}_{PQ} \triangleq \left| G_{PQ,\text{opt}} \right| = \frac{c\ (\Theta_F + \Theta_C)}{n_s \sqrt{2 s V_{PQ}}}, \tag{5.16}$$

defining the effective overlap volume

$$V_{PQ} = \frac{\left(\int |E_P|^2 dV \right) \left(\int \left| E_Q \right|^2 dV \right)}{\int |E_P|^2 \left| E_Q \right|^2 dV}. \tag{5.17}$$

The WGMs which are most concentrated to the surface have mode numbers $p = p'$ and $q = q'$. Since the magnon frequency $\sim 10\,$GHz, is much smaller than

λ_{ex}	n_s	M_s	$\gamma/(2\pi)$
109nm	2.2	140 kA/m	28 GHz/T
Θ_F	Θ_C	$H_{\text{app}} - M_s/3$	R
400 rad/m	150 rad/m	$200\,\text{mT}/\mu_0$	$300\,\mu$m

Table 5.1: Parameters for a standard YIG sphere: exchange constant A_{ex} [16, 17], refractive index n_s [16], saturation magnetization M_s [16], gyromagnetic ratio γ [16], Faraday rotation angle Θ_F [18, 19], Cotton-Mouton ellipticity Θ_C [20–22]. We assume the applied dc field H_{app} and the radius R based on typical experimental setup [23–25].

that of the photons, $\sim 100\,\text{THz}$, the incident and scattered photons have nearly the same frequency, implying $p \approx q$ [see Eq. (5.2)]. The Bessel function J_p approaches the Airy function $\text{Ai}(x)$ for $p, q \gg 1$ [see Eq. (5.7)],

$$M_\phi^{\text{opt}} \propto \text{Ai}\left(x - \beta_\mu\right) \text{Ai}\left(x - \beta_\nu\right) e^{-p\left(\frac{\pi}{2}-\theta\right)^2} e^{i(p+q)\phi}, \tag{5.18}$$

where the coordinate x is given by Eq. (5.8) after the substitution $l \to p$. This is a traveling wave in ϕ-direction and a Gaussian in θ-direction. The radial dependence for the lowest $\{\mu, \nu\}$ is plotted in Fig. 5.2, showing strong surface localization. The overlap volume (5.17) now reads

$$V_{PQ} \approx \left(\frac{2}{p}\right)^{7/6} \frac{R^3 \pi^{3/2} \left|\text{Ai}'\left(-\beta_\mu\right) \text{Ai}'\left(-\beta_\nu\right)\right|}{\int_0^\infty \text{Ai}^2\left(x - \beta_\mu\right) \text{Ai}^2\left(x - \beta_\nu\right) dx}, \tag{5.19}$$

For $p = 3000$ and $\mu = \nu = 1$, $V_{\text{sph}}/V_{PQ} \approx 1600$, reflecting the localized nature of the WGMs.

For light with $\lambda_0 = 1.3\,\mu$m, $p = 3190$ for a YIG sphere with parameters in Table 5.1. For the first modes $\{\mu, \nu, \mathcal{G}_{PQ}/(2\pi)\} = \{1, 1, 364\,\text{Hz}\}$, $\{1, 2, 224\,\text{Hz}\}$, and $\{2, 2, 304\,\text{Hz}\}$, so $\mathcal{G}_{PQ} \gg G_K$. For a fixed λ_0, $p \propto R$, and $\mathcal{G}_{PQ} \propto R^{-11/12}$ can be further enhanced by reducing the diameter.

Magnetic anisotropies and dipolar interaction can deform the circular precession of the magnons into an ellipse. Solving the above problem for a hypothetical linearly polarized magnetization precession, e.g. by letting $M_\phi \to \infty$ and $M_\rho \to 0$ while maintaining Eq. (5.11), leads to a diverging $\mathcal{G}_{PQ} \to \infty$. But such strong linear polarization are difficult to achieve in practice and ellipticity is typically limited to $\sim 10\%$, also valid in the calculations below.

A similar analysis for P and Q being TE and TM polarized, respectively, reveals the same results with $\Theta_F + \Theta_C \to \Theta_F - \Theta_C$ and thus reduced couplings by a factor 0.45. It is therefore advantageous to input TM photons over TE for larger blue sideband (magnon absorption) [11, 15]. The coupling constant concerning magnon emission processes follows a very similar discussion since $G_{PQA}^{\text{blue}} = G_{QPA}^*$.

5.2. Landau-Lifshitz equation

Here we derive the equations for the magnetic eigenmodes which will later be shown to approximate the optimal profile derived above. The parameters for a

standard YIG sphere are given in table 5.1. The Gilbert damping does not affect the magnon mode shapes to leading order and is disregarded. The magnetization dynamics then obeys the Landau-Lifshitz equation

$$\frac{d\mathbf{M}}{dt} = -\gamma\mu_0 \mathbf{M} \times \mathbf{H}_{\text{eff}}, \tag{5.20}$$

where $\mathbf{M}$ is the magnetization, μ_0 is the free space permeability, and the effective magnetic field

$$\mathbf{H}_{\text{eff}} = H_{\text{app}}\hat{\mathbf{z}} + \frac{2A_{\text{ex}}}{\mu_0 M_s^2}\nabla^2\mathbf{M} + \mathbf{H}_{\text{dip}}, \tag{5.21}$$

where H_{app} is the applied field that saturates the magnetization to M_s in the $\hat{\mathbf{z}}$-direction, A_{ex} is the exchange constant, and $\mathbf{H}_{\text{dip}}$ is the dipolar field that solves Maxwell's equations in the magnetostatic approximation:

$$\nabla \times \mathbf{H}_{\text{dip}} = 0; \quad \nabla \cdot \mathbf{H}_{\text{dip}} = -\nabla \cdot \mathbf{M}, \tag{5.22}$$

which is valid for magnons with wavelengths sufficiently smaller than $c/\omega \sim 1\,\text{cm}$ [26]. The amplitudes $\mathbf{m} = \mathbf{M} - M_s\hat{\mathbf{z}}$ are taken to be small. The dipolar field has a large dc and a small ac component, $\mathbf{H}_{\text{dip}} = \mathbf{H}_{\text{demag}} + \mathbf{h}_{\text{dip}}$, where the demagnetization field $\mathbf{H}_{\text{demag}} = -M_s\hat{\mathbf{z}}/3$ for a sphere. We disregard the small magnetocrystalline anisotropies in YIG.

The scalar potential $\mathbf{h}_{\text{dip}} = -\nabla\psi$ satisfies

$$\nabla^2\psi = \nabla \cdot \mathbf{m}. \tag{5.23}$$

After substitution into Eq. (5.20), linearizing in $\mathbf{m}$, and in the frequency domain $\partial/\partial t \to -i\omega$,

$$\left[\pm\omega + \omega_a - \frac{\omega_s}{k_{\text{ex}}^2}\nabla^2\right] m_\pm = -\omega_s \partial_\pm \psi, \tag{5.24}$$

where we used the circular coordinates $m_\pm = m_x \pm i m_y$ and $\partial_\pm = \partial_x \pm i\partial_y$. Here $\omega_a = \gamma\mu_0\left(H_{\text{app}} - M_s/3\right)$, $\omega_s = \gamma\mu_0 M_s$, and the inverse exchange length

$$\frac{2\pi}{\lambda_{\text{ex}}} = k_{\text{ex}} = \sqrt{\frac{\mu_0 M_s^2}{2A_{\text{ex}}}}. \tag{5.25}$$

We call $m_-(m_+)$ the Larmor(anti-Larmor) component since $m_+ = 0$ for a pure Larmor precession. Outside the magnet

$$\nabla^2\psi_o = 0. \tag{5.26}$$

The coupled set of differential equations (5.23)-(5.26) are closed by boundary conditions derived from Maxwell's equations,

$$\psi(R) = \psi_o(R); \quad -\partial_r\psi(R) + m_r(R) = -\partial_r\psi_o(R). \tag{5.27}$$

The first condition is required for a finite $\mathbf{h}_{\rm dip}$ at the surface, while the second one enforces continuity of the normal component of the magnetic field $\mathbf{h}_{\rm dip}+\mathbf{m}$.

The boundary conditions for the magnetization depends on the surface morphology and is complicated by the long range nature of the dipolar interaction [27–29]. Here, we present calculations for pinned boundary conditions, $m_{x,y}(R)=0$, valid when the surface anisotropy is high [27, 29, 30] . This is not very realistic for samples with high surface quality but sufficiently accurate for our purposes, as justified in Sec. 5.3.

5.3. Exchange-dipolar magnons

Here we discuss the amplitude of the magnons in dielectric magnetic spheres which resemble the ideal magnetization distribution derived in Sec. 5.1. These are the surface exchange-dipolar magnons localized at the equator derived in App. 5.6. Similar problems have been addressed in Refs. [28, 31] for different geometries.

Analogous to the photons discussed above, magnons in spheres are characterized by three mode numbers $\{l,m,\nu\}$. Their amplitudes are a linear combination of three terms [cf. Eqs. (5.76)-(5.77)],

$$m_{\pm}(\mathbf{r})=m_0 Y_{l\pm1}^{m\pm1}(\theta,\phi)\left[\zeta_{\rm dip,\pm}\left(\frac{r}{R}\right)^{l\pm1}+\zeta_{\rm ex,\pm}\frac{J_{l\pm1}(kr)}{J_{l-1}(kR)}+\zeta_{\rm s,\pm}\frac{I_{l\pm1}(\kappa r)}{I_{l-1}(\kappa R)}\right]. \tag{5.28}$$

with 'dispersion' relations [cf. Eq. (5.61)].

$$\frac{k^2}{k_{\rm ex}^2}=\frac{\omega_{\rm sq}-\omega_{\rm DE}}{\omega_s},\quad \frac{\kappa^2}{k_{\rm ex}^2}=\frac{\omega_{\rm sq}+\omega_{\rm DE}}{\omega_s},\quad \omega_{\rm sq}=\sqrt{\omega^2+\frac{\omega_s^2}{4}},\quad \omega_{\rm DE}=\omega_a+\frac{\omega_s}{2}. \tag{5.29}$$

Here $k_{\rm ex},\omega_s,\omega_a$ are defined below Eq. (5.24), $\omega_{\rm DE}$ is the frequency of the surface magnons in a purely dipolar theory [32, 33], and the normalization constant m_0 is determined below. {'dip','ex','s'} refers to {dipolar, exchange, surface} respectively.

The ratios of anti-Larmor (m_+) and Larmor (m_-) components is measure of the ellipticity [see Eq. (5.78)]:

$$\zeta_{\rm dip+}=0,\quad \frac{\zeta_{\rm ex+}}{\zeta_{\rm ex-}}=\frac{\omega_{\rm sq}-\omega}{\omega_s/2},\quad \frac{\zeta_{\rm s+}}{\zeta_{\rm s,-}}=\frac{\omega_{\rm sq}+\omega}{\omega_s/2}. \tag{5.30}$$

The coefficients ζ read for pinned boundary conditions $\mathbf{m}(R)=0$ [see Eqs. (5.79)-(5.80)],

$$\zeta_{\rm dip,-}=\frac{\omega_{\rm sq}}{\omega_s/2},\quad \zeta_{\rm ex,-}=\frac{-\kappa^2}{k_{\rm ex}^2},\quad \zeta_{\rm s,-}=\frac{-k^2}{k_{\rm ex}^2}. \tag{5.31}$$

Close to the boundary, the 'dip' and 's' terms dominate, but the 'ex' term in $m_\pm$ takes over for $r/R<1-1/l$.

The dipolar (subscript 'dip') term in Eq. (5.28) decays exponentially with distance from the surface with a length scale R/l. This solution is not affected by exchange [13, 33] because $\nabla^2\left(Y_l^m(\theta,\phi)\left(\frac{r}{R}\right)^l\right)=0$. For $l\gg1$ the surface term

(subscript 's') simplifies by the asymptotics of the Bessel function to

$$\frac{I_{l-1}(\kappa r)}{I_{l-1}(\kappa R)} \approx \left(\frac{\sqrt{l^2+\kappa^2R^2}-l}{\sqrt{l^2+\kappa^2R^2}+l}\right)\frac{I_{l+1}(\kappa r)}{I_{l-1}(\kappa R)} \approx \exp\left[-\sqrt{l^2+\kappa^2R^2}\frac{R-r}{R}\right]. \tag{5.32}$$

This is again an exponential decay, but on an even shorter scale $R/\sqrt{l^2+\kappa^2R^2}$ than the dipolar term. At first glance, it appears to have a large negative exchange energy, $\propto -\kappa^2$, but its total contribution to the energy is small due to its very small mode volume. Both 'dip' and 's' terms are important to satisfy the boundary conditions, but they do not contribute significantly to the optomagnonic coupling because the optical WGMs penetrate much deeper into the magnet [see Fig. 5.2]. The exchange 'ex' function in Eq. (5.28), on the other hand, resembles a photon WGM when $kR \approx l$ [see Sec. 5.1]. We show below that this condition is satisfied by magnons with $\nu > 0$.

We now turn to the magnon eigenfrequencies and modes for fixed l and m with $\nu \geq 0$ [using App. 5.6]. For $\nu = 0$, $\omega_0^2 \approx \omega_a^2 + \omega_a\omega_s$ and mode amplitudes Eq. (5.28) approach

$$m_\phi \approx l^{3/2}\sqrt{\frac{\gamma\hbar M_s}{2R^3}}Y_l^m(\theta,\phi)\left(\frac{r}{R}\right)^{l-1}\left(1-\frac{r^2}{R^2}\right) \tag{5.33}$$

and $m_\rho = -im_\phi$ when $k_{\mathrm{ex}}R \gg \sqrt{l}$, which is the case for typical experimental conditions discussed below. We normalized m_ϕ according to Eq. (1.69). Note that (only) the results for $\nu = 0$ depend strongly on the surface pinning.

For non-zero $\nu \sim O(1)$, analogous to Eq. (5.2) for the photons,

$$k_\nu R = l + \beta_\nu\left(\frac{l}{2}\right)^{1/3}, \tag{5.34}$$

where $\beta_\nu \in \{2.3, 4.1, 5.5, \dots\}$ are again the negative of the zeros of Airy's function. We compute coefficients $\{\zeta_{\mathrm{dip},-}, \zeta_{\mathrm{ex},-}, \zeta_{\mathrm{s},-}, \zeta_{\mathrm{dip},+}, \zeta_{\mathrm{ex},+}\} \approx \{3.5, 3.4, 0.1, 0.5, 1.0\}$. Although $\zeta_{\mathrm{ex}} \sim \zeta_{\mathrm{dip}}$, the energy of the 'dip' term is much smaller than that of the 'ex' term because the former is localized to a small skin depth $\sim R/l$ and therefore does not contribute much when integrated over the mode volume. We disregard 'dip' and 's' terms at the cost of an error scales as $\propto l^{-1/3}$ (shown below). The magnetization is

$$m_\phi(\mathbf{r}) \approx \sqrt{\frac{\gamma\hbar M_s}{2R^3\mathcal{N}_l(kR)}}Y_l^m(\theta,\phi)J_l(k_\nu r)\tan\theta_e \tag{5.35}$$

$$m_\rho \approx -im_\phi\cot^2\theta_e, \tag{5.36}$$

for $r/R < 1 - 1/l$. Here $\mathcal{N}$ is given by Eq. (5.5) and the ellipticity is parametrised by

$$\tan\theta_e = \sqrt{\frac{\zeta_{\mathrm{ex},-}-\zeta_{\mathrm{ex},+}}{\zeta_{\mathrm{ex},-}+\zeta_{\mathrm{ex},+}}} = \sqrt{\frac{\omega_s/2-\omega_{\mathrm{sq}}+\omega}{\omega_s/2+\omega_{\mathrm{sq}}-\omega}}. \tag{5.37}$$

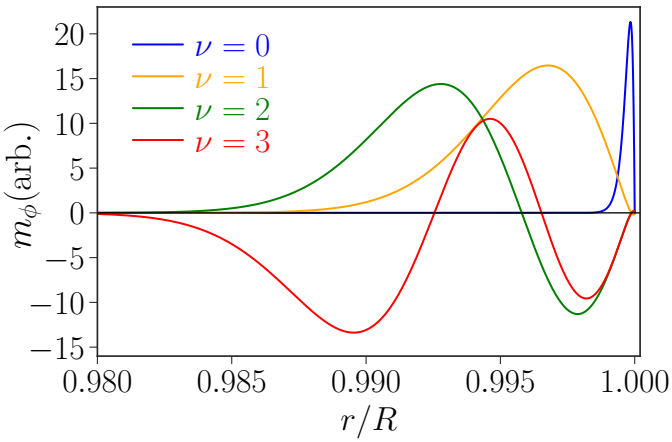

Figure 5.3: Radial dependence of $m_\phi = (m_+ e^{-i\phi} - m_- e^{i\phi})/2$ for $\nu \leq 3$ and $l = 6000$ with parameters from Table I. $\nu = 0$ resembles a purely dipolar wave and is localized to $1 > r/R > 1 - 2/l$. For $\nu > 0$ the magnetization is dominated by the Bessel function except for the region occupied by the $\nu = 0$ mode.

5

The amplitudes (5.35) are normalized according to Eq. (1.69).

For $R = 300\,\mu$m and $l = 6000$ [see Sec. 5.4], $2\pi R/l \approx 300\,$nm is the magnon wavelength for a typical experiment. The azimuthal ϕ-component of the magnetization m_ϕ for $\nu \leq 3$ is plotted in Fig. 5.3, while m_ρ looks similar to m_ϕ after scaling (not shown for brevity). $\nu > 0$ modes contribute significantly to the coupling with large overlap factors [see Sec. 5.4 for explicit expressions].

For the parameters in Table 5.1, we find $\omega_a = 2\pi \times 5.6\,$GHz, and $\omega_s = 2\pi \times 4.9\,$GHz. Putting $kR = l$ in Eq. (5.29), we get the frequency $\omega_N = 2\pi \times 8.4\,$GHz. $\omega_0 = 2\pi \times 7.7\,$GHz, while frequencies for $\nu = \{1, 2, 3\}$ are $\omega_\nu = \omega_N + 2\pi \times \{7.5, 13.2, 17.9\}\,$MHz respectively. We estimate the linewidth of the magnons $\sim \alpha_G \omega_\nu$, in terms of the (geometry-independent) bulk Gilbert constant $\alpha_G = 10^{-4}$. The frequency splittings are an order of magnitude larger than the typical line width, so the magnon resonances are well defined. The exchange mode has a small ellipticity $\tan\theta_e = 0.8$.

At these frequencies the 'surface' term in Eq. (5.28) has wavelengths $2\pi/\kappa_\nu \approx 60\,$nm. It decays much faster into the sphere than the wavelength of infrared light, $> 500\,$nm in YIG, which validates our statements above.

We assumed perfect pinning at the boundary, $m_\pm(R) = 0$, which is realistic only when surface anisotropies are strong [27–29]. While Eqs. (5.28)-(5.30) do not depend on the boundary conditions, the relative weights of three waves, $\{\zeta_{\mathrm{dip},-}, \zeta_{\mathrm{ex},-}, \zeta_{\mathrm{s},-}\}$ do. However, the validity of Eq. (5.35) depends only on the fact that the energy is dominated by the Bessel function which still holds for imperfect pinning and $\nu > 0$. We estimate the contributions of surface exchange waves to

the magnon mode energy by the parameter

$$\eta = \frac{\left|\zeta_{\mathrm{dip},-}\right|^2}{\left|\zeta_{\mathrm{ex},-}\right|^2} \frac{J_l^2(kR)\int (r/R)^{2l} dr}{\int J_l^2(kr) dr}. \tag{5.38}$$

For a film, the squared ratio of the ζ coefficients is ~ 1 [28], which should be the case also for a sphere with curvature R much larger than the magnon wavelength R/l. The second fraction is of $O(l^{-1/3})$. Therefore $\eta \ll 1$, implying that the energy is indeed dominated by the Bessel function as assumed in Eq. (5.35). Reduced pinning changes the magnetization profile near the surface, $r/R > 1 - 1/l$, but not the coupling of states with $\nu > 0$ to the WGMs.

5.4. Optomagnonic coupling

We calculate the coupling constant G_{PQA} given by Eq. (5.9). Consider an incident TM-polarized optical WGM $P \equiv \{p, -p', \mu\}$ that reflects into a TE-polarized WGM $Q \equiv \{q, q', \nu\}$ by absorbing a magnon $A \equiv \{\alpha, \alpha', \xi\}$. Their frequencies are, respectively, ω_P, ω_Q, and $\omega_A \ll \omega_P, \omega_Q$. By energy conservation, $\omega_P \approx \omega_Q$ and thus, $p \approx q$ [see Eq. (5.2)]. For the modes localized near the equator, $\theta = \pi/2$, the indices $x \approx x'$ where $x \in \{p, q, \alpha\}$. The conservation of angular momentum in the z-direction [8], cf. Eq. (5.42), implies $p' + q' = \alpha'$. For $\lambda_0 \approx 1.3\,\mu$m, Eq. (5.2) and Table 5.1 give $p \approx 3000$ for $\nu_P \sim O(1)$. Summarizing, $p \approx p' \approx q \approx q' \approx \alpha/2 \approx \alpha'/2 \approx 3000$.

From Figs. 5.2 and 5.3, we observe that the radial magnon amplitude can be close to the optimal profile. This is also the case in the azimuthal θ-direction close to the equator (not shown). Here, we confirm this observation by explicitly calculating the mode overlap integrals.

The coupling constant Eq. (5.9) can be written

$$G_{PQA} = \frac{c(\Theta_F + \Theta_C)}{n_s\sqrt{2sR^3}} \mathcal{A}_{PQA} \mathcal{R}_{PQA}, \tag{5.39}$$

in terms of the dimensionless angular and radial overlap integrals, $\mathcal{A}_{PQA}$ and $\mathcal{R}_{PQA}$.

The angular part,

$$\mathcal{A}_{PQA} = \int Y_p^{-p'} Y_\alpha^{\alpha'} \left(Y_q^{q'}\right)^* \sin\theta d\theta d\phi. \tag{5.40}$$

is a standard integral that can be written in terms of Clebsch-Gordan coefficients $\langle l_1 m_1, l_2 m_2 | l_3 m_3 \rangle$. For $p, q, \alpha \gg 1$,

$$\mathcal{A}_{PQA} \approx \sqrt{\frac{pq}{2\pi\alpha}} \langle pp', qq' | \alpha\alpha' \rangle \langle p0, q0 | \alpha 0 \rangle. \tag{5.41}$$

With $x = x'$ where $x \in \{p, q, \alpha\}$, the Gaussian approximation [Eq. (5.6)] leads to

$$\mathcal{A}_{PQA} \approx \delta_{\alpha,p+q} \frac{(pq\alpha)^{1/4}}{\pi^{3/4}\sqrt{p+q+\alpha}} \approx \delta_{\alpha,p+q} \frac{p^{1/4}}{3.97}, \tag{5.42}$$

where in the second step, we used $p \approx q \approx \alpha/2$. $\mathcal{A}_{PQA}$ vanishes when $\alpha \neq p+q$, reflecting the conservation of angular momentum in the z-direction. The angular overlap is optimal because $Y_\alpha^\alpha \propto Y_p^p Y_q^q$ for $p \approx q \approx \alpha/2$, which equals the angular part in Eq. (5.18). For $p = 3000$, $\mathcal{A}_{PQA} = 1.9$.

We discuss the radial overlap first for the magnon $\xi = 0$ with magnetization given by Eq. (5.33). Then

$$\mathcal{R}_{PQA}^{(0)} = \int_0^R \frac{\alpha^{3/2} J_p(k_P r) J_q(k_Q r)}{\sqrt{\mathcal{N}_p(k_P R)\mathcal{N}_q(k_Q R)}} \frac{r^{\alpha+1}(R^2 - r^2)}{R^{\alpha+4}} dr \tag{5.43}$$

where $\{k_P, k_Q\}$ are the photon wave numbers, Eq. (5.2). Since the magnetic amplitude is significant only near the surface, we may linearize the optical fields (the Bessel functions) close to R. Using Eq. (5.2) and the Airy's function approximation [10] , cf. Eq. (5.7)

$$J_p(k_P r) \approx \frac{2^{2/3}\mathrm{Ai}'\left(-\beta_\mu\right)}{p^{2/3}} \left[P_{\mathrm{TM}} + p\left(1 - \frac{r}{R}\right)\right], \tag{5.44}$$

and

$$\mathcal{N}_p(k_P R) \approx \left(\frac{2}{p}\right)^{4/3} \frac{\mathrm{Ai}'^2\left(-\beta_\mu\right)}{2}. \tag{5.45}$$

Similar results hold for $\{p, P, \mu, P_{\mathrm{TM}}\} \to \{q, Q, \nu, P_{\mathrm{TE}}\}$. For $p \approx q \approx \alpha/2$,

$$\mathcal{R}_{PQA}^{(0)} = \sqrt{\frac{2}{p}} \left[P_{\mathrm{TM}} P_{\mathrm{TE}} + P_{\mathrm{TM}} + P_{\mathrm{TE}} + \frac{3}{2}\right]. \tag{5.46}$$

For $p = 3000$ and $n_s = 2.2$, $\mathcal{R}_{PQA}^{(0)} = 0.08$ and the coupling $G_{PQA}^{(0)} = 2\pi \times 2.8\,\mathrm{Hz}$ is of the same order as that to the Kittel mode, $G_K = 2\pi \times 9.1\,\mathrm{Hz}$ [see Sec. 5.1] [8]. We emphasize that this result depends strongly on the magnetic boundary condition (taken to be fully pinned here) and only indicates the smallness of the coupling.

The magnetization Eq. (5.35) for $\xi \geq 1$

$$\frac{\mathcal{R}_{PQA}}{M_e} \approx \int_0^R \frac{dr}{R} \frac{J_p(k_P r) J_q(k_Q r) J_\alpha(k_A r)}{\sqrt{\mathcal{N}_p(k_P R)\mathcal{N}_q(k_Q R)\mathcal{N}_\alpha(k_A R)}}, \tag{5.47}$$

to leading order in α, where

$$M_e = \frac{\tan\theta_e \Theta_F + \cot\theta_e \Theta_C}{\Theta_F + \Theta_C}. \tag{5.48}$$

For a YIG sphere with parameters in table 5.1, the ellipticity of the magnons $\tan\theta_e = 0.8$ and $M_e \approx 0.95$.

The Bessel functions asymptotically become Airy's functions, Eq. (5.7),

$$\frac{\left|\mathcal{R}_{PQA}\right|}{M_e} \approx \sqrt{2} p^{1/3} \int_0^\infty \mathrm{A}_\mu(x)\, \mathrm{A}_\nu(x)\, \mathrm{A}_\xi\left(2^{2/3} x\right) dx, \tag{5.49}$$

μ	ν	ξ	$\mathbb{G}_{PQ}/(2\pi)$	M_r
1	1	1	304Hz	0.88
1	2	1	138Hz	0.65
2	2	3	213Hz	0.74
1	3	2	144Hz	0.82
2	3	4	130Hz	0.66
3	3	5	180Hz	0.70

Table 5.2: The calculated optomagnonic coupling for a given $\{\mu,\nu\}$ and ξ chosen to maximize G_{PQA}. M_r is the radial overlap defined in the text, such that $M_r = 1$ for the ideal magnetization distribution. $M_r \sim 1$ indicates high overlap.

where the scaled radial coordinate x

$$x = \frac{l}{(l/2)^{1/3}}\left(1 - \frac{r}{R}\right), \tag{5.50}$$

and the normalized Airy's function,

$$\mathrm{A}_o\,(x) = \frac{\mathrm{Ai}\,(x-\beta_o)}{|\mathrm{Ai}'\,(-\beta_o)|}. \tag{5.51}$$

$\mathcal{R}_{PQA}$ mainly depends on the radial structure of the mode amplitudes with a weak scaling factor of $p^{1/3}$. We summarize results as $\{\mu,\nu,\xi,\mathcal{R}_{PQA}\}$, where ξ is chosen to maximize $\mathcal{R}_{PQA}$ for given $\{\mu,\nu\}$. For $p = 3000$, we find $\{1,1,1,8.02\}$, $\{1,2,1,3.64\}$, and $\{2,2,3,5.63\}$, much larger than the dipolar mode $\mathcal{R}^{(0)}_{PQA} = 0.08$.

For a given pair (P,Q), we define $\mathbb{G}_{PQ}$ as the maximum over all G_{PQA}. With $x = x'$ where $x \in \{p,q,\alpha\}$, the angular momentum of the magnon is fixed by the WGMs, see Eq. (5.42). The radial index can be found by maximizing the integral appearing in Eq. (5.49) by enumerating it for each ξ. The maximum appears at $\xi \sim O(1)$ for $\mu,\nu \sim O(1)$, so we do not need to go beyond $\xi = 10$.

We present the final results in the table 5.2, where $\mathbb{G}_{PQ} \sim 2\pi \times 100\,\mathrm{Hz}$. This can be compared with the maximum coupling possible for WGMs, $\mathcal{G}_{PQ}$ discussed in Sec. 5.1. We find $\mathbb{G}_{PQ}/\mathcal{G}_{PQ} = M_e M_r$ where M_e is given in Eq. (5.48) and the radial 'mismatch'

$$M_r = \frac{2^{1/3}\int_0^\infty \mathrm{A}_\mu\,(x)\,\mathrm{A}_\nu\,(x)\,\mathrm{A}_\xi\left(2^{2/3}x\right)dx}{\sqrt{\int_0^\infty \mathrm{A}^2_\mu\,(x)\,\mathrm{A}^2_\nu\,(x)\,dx}}. \tag{5.52}$$

Table 5.2 indeed shows $M_r \sim O\,(1)$ implying a near ideal mode matching. Furthermore, $\mathbb{G}_{PQ} \gg G_K$, the coupling to the Kittel mode. By doping with bismuth, the coupling can be increased tenfold [34] to $\mathbb{G}_{PQ} \sim 2\pi \times 1\,\mathrm{kHz}$. We see that $\mathbb{G}_{PQ}/\mathcal{G}_{PQ}$ does not depend on R and hence both scale $\mathbb{G}_{PQ}, \mathcal{G}_{PQ} \propto R^{-0.9}$. For a microsphere with $R = 10\,\mu\mathrm{m}$ ($p \approx 100$), $\mathbb{G}_{PQ} \sim 2\pi \times 2\,\mathrm{kHz}$ should be possible in YIG, but fabrication is challenging. A very similar theory as outlined here can be applied to YIG disks when their aspect ratio is close to unity and the demagnetization fields are

approximately uniform. Scaling those down by nanofabrication of thin films may be the most straightforward option to enhance the coupling in otherwise monolithic optical wave guide structures.

The above analysis for scattering via TM → TE scattering can be generalized, similar to the discussion at the end of Sec. 5.1. The coupling constant $G_{\mathrm{TE}\to\mathrm{TM}}$ is smaller by a factor $(\Theta_F - \Theta_C)/(\Theta_F + \Theta_C) = 0.45$. Also, by Hermiticity, $\left|G^{\mathrm{blue}}_{\sigma\to\sigma'}\right| = |G_{\sigma'\to\sigma}|$ if the directions of motion are reversed as well.

A-magnons are efficiently cooled by the process $P + A \to Q$ when the magnon annihilation rate exceeds that of the magnon equilibration. For the internal optical dissipation κ_{int} and the leakage rate of photons into the fiber κ_{ext}, the cooperativity should satisfy [3]

$$C = \frac{4G_{PQA}^2 n_P}{(\kappa_{int} + \kappa_{ext})\,\kappa_A} > 1 \tag{5.53}$$

where n_P is the number of photons in mode P, $\kappa_A \sim 2\pi \times 0.5$MHz is the magnon's linewidth in YIG, and $\kappa_{int} \sim 2\pi \times 0.1 - 0.5$ GHz [23–25]. We assumed $\omega_P + \omega_M = \omega_Q$ for simplicity. In terms of input power P_{in}, [3]

$$n_P = \frac{4\kappa_{ext}}{(\kappa_{int} + \kappa_{ext})^2}\frac{P_{in}}{\hbar\omega_P}. \tag{5.54}$$

The cooperativity C is maximized at $\kappa_{ext} = \kappa_{int}/2$ for a given input power.

For $G_{PQA} \sim 2\pi \times 200$ Hz, $C_{PQA} = 1$ for $n_P \sim 10^9 - 10^{10}$ requiring large powers $P_{in} \sim 50{-}1000$mW for $\omega_P = 2\pi{\times}200$THz. However, required P_{in} can be significantly reduced by scaling or doping as discussed above: a tenfold increase in G causes a hundredfold decrease in required input power. Similar arguments hold for magnon pumping processes $P \to A + Q'$. The steady state number of magnons is governed by a balance of all cooling and pumping processes, whose analysis we defer to a future work.

The strong coupling regime is reached under the condition $G_{PQA}\sqrt{n_P} > (\kappa_{int} + \kappa_{ext})\,,\kappa_A$ which again requires an unrealistically large $n_P > 10^{12}$ for $G_{PQA} \sim 2\pi \times 200$ Hz and powers exceeding kilowatts, because of the large optical linewidths observed in typical YIG spheres [23–25]. The optical lifetime is limited by material absorption [23] and thus, can be improved only at the cost of reduced magneto-optical coupling. 2-3 orders of magnitude improvement in coupling constant is required to bridge this gap.

5.5. Discussion

We modeled the magnetization dynamics in spherical cavities in order to find its optimal coupling to WGM photons. We find that selected exchange-dipolar magnons localized close to the equator (but not the Damon-Eshbach modes) are almost ideally suited to play that role. We predict an up to 40-fold increase in the coupling constant, implying a 1000-fold larger signal in Brillouin light scattering, as compared to that of the (unexcited) Kittel mode. Further improvement requires smaller optical volumes or higher magneto-optical constants.

The option to shrink the cavity and optical volume is limited by the wavelength λ_0/n_s. For $\lambda_0 = 1.3\,\mu$m and $n_s = 2.2$, a cavity with an optical volume of λ_0^3/n_s^3 gives an upper limit $\sim 2\pi \times 50$ kHz for pure YIG. In a Bi:YIG sphere of radius $\sim \lambda_0/n_s$, the optical first Mie resonance may strongly couple with the Kittel mode [4].

The coupling can be enhanced by the ellipticity angle θ_e of the magnetization, which is controlled by crystalline anisotropy, saturation magnetization, and geometry. Linear polarization $\theta_e \to 0$ or $\theta_e \to \pi/2$ would lead to a unphysical diverging coupling, because in practice magnons are close to circularly polarized, $\theta_e \approx \pi/4$. For YIG spheres the weak ellipticity even suppresses the coupling, $M_e < 1$ in Eq. (5.48).

In purely dipolar theory, the surface magnons are chiral, i.e. only modes with $m > 0$ exist, implying a complete suppression of the red sideband that hinders magnon cooling [3]. This is not necessarily the case when the exchange interaction kicks in [35]. An analysis similar to the one above indeed indicates that exchange-dipolar magnons are only partially chiral, since modes with $m < 0$ acquire finite amplitude [1].

We find that light may efficiently pump or cool certain surface (low wavelength) magnons that do not couple easily to microwaves. This could be used to manipulate macroscopically coherent magnons, raising hopes of accessing interesting non-classical dynamics in the foreseeable future.

5.6. Appendix: Exchange-dipolar magnons

Here, we solve Eqs. (5.23)-(5.26) with Maxwell boundary conditions, Eq. (5.27), and pinned surface magnetization $m_\pm(R) = 0$. The magnetization in the linearized LL equation, Eq. (5.24), can be eliminated in favor of the scalar potential ψ, Eq. (5.23) [28],

$$\left[\left(\mathcal{O}^2 - \omega^2\right)\nabla^2 + \omega_s \mathcal{O}\left(\nabla^2 - \frac{\partial^2}{\partial z^2}\right)\right]\psi = 0, \tag{5.55}$$

where $\mathcal{O} = \omega_a - D_{\rm ex}\nabla^2$ with $D_{\rm ex} = \omega_s/k_{\rm ex}^2$. The general solution for a sphere is complicated because the magnetization breaks the rotational symmetry, but it can be simplified for the surface magnons near the equator. The ansatz

$$\psi(\mathbf{r}) = Y_l^m(\theta,\phi)\Psi(r), \tag{5.56}$$

where

$$Y_l^m(\theta,\phi) = (-1)^m \sqrt{\frac{2l+1}{4\pi}\frac{(l-m)!}{(l+m)!}}\, P_l^m(\cos\theta)e^{im\phi} \tag{5.57}$$

are spherical harmonic functions with associated Legendre polynomials

$$P_l^m(x) = \frac{(-1)^m}{2^l l!}\left(1-x^2\right)^{m/2}\frac{d^{l+m}}{dx^{l+m}}\left(x^2-1\right)^l, \tag{5.58}$$

[1] Our calculations not discussed here

leads to $\nabla^2\psi = Y_l^m \hat{O}_l \Psi$ where

$$\hat{O}_l = \frac{1}{r^2}\frac{\partial}{\partial r}\left(r^2\frac{\partial}{\partial r}\right) - \frac{l(l+1)}{r^2} \tag{5.59}$$

have spherical Bessel functions of order l as eigenfunctions. The surface magnons with large angular momentum l are localized near the equator. They have a large "kinetic energy" along the equator. The confinement along the θ-direction is not so strong, however, so the magnon amplitude looks like a flat tire. A posteriori, we find $k_\theta \propto \sqrt{l}$, while $k_\phi \propto l$. For large l, the terms $\partial_z^2 \approx R^{-2}\partial_\theta^2$ near the equator, may therefore be disregarded in Eq. (5.55). This gives a cubic in $\hat{O}_l$, similar to a magnetic cylinder [31],

$$\hat{O}_l\left(\hat{O}_l + k^2\right)\left(\hat{O}_l - \kappa^2\right)\Psi = 0, \tag{5.60}$$

where

$$D_{\mathrm{ex}}k^2 = \omega_{\mathrm{sq}} - \omega_a - \frac{\omega_s}{2}, \quad D_{\mathrm{ex}}\kappa^2 = \omega_{\mathrm{sq}} + \omega_a + \frac{\omega_s}{2}, \tag{5.61}$$

where

$$\omega_{\mathrm{sq}} = \sqrt{\omega^2 + \frac{\omega_s^2}{4}}. \tag{5.62}$$

κ is real and k is real as well when $\omega > \sqrt{\omega_a^2 + \omega_a\omega_s}$, which is the case for $k \approx l/R$, i.e. waves propagating along the equator [see Sec. 5.4].

Consider the eigenvalue equation $\hat{O}_l\Psi_\mu = -\mu^2\Psi_\mu$ with reciprocal "length scales" $\mu \in \{0, k, i\kappa\}$. Its two linearly independent solutions are spherical Bessel functions of first and second kind, which in the limit $l \gg 1$ are proportional to Bessel functions of first $[J_l(\mu r)]$ and second $[Y_l(\mu r)$, not to be confused with the spherical harmonic $Y_l^m]$ kind, respectively. $Y_l(\mu r)$ diverges at $r = 0$, so inside the sphere $\Psi_\mu = J_l(\mu r)$. Thus, Eq. (5.60) has three linearly independent solutions, $\{\Psi_0, \Psi_k, \Psi_{i\kappa}\}$ and the general solution is

$$\Psi = \sum_{i=1}^{3} \alpha_i \frac{J_l(\mu_i r)}{\mu_i J_{l-1}(\mu_i R)}, \tag{5.63}$$

where $\mu_1 \to 0$, $\mu_2 = k$, $\mu_3 = i\kappa$, α_i are integration constants, and the Bessel functions

$$J_l(z) = \sum_{r=0}^{\infty} \frac{(-1)^r}{r!(r+l)!}\left(\frac{z}{2}\right)^{2r+l}. \tag{5.64}$$

The spatial distribution of the three components are discussed in more detail in the main text [see Sec. 5.3].

The derivative introduced in Sec. 5.2

$$\partial_\pm\psi = Y_l^m e^{\pm i\phi}\sum_{i=1}^{3}\frac{\alpha_i}{J_{l-1}(\mu_i R)}\left(J_l'(\mu_i r) \mp \frac{mJ_l(\mu_i r)}{\mu_i \rho}\right), \tag{5.65}$$

where $\partial_\pm = \partial_x \pm i\partial_y$. Close to the equator, $\rho \approx r$ and using $l \gg |l-m|$,

$$\partial_\pm \psi \approx \mp Y_{l\pm1}^{m\pm1} \sum_{i=1}^{3} \frac{J_{l\pm1}(\mu_i r)}{J_{l-1}(\mu_i R)}, \tag{5.66}$$

where we used the recursion relations [10]

$$J_{\alpha\pm1}(x) = \frac{\alpha}{x} J_\alpha(x) \mp J'_\alpha(x) \tag{5.67}$$

and $Y_{l\pm1}^{m\pm1} \approx e^{\pm i\phi} Y_l^m$ that holds for $l \gg 1, |l-m|$. Solving Eq. (5.24) for magnetization,

$$m_\pm(\mathbf{r}) = Y_{l\pm1}^{m\pm1} \sum_{i=1}^{3} \zeta_{i,\pm} \frac{J_{l\pm1}(\mu_i r)}{J_{l-1}(\mu_i R)}, \tag{5.68}$$

with coefficients

$$\zeta_{i,\pm} = \frac{\omega_s \alpha_i}{\omega \pm \tilde{\omega}_i}, \tag{5.69}$$

and $\tilde{\omega}_i = \omega_a + D_{\text{ex}}\mu_i^2$.

Outside the magnet, ψ_o satisfies a Laplace equation Eq. (5.26). Using the continuity of magnetic potential and $\psi_o \to 0$ at $r \to \infty$,

$$\psi_o = Y_l^m(\theta,\phi) \left(\frac{R}{r}\right)^{l+1} \sum_{i=1}^{3} \alpha_i \frac{J_l(\mu_i R)}{\mu_i J_{l-1}(\mu_i R)}. \tag{5.70}$$

The integration constants α_i are governed by the boundary conditions: Maxwell boundary conditions, Eq. (5.27), and pinned magnetization boundary condition for the LL equation $m_\pm = 0$, which we justified a posteriori in Sec. 5.3. Demanding $m_-(r=R) = 0$ and $\partial_r(\psi - \psi_o)\big|_{r=R} = 0$ gives

$$\sum_{i=1}^{3} \frac{\omega_s \alpha_i}{\omega - \tilde{\omega}_i} = 0 = \sum_{i=1}^{3} \alpha_i, \tag{5.71}$$

which is solved by

$$\alpha_1 = m_0 \frac{(\omega - \tilde{\omega}_1)(\tilde{\omega}_2 - \tilde{\omega}_3)}{\omega_s}, \tag{5.72}$$

$$\alpha_2 = m_0 \frac{(\omega - \tilde{\omega}_2)(\tilde{\omega}_3 - \tilde{\omega}_1)}{\omega_s}, \tag{5.73}$$

$$\alpha_3 = m_0 \frac{(\omega - \tilde{\omega}_3)(\tilde{\omega}_1 - \tilde{\omega}_2)}{\omega_s}, \tag{5.74}$$

where m_0 is a normalization constant.

We now arrive at the solution discussed in the main text, Sec. 5.3. With $\{\mu_1, \mu_2, \mu_3\} = \{0, k, i\kappa\}$

$$\lim_{\mu_1 \to 0} J_l(\mu_1 r) \approx \frac{1}{l!}\left(\frac{\mu_1 r}{2}\right)^l ; \quad J_l(i\kappa r) = i^l I_l(\kappa r), \tag{5.75}$$

where I is the modified Bessel function. The above holds also for $l \to l \pm 1$. Substituting into Eq. (5.68),

$$m_- = Y_{l-1}^{m-1}\left[\zeta_{1,-}\left(\frac{r}{R}\right)^{l-1} + \zeta_{2,-}\frac{J_{l-1}(kr)}{J_{l-1}(kR)} + \zeta_{3,-}\frac{I_{l-1}(\kappa r)}{I_{l-1}(\kappa R)}\right] \tag{5.76}$$

$$m_+ = Y_{l+1}^{m+1}\left[0 \qquad + \zeta_{2,+}\frac{J_{l+1}(kr)}{J_{l-1}(kR)} - \zeta_{3,+}\frac{I_{l+1}(\kappa r)}{I_{l-1}(\kappa R)}\right]. \tag{5.77}$$

In spite of $J_{l-1}(\mu_1 r) \to 0$, the first term of m_- is finite while that of m_+ vanishes. The Bessel function ratios in the third terms are real even though $J_l(i\kappa r)$ need not be.

5

According to Eq. (5.69) the polarization does not depend on the coefficients α_i. With $\{\tilde{\omega}_1, \tilde{\omega}_2, \tilde{\omega}_3\} = \{\omega_a, \omega_{\rm sq} - \omega_s/2, -\omega_{\rm sq} - \omega_s/2\}$, $\omega_{\rm sq}^2 = \omega^2 + \omega_s^2/4$

$$\frac{\zeta_{2,+}}{\zeta_{2,-}} = \frac{\omega + \omega_s/2 - \omega_{\rm sq}}{\omega - \omega_s/2 + \omega_{\rm sq}}. \tag{5.78}$$

A similar result holds by substituting $\zeta_{2\pm} \to \zeta_{3\pm}$ and $\omega_{\rm sq} \to -\omega_{\rm sq}$. Multiplying the numerator and denominator in the above equation by $\omega - \omega_s/2 - \omega_{\rm sq}$, we arrive at the form Eq. (5.30) in the main text.

Substituting α_i for the pinned boundary conditions, Eqs. (5.72-5.74), into Eq. (5.69)

$$\zeta_{1,-} = m_0 \frac{2\omega_{\rm sq}}{\omega_s} \tag{5.79}$$

$$\zeta_{2,-} = -m_0 \frac{\omega_a + \omega_{\rm sq} + \omega_s/2}{\omega_s}, \tag{5.80}$$

$$\zeta_{3,-} = m_0 \frac{\omega_a - \omega_{\rm sq} + \omega_s/2}{\omega_s}. \tag{5.81}$$

The above solutions satisfy Maxwell's boundary conditions, Eq. (5.27), and $m_-(R) = 0$ by design [see Eq. (5.71)]. The last condition $m_+(R) = 0$ gives the resonance condition $\mathcal{R}_1(\omega) = \mathcal{R}_2(\omega)$, where

$$\mathcal{R}_1(\omega) = -\frac{J_{l+1}(kR)}{J_{l-1}(kR)}, \quad \mathcal{R}_2(\omega) = \frac{k^2}{\kappa^2}\frac{\omega_{\rm sq} + \omega}{\omega_{\rm sq} - \omega}\frac{I_{l+1}(\kappa R)}{I_{l-1}(\kappa R)}. \tag{5.82}$$

The roots of the above equation are counted by $\nu \geq 0$. For $k > 0$, the lowest root $\nu = 0$ occurs near $k \approx 0$ at frequency $\omega \approx \sqrt{\omega_a^2 + \omega_a \omega_s}$. The next and higher roots occurs only around $kR \gtrsim l$ as plotted in Fig. 5.4 [the root $\nu = 0$ is to the

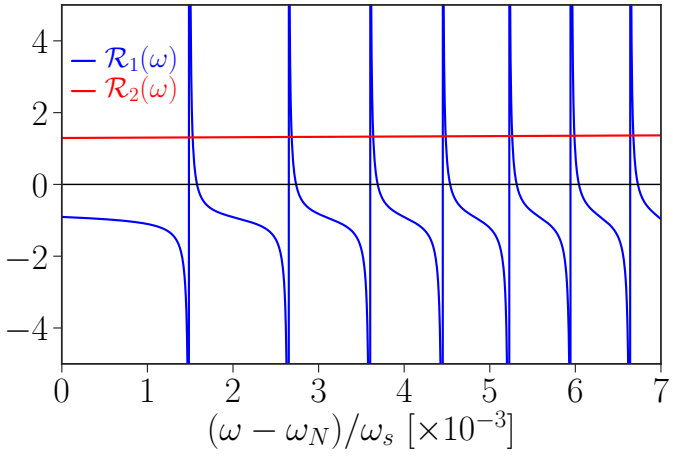

Figure 5.4: The resonance condition $\mathcal{R}_1 = \mathcal{R}_2$ gives the allowed magnon frequencies when the magnetization is pinned at the surface. ω_N is the frequency at which $kR = l$.

far left of the origin]. $\mathcal{R}_1$ is a rapidly varying function, while $\mathcal{R}_2 \approx 1.2$ is nearly constant. Sufficiently far from the zeroes of $J_{l-1}(kR)$, $\mathcal{R}_1 < 0$ and at the crossing with $\mathcal{R}_2$, $\mathcal{R}_1 \approx 1.2$. This implies that at magnon resonances, $J_{l-1}(kR) \approx 0$ or $kR \approx l + \beta_\nu (l/2)^{1/3}$, while $\omega(k)$ is given by Eq. (5.61). Their explicit values are discussed in Sec. 5.3

References

[1] S. Sharma, B. Zare Rameshti, Y. M. Blanter, and G. E. W. Bauer, *Optimal mode matching in cavity optomagnonics,* arXiv e-prints , arXiv:1903.01718 (2019), arXiv:1903.01718 [cond-mat.mes-hall] .

[2] S. V. Kusminskiy, H. X. Tang, and F. Marquardt, *Coupled spin-light dynamics in cavity optomagnonics,* Phys. Rev. A **94**, 033821 (2016).

[3] S. Sharma, Y. M. Blanter, and G. E. W. Bauer, *Optical cooling of magnons,* Phys. Rev. Lett. **121**, 087205 (2018).

[4] E. Almpanis, *Dielectric magnetic microparticles as photomagnonic cavities: Enhancing the modulation of near-infrared light by spin waves,* Phys. Rev. B **97**, 184406 (2018).

[5] V. Berzhansky, T. Mikhailova, A. Shaposhnikov, A. Prokopov, A. Karavainikov, V. Kotov, D. Balabanov, and V. Burkov, *Magneto-optics of nanoscale bi:yig films,* Appl. Opt. **52**, 6599 (2013).

[6] H. Chang, P. Li, W. Zhang, T. Liu, A. Hoffmann, L. Deng, and M. Wu, *Nanometer-thick yttrium iron garnet films with extremely low damping,* IEEE Magnetics Letters **5**, 1 (2014).

[7] C. Hauser, T. Richter, N. Homonnay, C. Eisenschmidt, M. Qaid, H. Deniz, D. Hesse, M. Sawicki, S. G. Ebbinghaus, and G. Schmidt, *Yttrium iron garnet thin films with very low damping obtained by recrystallization of amorphous material,* Scientific Reports **6**, 20827 (2016), article.

[8] S. Sharma, Y. M. Blanter, and G. E. W. Bauer, *Light scattering by magnons in whispering gallery mode cavities,* Phys. Rev. B **96**, 094412 (2017).

[9] A. N. Oraevsky, *Whispering-gallery waves,* Quantum Electronics **32**, 377 (2002).

[10] M. Abramowitz and I. A. Stegun, *Handbook of Mathematical Functions*, Applied Mathematics Series (National Bureau of Standards, 1964).

[11] W. Wettling, M. G. Cottam, and J. R. Sandercock, *The relation between one-magnon light scattering and the complex magneto-optic effects in yig,* Journal of Physics C: Solid State Physics **8**, 211 (1975).

[12] A. Borovik-Romanov and N. Kreines, *Brillouin-mandelstam scattering from thermal and excited magnons,* Physics Reports **81**, 351 (1982).

[13] L. R. Walker, *Magnetostatic modes in ferromagnetic resonance,* Phys. Rev. **105**, 390 (1957).

[14] J. A. Haigh, N. J. Lambert, S. Sharma, Y. M. Blanter, G. E. W. Bauer, and A. J. Ramsay, *Selection rules for cavity-enhanced brillouin light scattering from magnetostatic modes,* Phys. Rev. B **97**, 214423 (2018).

[15] J. Sandercock and W. Wettling, *Light scattering from thermal acoustic magnons in yttrium iron garnet,* Solid State Communications **13**, 1729 (1973).

[16] D. D. Stancil and A. Prabhakar, *Spin Waves: Theory and Applications* (Springer US, 2009).

[17] S. Klingler, A. Chumak, T. Mewes, B. Khodadadi, C. Mewes, C. Dubs, O. Surzhenko, B. Hillebrands, and A. Conca, *Measurements of the exchange stiffness of yig films using broadband ferromagnetic resonance techniques,* Journal of Physics D: Applied Physics **48**, 015001 (2015).

[18] M. N. Deeter, A. H. Rose, and G. W. Day, *Fast, sensitive magnetic-field sensors based on the faraday effect in yig,* Journal of Lightwave Technology **8**, 1838 (1990).

[19] G. Scott and D. Lacklison, *Magnetooptic properties and applications of bismuth substituted iron garnets,* IEEE Transactions on Magnetics **12**, 292 (1976).

[20] J. Castera and G. Hepner, *Isolator in integrated optics using the faraday and cotton-mouton effects,* IEEE Transactions on Magnetics **13**, 1583 (1977).

[21] O. Kamada and S. Higuchi, *Magnetic field sensors using ce:yig single crystals as a faraday element,* IEEE Transactions on Magnetics **37**, 2013 (2001).

[22] J. A. Haigh, S. Langenfeld, N. J. Lambert, J. J. Baumberg, A. J. Ramsay, A. Nunnenkamp, and A. J. Ferguson, *Magneto-optical coupling in whispering-gallery-mode resonators,* Phys. Rev. A **92**, 063845 (2015).

[23] X. Zhang, N. Zhu, C.-L. Zou, and H. X. Tang, *Optomagnonic whispering gallery microresonators,* Phys. Rev. Lett. **117**, 123605 (2016).

[24] A. Osada, R. Hisatomi, A. Noguchi, Y. Tabuchi, R. Yamazaki, K. Usami, M. Sadgrove, R. Yalla, M. Nomura, and Y. Nakamura, *Cavity optomagnonics with spin-orbit coupled photons,* Phys. Rev. Lett. **116**, 223601 (2016).

[25] J. A. Haigh, A. Nunnenkamp, A. J. Ramsay, and A. J. Ferguson, *Triple-resonant brillouin light scattering in magneto-optical cavities,* Phys. Rev. Lett. **117**, 133602 (2016).

[26] M. Hurben and C. Patton, *Theory of magnetostatic waves for in-plane magnetized isotropic films,* Journal of Magnetism and Magnetic Materials **139**, 263 (1995).

[27] R. Soohoo, *Magnetic Thin Films*, Harper's physics series (Harper and Row, 1965).

[28] R. E. D. Wames and T. Wolfram, *Dipole□exchange spin waves in ferromagnetic films,* Journal of Applied Physics **41**, 987 (1970).

[29] K. Y. Guslienko and A. N. Slavin, *Boundary conditions for magnetization in magnetic nanoelements,* Phys. Rev. B **72**, 014463 (2005).

[30] R. E. Camley and D. L. Mills, *Surface response of exchange- and dipolar-coupled ferromagnets: Application to light scattering from magnetic surfaces,* Phys. Rev. B **18**, 4821 (1978).

[31] J. Rychły, V. S. Tkachenko, J. W. Kłos, A. Kuchko, and M. Krawczyk, *Spin wave modes in a cylindrical nanowire in crossover dipolar-exchange regime,* ArXiv e-prints (2018), arXiv:1807.02580 [cond-mat.mes-hall] .

[32] R. Damon and J. Eshbach, *Magnetostatic modes of a ferromagnet slab,* Journal of Physics and Chemistry of Solids **19**, 308 (1961).

[33] J. R. Eshbach and R. W. Damon, *Surface magnetostatic modes and surface spin waves,* Phys. Rev. **118**, 1208 (1960).

[34] D. Lacklison, G. Scott, H. Ralph, and J. Page, *Garnets with high magnetooptic figures of merit in the visible region,* IEEE Transactions on Magnetics **9**, 457 (1973).

[35] M. Kostylev, *Non-reciprocity of dipole-exchange spin waves in thin ferromagnetic films,* Journal of Applied Physics **113**, 053907 (2013), https://doi.org/10.1063/1.4789962 .

Curriculum Vitæ

Sanchar SHARMA

11-09-1992 Born in Jaipur, Rajasthan, India.

Education

2010 High School
Vidya Mandir School, Kota, Rajasthan, India

2010–2015 Dual Degree (Bachelors & Masters) in Electrical Engineering
Indian Institute of Technology, Mumbai, India
Thesis: Self-oscillations in domain wall magnets
Supervisors: Prof. dr. Bhaskaran Muralidharan and Prof. dr. Ashwin Tulapurkar

2015–2019 PhD in Applied Physics
Delft University of Technology, Delft, the Netherlands
Thesis: Cavity Optomagnonics
Promotors: Prof. dr. ir. Gerrit E. W. Bauer and Prof. dr. Yaroslav M. Blanter

List of Publications

6. **S. Sharma**, B. Z. Rameshti, Y. M. Blanter, and G. E. W. Bauer, Optimal mode matching in cavity optomagnonics, arXiv:1903.01718

5. T. Yu, **S. Sharma**, Y. M. Blanter, and G. E. W. Bauer, Surface dynamics of rough magnetic films, Phys. Rev. B 99, 174402 (2019)

4. **S. Sharma**, Y. M. Blanter, and G. E. W. Bauer, Optical cooling of magnons, Phys. Rev. Lett. 121, 087205 (2018)

3. J. A. Haigh, N. J. Lambert, **S. Sharma**, Y. M. Blanter, G. E. W. Bauer, and A. J. Ramsay, Selection rules for cavity-enhanced Brillouin light scattering from magnetostatic modes, Phys. Rev. B. 97, 214423 (2018)

2. **S. Sharma**, Y. M. Blanter, and G. E. W. Bauer, Light scattering by magnons in whispering gallery mode cavities, Phys. Rev. B. 96, 094412 (2017)

1. **S. Sharma**, B. Muralidharan, and A. Tulapurkar, Proposal for a Domain Wall Nano-Oscillator driven by Non-uniform Spin Currents, Sci. Rep. 5, 14647 (2015)